Full 3D Analysis of the GE90 Turbofan Primary Flowpath

Mark G. Turner
GE Aircraft Engines, Cincinnati, Ohio

Since its founding, NASA has been dedicated to the advancement of aeronautics and space science. The NASA Scientific and Technical Information (STI) Program Office plays a key part in helping NASA maintain this important role.

The NASA STI Program Office is operated by Langley Research Center, the Lead Center for NASA's scientific and technical information. The NASA STI Program Office provides access to the NASA STI Database, the largest collection of aeronautical and space science STI in the world. The Program Office is also NASA's institutional mechanism for disseminating the results of its research and development activities. These results are published by NASA in the NASA STI Report Series, which includes the following report types:

- TECHNICAL PUBLICATION. Reports of completed research or a major significant phase of research that present the results of NASA programs and include extensive data or theoretical analysis. Includes compilations of significant scientific and technical data and information deemed to be of continuing reference value. NASA's counterpart of peer-reviewed formal professional papers but has less stringent limitations on manuscript length and extent of graphic presentations.

- TECHNICAL MEMORANDUM. Scientific and technical findings that are preliminary or of specialized interest, e.g., quick release reports, working papers, and bibliographies that contain minimal annotation. Does not contain extensive analysis.

- CONTRACTOR REPORT. Scientific and technical findings by NASA-sponsored contractors and grantees.

- CONFERENCE PUBLICATION. Collected papers from scientific and technical conferences, symposia, seminars, or other meetings sponsored or cosponsored by NASA.

- SPECIAL PUBLICATION. Scientific, technical, or historical information from NASA programs, projects, and missions, often concerned with subjects having substantial public interest.

- TECHNICAL TRANSLATION. English-language translations of foreign scientific and technical material pertinent to NASA's mission.

Specialized services that complement the STI Program Office's diverse offerings include creating custom thesauri, building customized data bases, organizing and publishing research results . . . even providing videos.

For more information about the NASA STI Program Office, see the following:

- Access the NASA STI Program Home Page at *http://www.sti.nasa.gov*

- E-mail your question via the Internet to help@sti.nasa.gov

- Fax your question to the NASA Access Help Desk at (301) 621-0134

- Telephone the NASA Access Help Desk at (301) 621-0390

- Write to:
  NASA Access Help Desk
  NASA Center for AeroSpace Information
  7121 Standard Drive
  Hanover, MD 21076

NASA/CR—2000-209951

Full 3D Analysis of the GE90 Turbofan Primary Flowpath

Mark G. Turner
GE Aircraft Engines, Cincinnati, Ohio

National Aeronautics and
Space Administration

Glenn Research Center

March 2000

Abstract

The multi-stage simulations of the GE90 turbofan primary flowpath components have been performed. The multistage CFD code, APNASA, has been used to analyze the fan, fan OGV and booster, the 10-stage high-pressure compressor and the entire turbine system of the GE90 turbofan engine. The code has two levels of parallel, and for the 18 blade row full turbine simulation has 87.3% parallel efficiency with 121 processors on an SGI ORIGIN. Grid generation is accomplished with the multistage Average Passage Grid Generator, APG. Results for each component are shown which compare favorably with test data.

Organization

This document is a collection of several presentations, modified presentations (to eliminate GE proprietary information) and papers which have been written or presented in support of this task order. They are arranged in the appendices which follow. They are:

- Appendix A: Parallel 3D Multi-Stage Simulation of a Turbofan Engine, presented at the 1998 NASA HPCCP/CAS workshop, August 25-27, 1998 at the NASA Ames Research Center.

- Appendix B: Application of Multi-Stage Viscous Flow CFD Methods for Advanced Gas Turbine Engine Design and Development, also presented at the 1998 NASA HPCCP/CAS workshop, August 25-27, 1998 at the NASA Ames Research Center.

- Appendix C: GE90 Simulation which has been slightly modified from the presentation given at NASA Lewis Research Center on October 16, 1998.

- Appendix D: "Multistage Simulations of the GE90 Turbine" paper which will be presented at the 1999 ASME IGTI conference.

- Appendix E: Excerpts from the 1999 IGTI scholar lecture paper by John J. Adamczyk "Aerodynamic Analysis of Multistage Turbomachinery Flows in Support of Aerodynamic Design."

- Appendix F: Combustor Analysis description for the efforts to model the combustor in APNASA with source terms. This approach was later replaced by a simple boundary condition treatment for representing combustor profiles.

All slide, chart, page or figure numbers will be referred to using the following format: (Slide 1, A), where the slide number is referenced followed by the appendix letter.

Overview

An overview of this task order is shown in Appendix A. On the title slide (Slide 1, A) is a picture of the GE90 compressor. Each blade row is shown with the contour representing a quantity calculated when running the full compressor with APNASA.

(Slide 2, A) shows how a building block approach has been used in this project. First, rig simulations have been run including the low pressure turbine (LPT), high pressure turbine (HPT), high pressure compressor (HPC) and a GE90 booster rig. The PIP (Performance Improvement Program) HPC is a new 3D Aero compressor which has been designed to have greater efficiency than the original production compressor. In addition to the these rigs, a fan simulation has been run consisting of the fan, fan OGV and booster stator 1. Only in a turbofan engine can a fan of this size be tested. The fan, booster and bypass were then put together and run as a component.

Two systems are then put together at the takeoff Mach 0.25 cycle condition which has been chosen for this simulation. These are the full compression system and the full turbine system. These together then comprise all the turbomachinery of the GE90 engine.

(Slide 3, A) shows all 49 blade rows of the GE90 not including the pylon. All these blade rows have been modeled as part of this project.

The foundation of this effort is the CFD code APNASA. On (Slide 4, A) is a description of the features of the latest versions of APNASA which have been developed at GE. Version 5 has radial multi-block capability. Both Version 4 and 5 allow for non-pure H-grids in dealing with the multistage closure, although pure H-grids can still be run. Both versions have two levels of parallel capability as shown schematically in (Slide 5, A). Each blade row of a component can be run in parallel. In addition, each blade can be decomposed into a number of axial sub-domains. Each sub-domain of each blade row can then be run on a different computer processor in parallel.

The parallel efficiency for this code for an isolated blade row is shown in (Slide 6, A) for an SGI Origin 2000 as well as a network of Hewlett Packard (HP) workstations. MPI is used for the message passing. On the SGI Origin 2000, the parallel speedup is actually super-linear with 2 or 4 processors. This is probably due to an improved cache memory utilization. Different approaches have been taken in modifying the algorithms in APNASA to reduce the amount of network traffic. Using a reduced ADI scheme greatly improves the parallel performance on the network of HP workstations. With this approach, parallel convergence is not identical to serial convergence, but the converged solutions are the same. Excellent parallel efficiencies are obtained with this code.

An example of the fidelity of the calculations is shown in (Slide 7, A) which is the pressure ratio difference between the compressor rig simulation and the measured pressure ratio for the GE90 10 stage HPC. For each stage, the simulation is within 3% of the measured pressure ratio.

In addition to the complex simulation capability, an animation capability FEVis has also been developed under this task order. FEVis can be used to simulate the entire full engine solution with all the blade rows at once. The capability is shown in (Slide 8, A). It is a parallel visualization package utilizing the PV3 library from Bob Haimes at MIT. It allows for MPEG output, which is available for the engine simulation.

Grid Generation

The grid generation for this work is APG. A description is shown on (Slide 2, C). Examples of non-pure H-grids for turbines are shown in (Slides 3-4, C). The axisymmetric grids for the full compression system are shown in (Slides 30-32, C). For the compression system simulations, a pure H-grid is used whereas for the turbine simulations, a non-pure H-grid is used.

Compression System

The compression system is described in (Slides 5-32, C). The HPC simulation is described in Appendix E under the subheading **High Speed Ten Stage Compressor** (pages 15-16, E) and (Figs. 14-22, E).

Combustor

Appendix F describes the Combustor Analysis strategy which was initially adopted for this project. Due to time and funding constraints, this approach was stopped in favor of a simple boundary condition specification approach. This current procedure is also more consistent for future coupling with a combustor code.

Turbine System

Appendices B and D are detailed descriptions of the Turbine System simulation. In addition, (Pages 17-18, E) and (Fig. 25, E) also mention this turbine system simulation.

Parallel Efficiency

The parallel capability of the APNASA code has already been briefly described in the overview section above. In addition to this description in (Slides 4-6, A), there are (Charts 12-14, B), (Page 6, D), (Fig. 1, D) and (Figs. 15-16, D) which describe the parallel performance of APNASA in more detail.

In addition to the parallel capability of the solver APNASA, APG and FEVis, both of which are described above, are designed to run in parallel. APG can grid each blade row separately once the axisymmetric grid has been created. And FEVis uses PVM to collect information from client processors for the full engine visualization.

Applications in Design

The excerpts from the 1999 ASME IGTI scholar paper describes how APNASA can be used in design. The HPC which has been analyzed under this project is presented in this scholar paper to demonstrate how this method compares with other design approaches and experimental data. The GE90 HPT, which is also part of this work (in addition to the NASA AST work being done at GE under AOI 5), is also mentioned in this paper.

Conclusions

The components of the GE90 turbofan engine have been analyzed using the multistage CFD code, APNASA. The components analyzed are the fan, fan OGV and booster, the 10-stage high-pressure compressor and the entire turbine system. This is the first time a dual-spool cooled turbine has been analyzed in 3-D using a multi-stage approach. Grid generation has been accomplished with the multistage Average Passage Grid Generator, APG. Results for each component are shown which compare favorably with test data. The successful flow simulation of the fully coupled high pressure and low pressure turbines has prompted GE to adopt the use of APNASA as a tool to improve design confidence on future turbine designs. The code has two levels of parallel, and for the 18 blade row full turbine simulation has 87.3% parallel efficiency with 121 processors on an SGI ORIGIN 2000. The accuracy and good parallel efficiency of the calculation now allow this code to be effectively used in a design environment, so that multistage effects can be accounted for in turbine design, within the short design cycle times required by industry.

Future Work

The full turbine system has been analyzed as well as each component of the entire compression system. The full compression system comprising 31 blade rows has been set up, but still needs to be run to convergence. This will be done under a follow-on NPSS task NAS3-98004 Task Order #9. Also a cycle condition for the new production GE90 with the 3D Aero compressor will be determined, and this turbofan engine simulated.

Appendix A

Parallel 3D Multi-Stage Simulation of a Turbofan Engine

presented at the 1998 NASA HPCCP/CAS workshop, August 25-27, 1998 at
the NASA Ames Research Center

Parallel 3D Multi-Stage Simulation of a Turbofan Engine
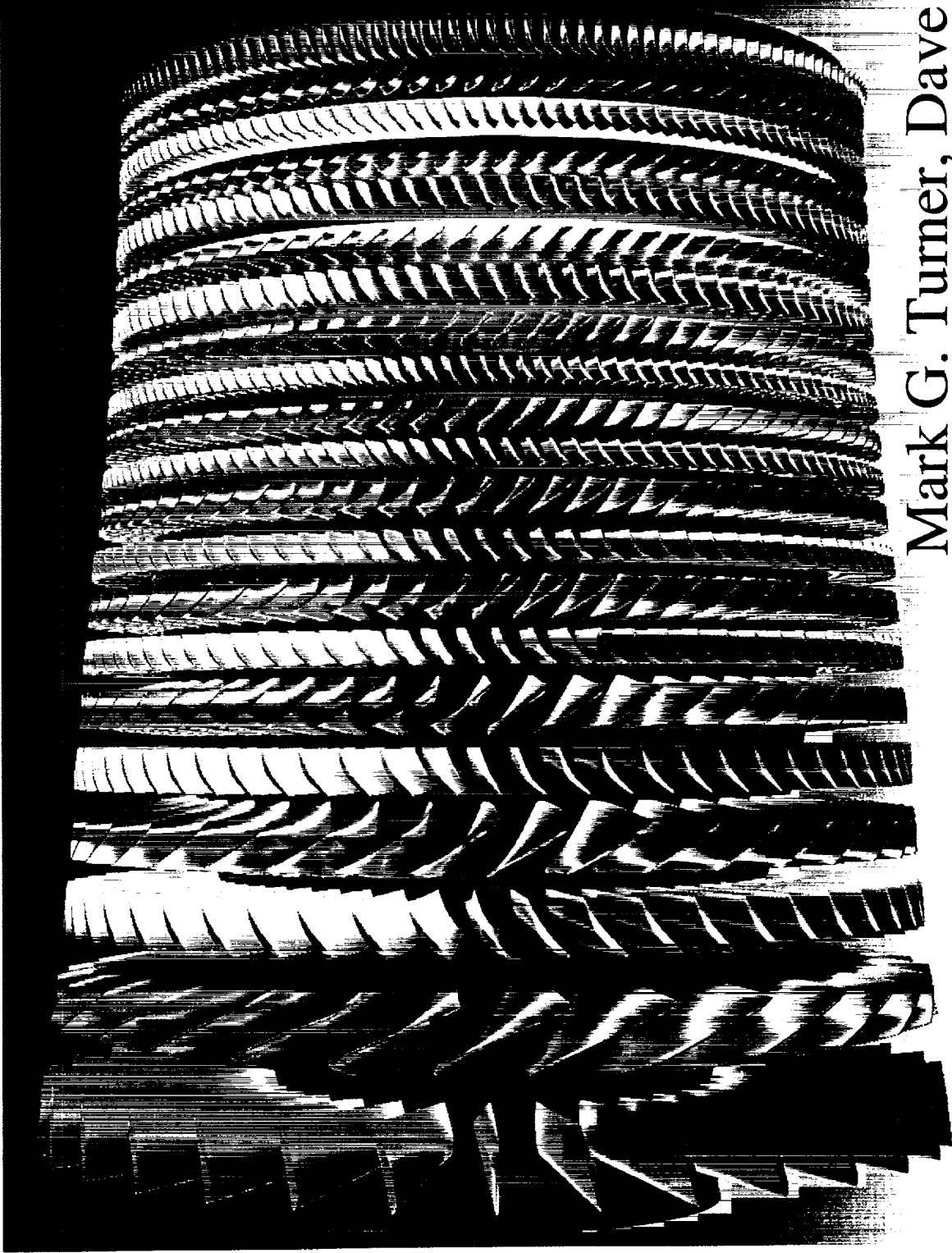
Mark G. Turner, Dave Topp
August 26, 1998

GE Aircraft Engines

Slide 1

6

Building Block Approach

Rigs ⎰ LPT
     ⎱ HPT
       PIP HPC
       booster

→

Components: ⎰ fan + OGV + booster S1
           ⎱ fan + booster + bypass

→

System: ⎰ Compression (31 blade rows)
        ⎱ Turbine (18 blade rows)

→ Full Engine

7

GE90 Turbofan
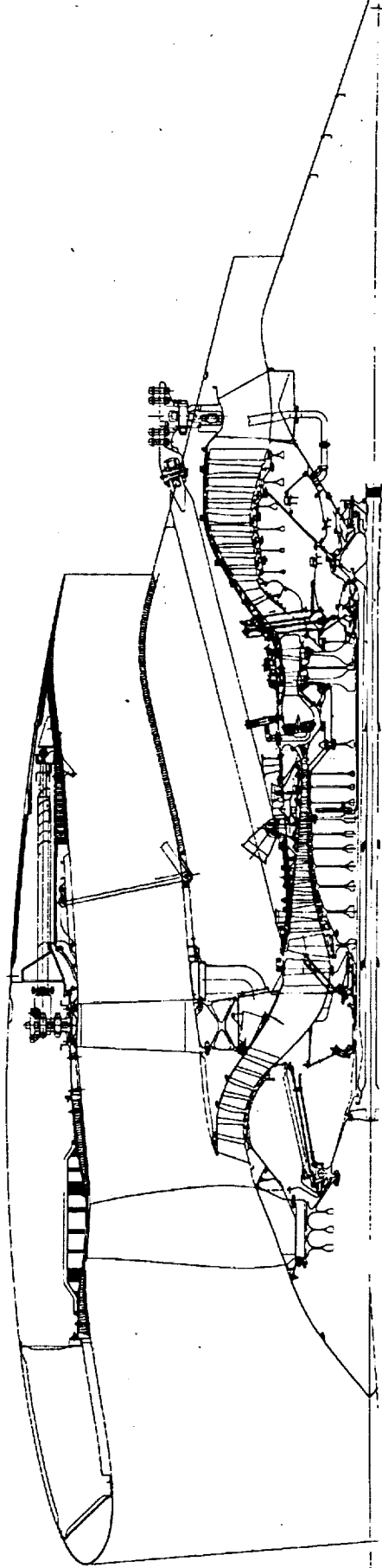
- 49 Blade Rows
  - Fan
  - OGV
  - 3 Stage Booster (7 blade rows)
  - Fan Frame strut
  - 10 Stage High Pressure Compressor (21 blade rows)
  - 2 Stage High Pressure Turbine (4 blade rows)
  - Turbine Mid-Frame Strut
  - 6 Stage Low Pressure Turbine (12 blade rows)
  - Turbine Rear Frame Strut

APNASA Versions 4 & 5

- 4 Stage Runge-Kutta Explicit Navier-Stokes Solver

- Local Time Steps

- Implicit Residual Smoothing

- Implicit k-ε Turbulence Model

- Models Multi-Stage Effects by Calculating Deterministic Stresses

- Domain Decomposition in Axial Direction

- Uses MPI Message Passing

- Uses HDF Files

Two Levels of Parallel
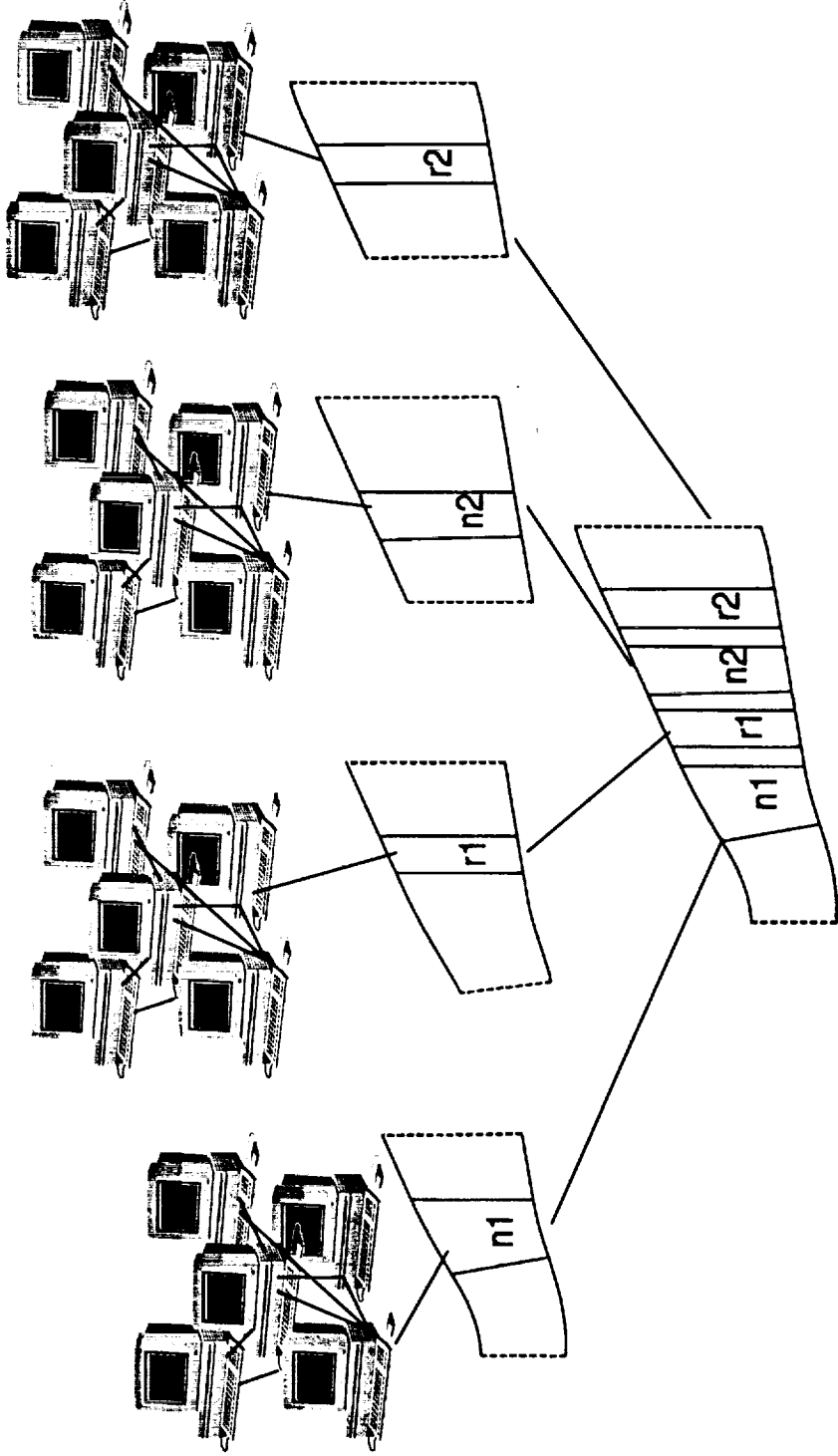
Parallel Efficiency
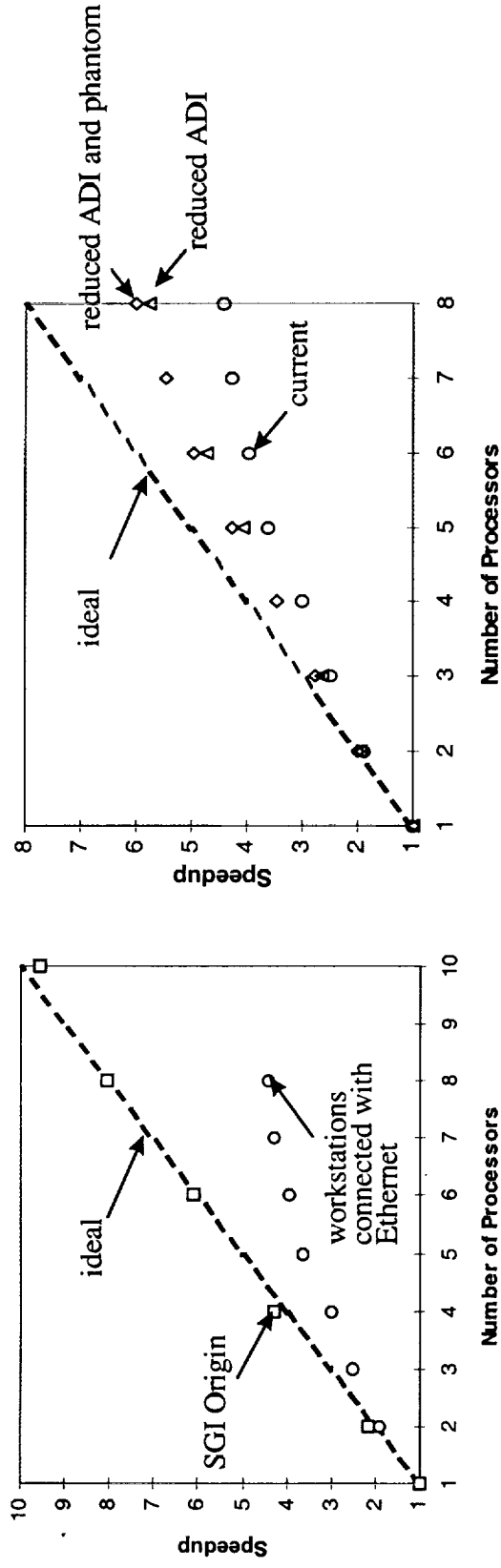
- 227 x 45 x 41 grid (418,815 nodes)
- Domain decomposition in axial (227 nodes) direction only
- Single iteration on SGI with 10 processors is 2.14 seconds on this grid.
- HP workstations connected with 10 Mbit Ethernet. Use CHIMP and LSF.
- Reduced ADI eliminates matrix communication across processor boundaries (parallel convergence does not equal serial convergence).
- Reduced phantom reduces communication at different Runge-Kutta steps (parallel still equals serial).

11

High Pressure Compressor Rig

Pressure Ratio Difference (analysis-measured)/measured
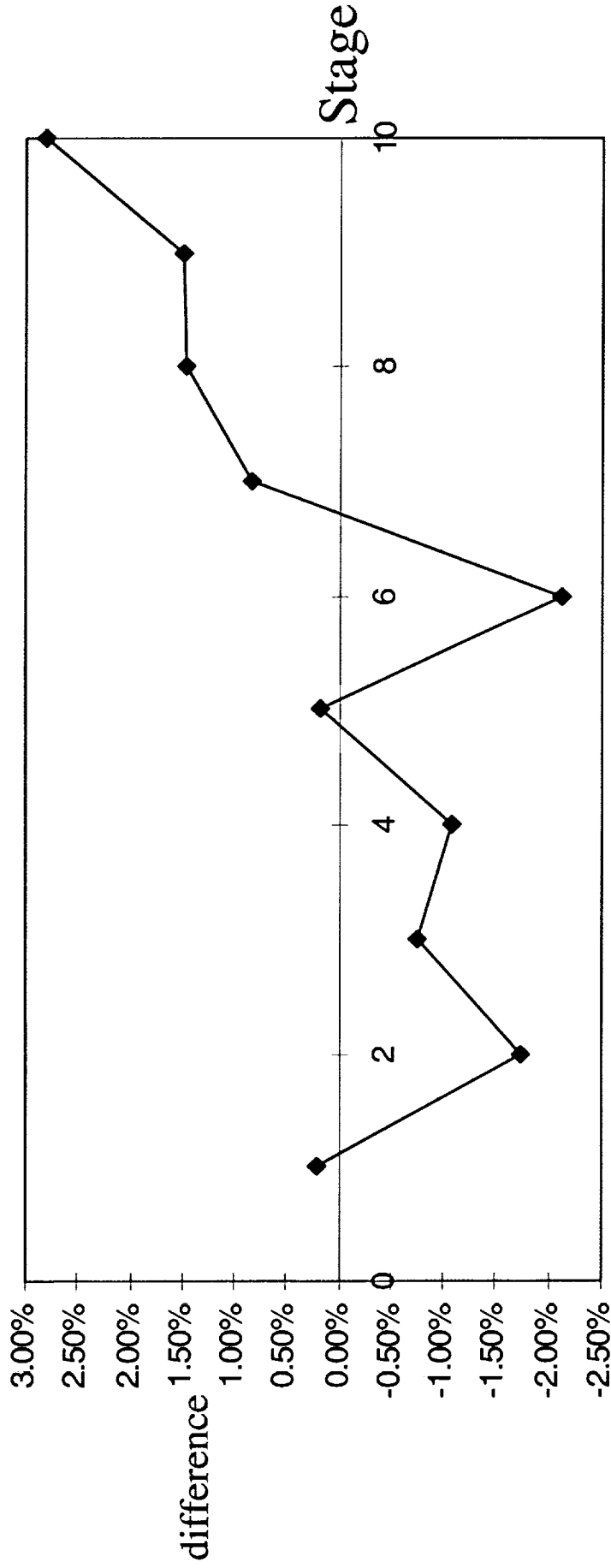
FEVis

- Full Engine Visualization Application
- Uses PV3 library from Bob Haimes
  - PVM for message passing
  - 10 HP C160 workstation clients and an SGI server
- Script based
- Optional MPEG output for animation
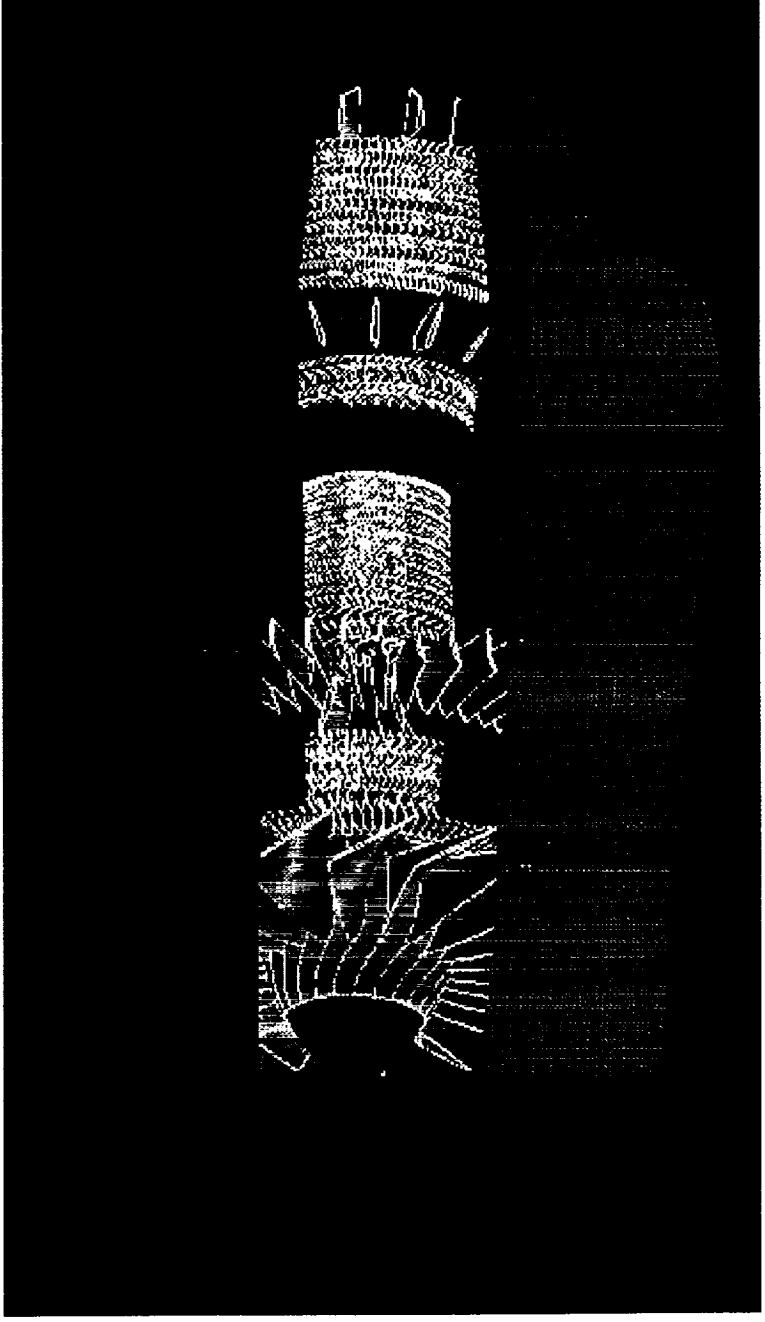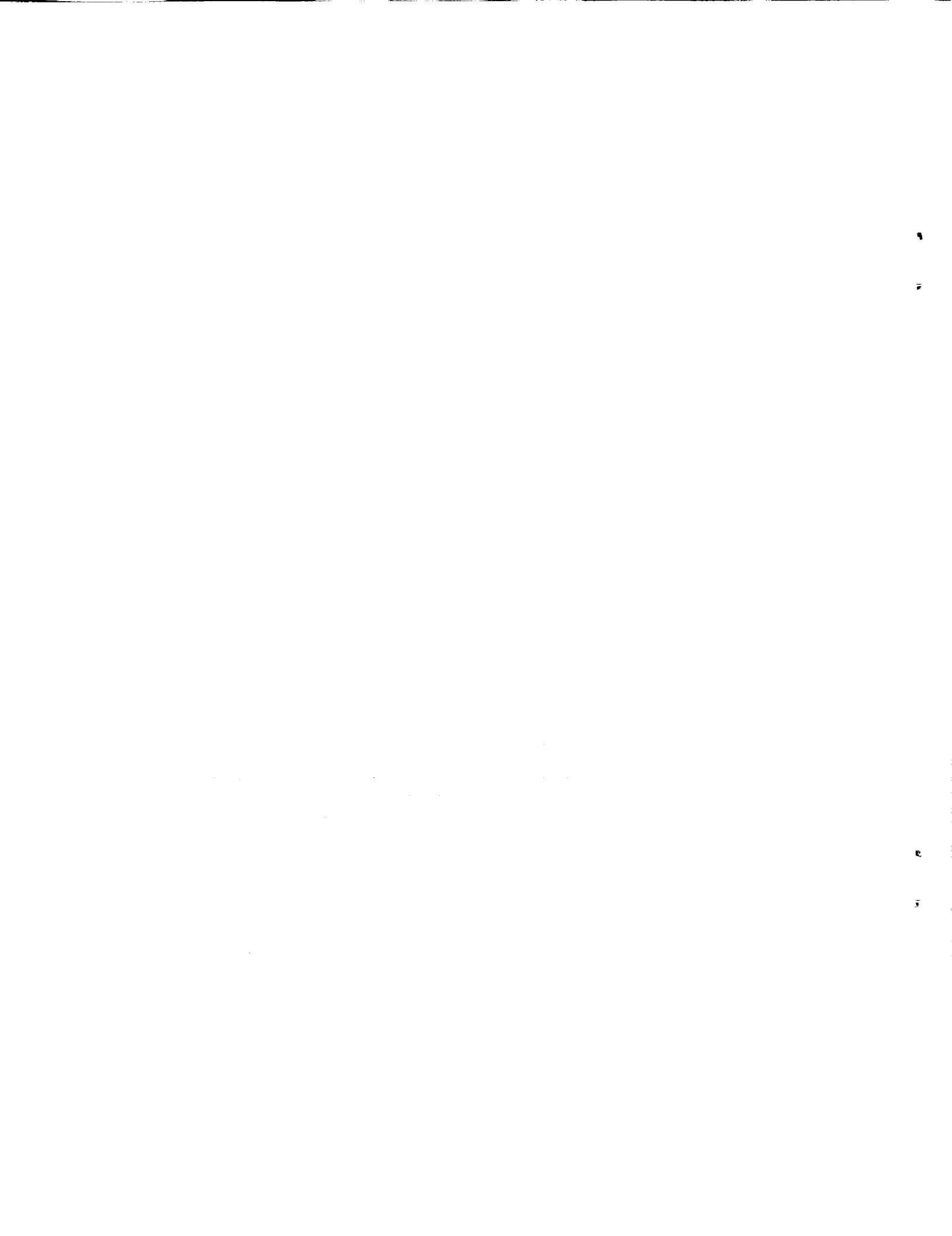
13

Appendix B

Application of Multi-Stage Viscous Flow CFD Methods for Advanced Gas Turbine Engine Design and Development

presented at the 1998 NASA HPCCP/CAS workshop, August 25-27, 1998 at the NASA Ames Research Center

Application of Multi–Stage Viscous Flow CFD Methods for Advanced Gas Turbine Engine Design and Development

Mani Subramanian
Paul Vitt
ASE Technologies, Inc.

David Cherry
Mark Turner
GE Aircraft Engines

Presented at the NASA HPCCP/CAS Workshop

August 25–27, 1998

NASA Ames Research Center

16

ASE Technologies, Inc.

Overview

- Gas turbine engines under development have aggressive performance goals.

  ○ Higher thrust and blade loading, smaller size and weight, lower emissions, and improved efficiency and economy.

- Important element of several national programs:

  ○ NASA –– Advanced Subsonic Technology (AST).
  ○ NASA –– High Speed Civil Transport (HSCT).
  ○ DoD –– Integrated High Performance Turbine Engine Technology (IHPTET).

  ○ DoE –– Advanced Turbine Systems (ATS).

- Require increased physical modeling in accurate, dependable and efficient analysis and design methods.

  ○ To support rapid engine development efforts.

Chart 2 of 15

17

ASE Technologies, Inc.

Objectives

- Simulate inter–component interaction effects with a high level of confidence to guide design and re–design.

- Demonstrate the analytical capability to model large, interacting component assemblies with very good accuracy and in acceptable computational time.

- Extend the methodology to improve

  ○ modeling and physical aspects.

  ○ parallel analysis/code performance enhancement.

Chart 3 of 15

18

ASE Technologies, Inc.

Multi–Tiered Approach

Multi–Method Approach:

● 3D viscous flow analysis in steady state for single blade rows.

● 3D steady state viscous flow analysis for multiple blade rows with the average passage methodology.

● 3D unsteady viscous flow analysis for single and multiple blade rows.

Component Assembly

● Model individual blade rows and turbine stages (high and low pressure).

   ○ Compare with test data to evaluate modeling accuracy.

   ○ Perform necessary model improvements.

● Combine stages by adding individual component models to form the entire turbine, and eventually, the entire engine.

Chart 4 of 15

19

ASE Technologies, Inc.

Progress

3D steady viscous flow analysis of turbomachinery.

Using the HPCCP/CAS resources, several high and low pressure turbine geometries have been analyzed:

● Single stage and multiple stage high pressure turbines: Boeing 737–class, HSCT, IHPTET candidate systems.

 ○ Rig and on–wing flight conditions.

 ○ Take–off and cruise operating points.

● Multiple stage low pressure turbines (Boeing 737 and 777 class engines).

● Combined HP and LP turbines (Boeing 737 and 777 class).

3D unsteady viscous flow analysis of turbomachinery.

● NASA Lewis MSU–Turbo code for IHPTET candidate designs.

● NASA Ames Rotor4 code for Boeing 737 class engines.

Chart 5 of 15

20

ASE Technologies, Inc.

GE90 Full Turbine Simulation Results

● Model separate high pressure and low pressure turbine stages.

○ Experimental test rig conditions.

○ Used to validate the method against experimental data.

● Model the entire turbine of the GE90 (Boeing *777* class) engine.

○ Combined the high pressure turbine, mid–frame strut, low pressure turbine and outer guide vane (18 blade rows total).

○ Take–off operating conditions.

○ Both HP and LP turbines were cooled.

○ Include the effects of seal leakage.

ASE Technologies, Inc.

Data Comparison

● Cooled high pressure turbine rig simulation (4 blade rows).

   ○ Experimental efficiency predicted within 0.5 percent.

   ○ Total pressure ratio was within 0.4% of the data.

   ○ Total temperature ratio was within 1.6% of the data.

● Low pressure turbine rig simulation (14 blade rows).

   ○ Experimental efficiency predicted within 1.0 percent.

   ○ Total pressure ratio was within 0.3% of the data.

   ○ Total temperature ratio was within 3.5% of the data.

Chart 7 of 15

PHV 8/26/98

22

Current Computational Model

- Average passage turbomachinery Navier–Stokes solver, developed at NASA–Lewis.

  ○ Influence of surrounding blade rows is calculated through deterministic stresses (body forces).

  ○ Information is transferred between blade rows periodically, not continually.

- Cooling air was included through source terms which add the equivalent amounts of mass, momentum and energy.

- Leakage through seals and around the blade and vane labyrinth seals was modeled.

  ○ Included through the use of both source terms and mass addition/extraction wall boundary conditions.

ASE Technologies, Inc.

Full Turbine Geometry

Chart 9 of 15

Turbine Relative Mach Numbers
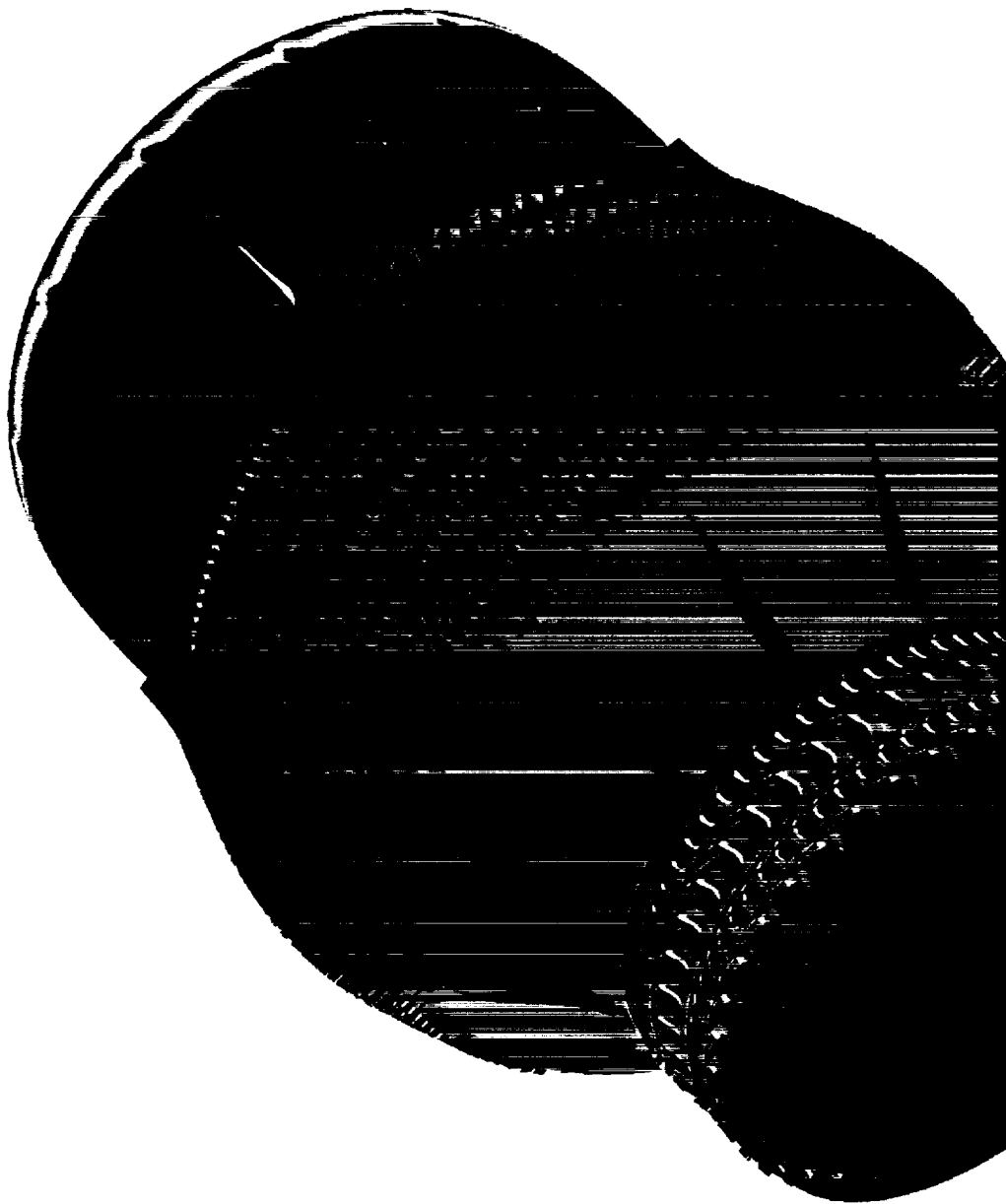
LP Turbine Cooling Flow Aerodynamics

Total
Temperature
Contours

Cooling Flow Streamlines

LP Turbine Blade

Cooling
Flow

26
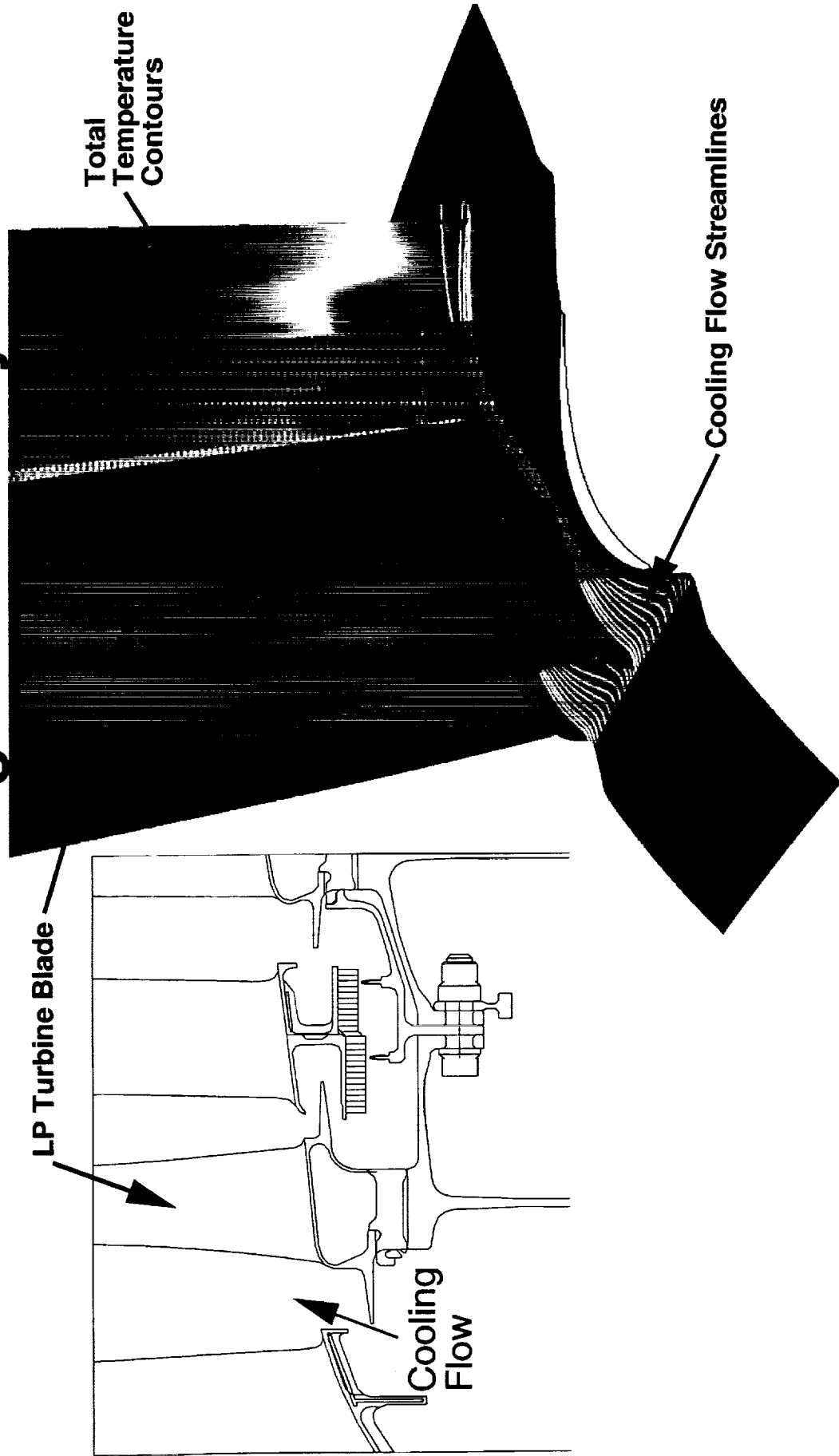
Parallel Performance

● Two levels of parallelization:

○ Blade rows are run individually, only exchanging interaction information periodically.

○ Each blade row is axially decomposed into smaller domains.

● Load Balancing:

○ adjust the number of processors for each blade row to maximize efficiency (minimize wait times).

Domain Sizes and Load Balancing

ASE Technologies, Inc.
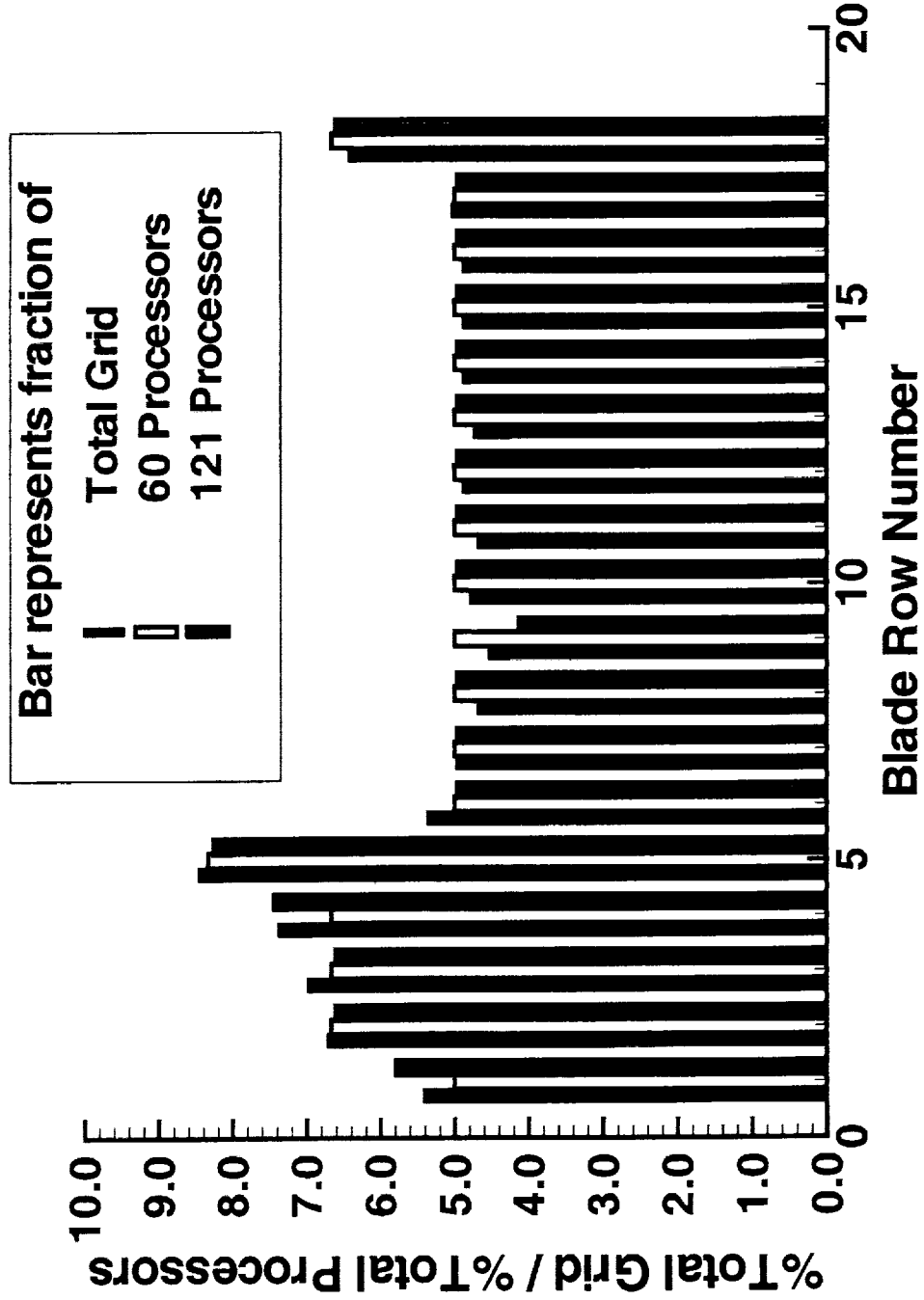
Parallel Efficiency Results

Legend:
- Linear Scalability
- Single Blade Row, Original Robust Method
- Single Blade Row, Increased Efficiency Method
- Full Turbine, 60 proc, Load Balanced
- Full Turbine, 121proc, Load Balanced
- Full Turbine, 54proc, Not Balanced

GE90 HPT+LPT (18BR), Cooled Average Passage Results
Blade Row 1 490000 Grid points, 9e6 Total Grid Points
250 MHz Origin 2000 (Hopper/Steger) August 1998 Data

X-axis: Number of Processors/Blade Row 1
Y-axis: Parallel Speedup Factor

ASE Technologies, Inc.

Summary

● Demonstrated the applicability of the average passage code to predict multi–blade–row interaction effects while achieving good agreement with experimental data.

● Obtained excellent parallel efficiencies.

● Shown the feasibility of large–scale 3D viscous turbomachinery analysis to support design and development efforts.

Chart 15 of 15

30

Appendix C

GE90 Simulation

slightly modified from the presentation given at NASA Lewis Research
Center on October 16, 1998

GE90 Simulation

GE Aircraft Engines

Slide 1
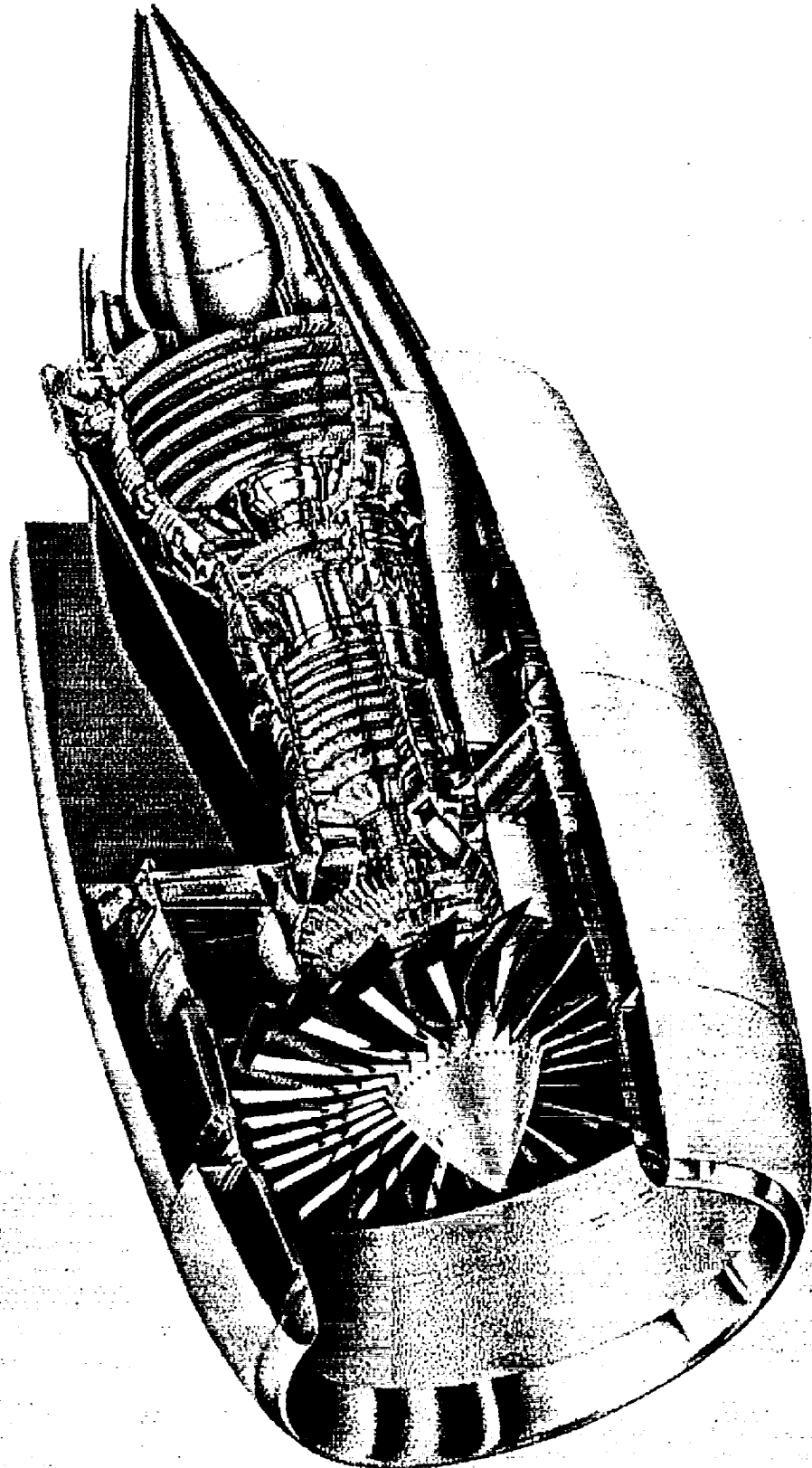
APG Grid Generator

- Script Based
- Uses point or NURB data to define geometry
- Interview mode for Single Passages
- Axi step
- Trim & Grid steps for each blade row in Parallel
- Finish Step

33

APG Grid Generator

GE90 HPT Rotor 1
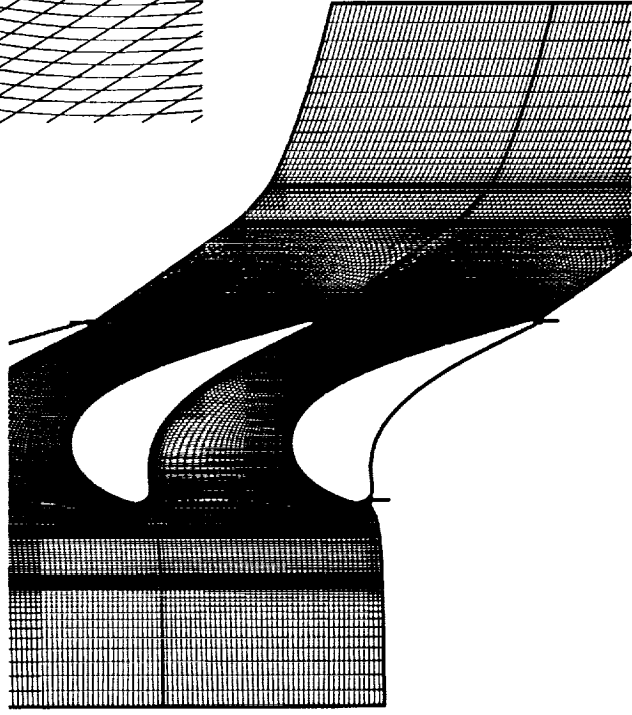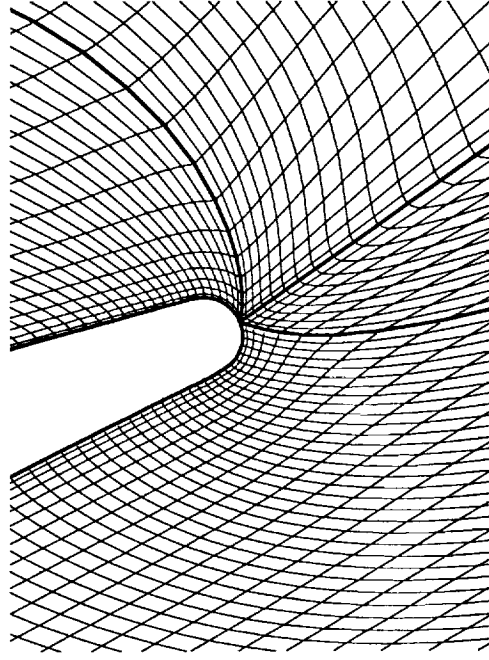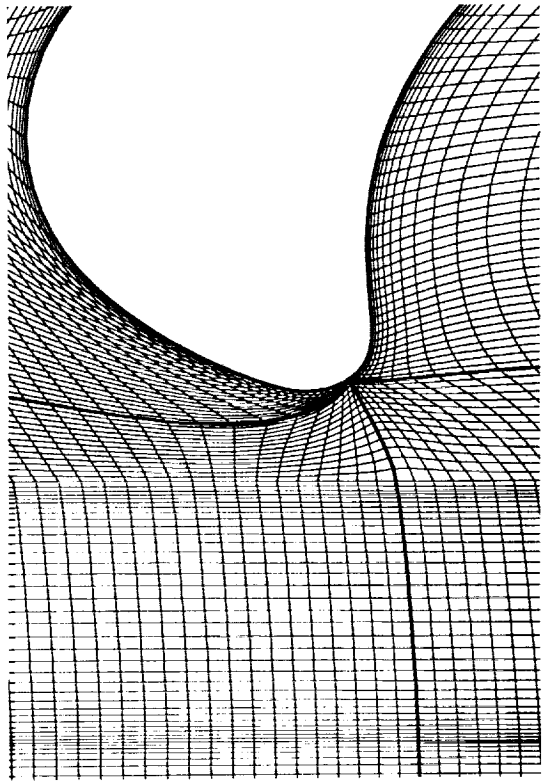
APG Grid Generator

GE90 LPT Rotor 2

High Pressure Compressor Rig

GE Aircraft Engines

Slide 5
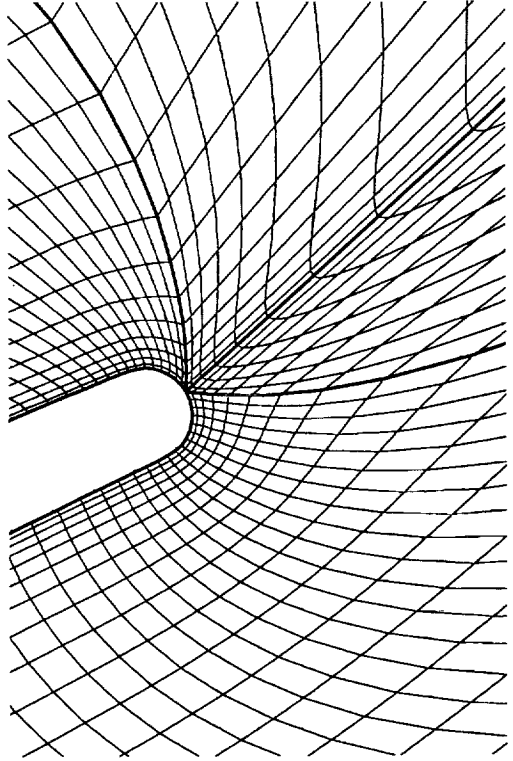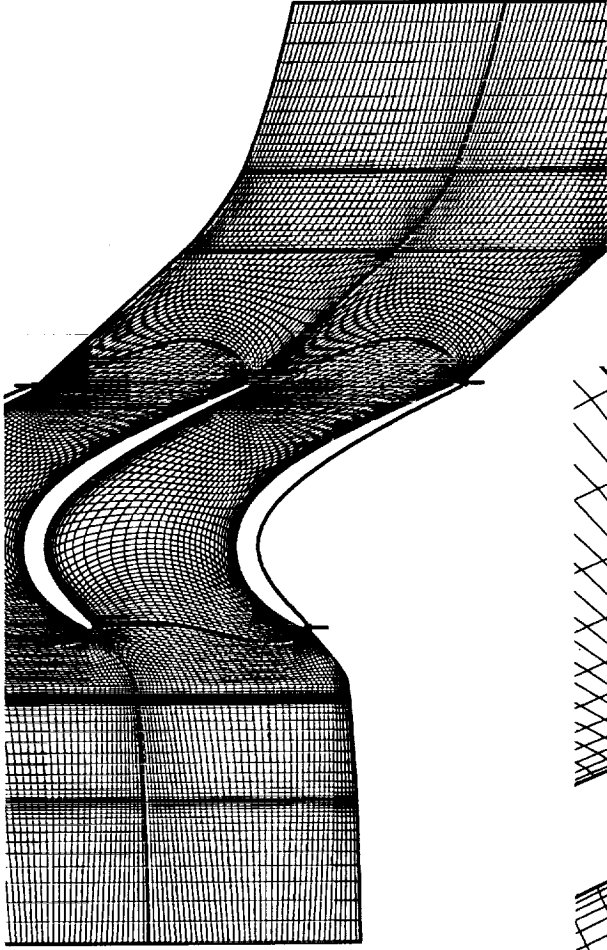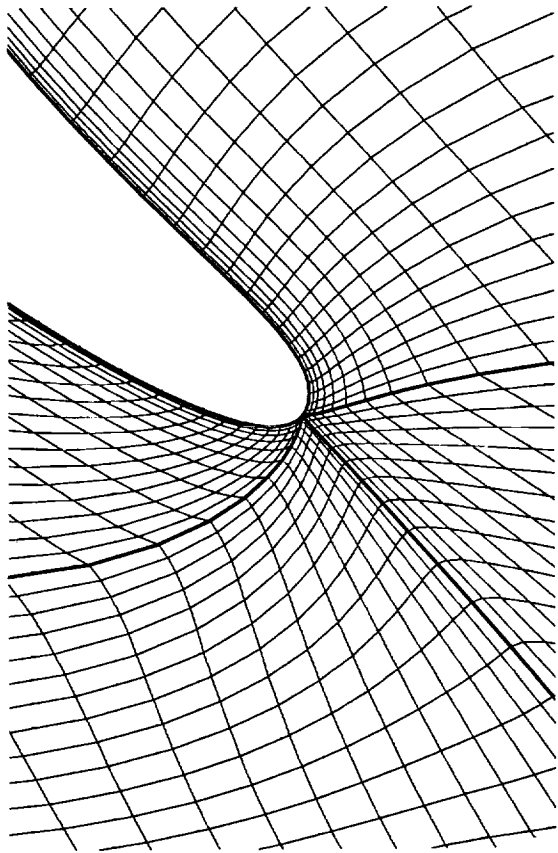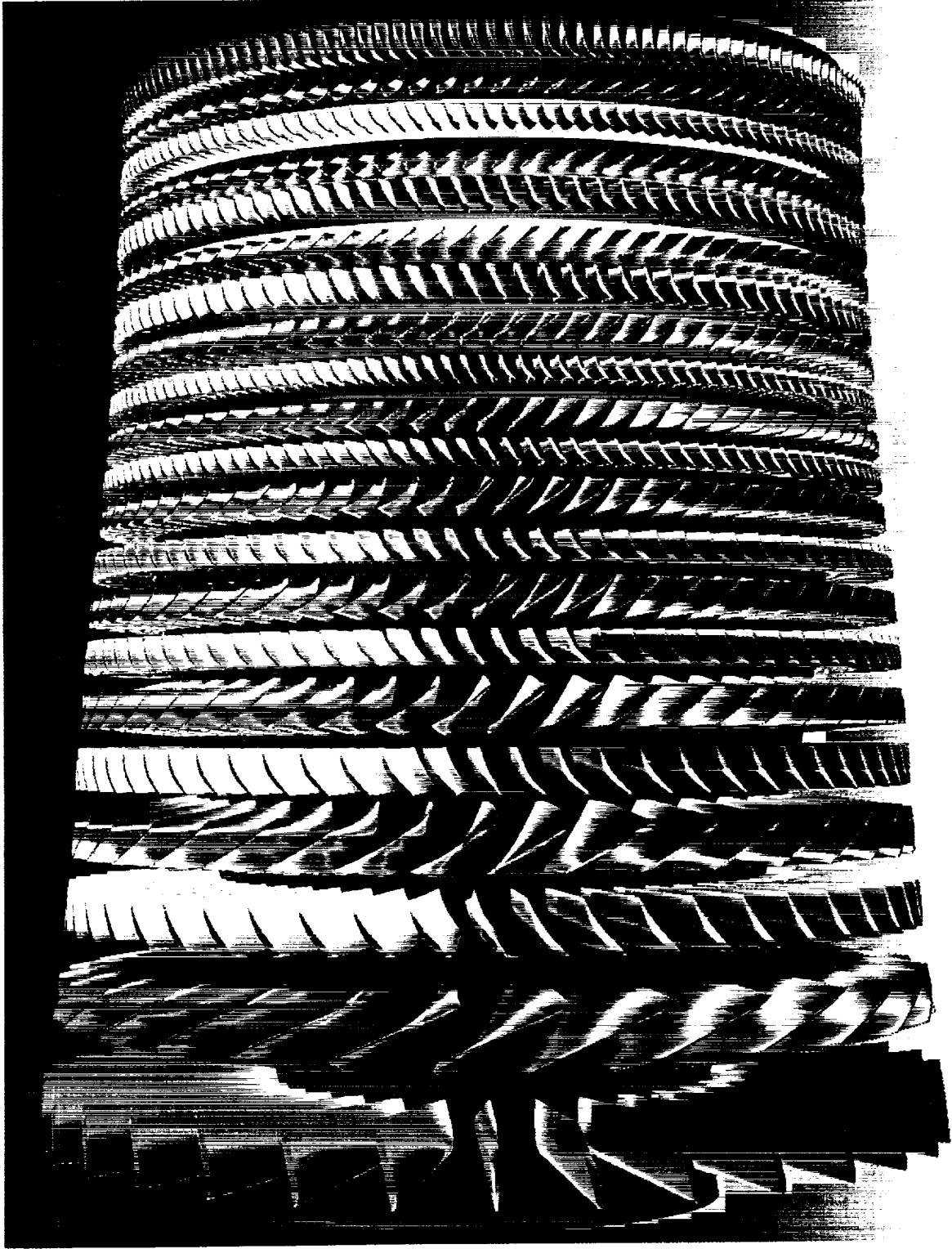
High Pressure Compressor Rig

GE90 PIP Total Pressure, Rdg 53
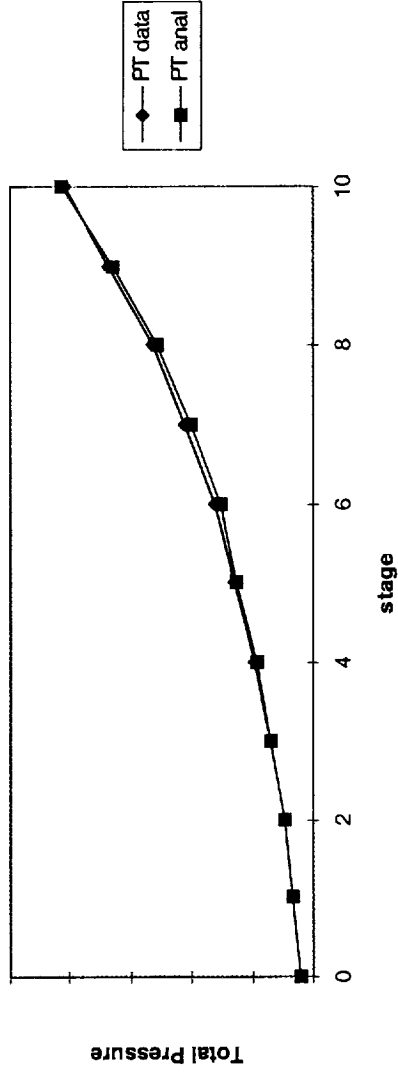
GE90 PIP Total Temperature, Rdg 53
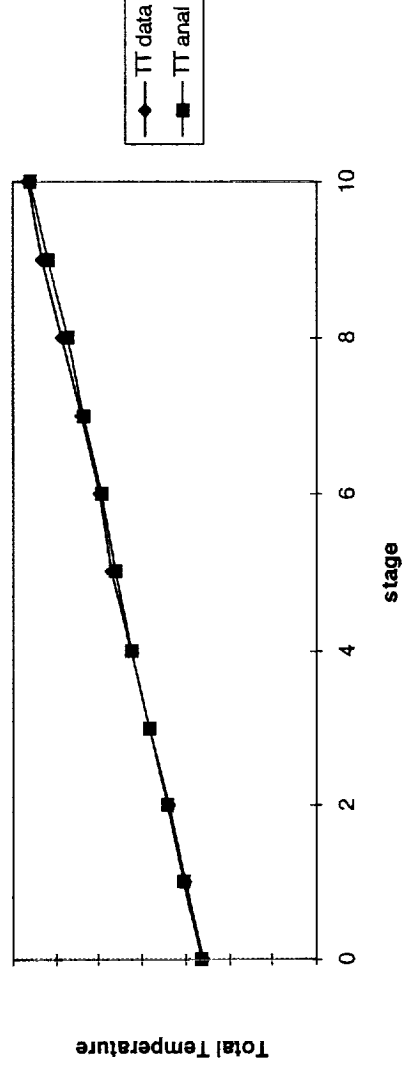
High Pressure Compressor Rig

Error in Pressure Ratio
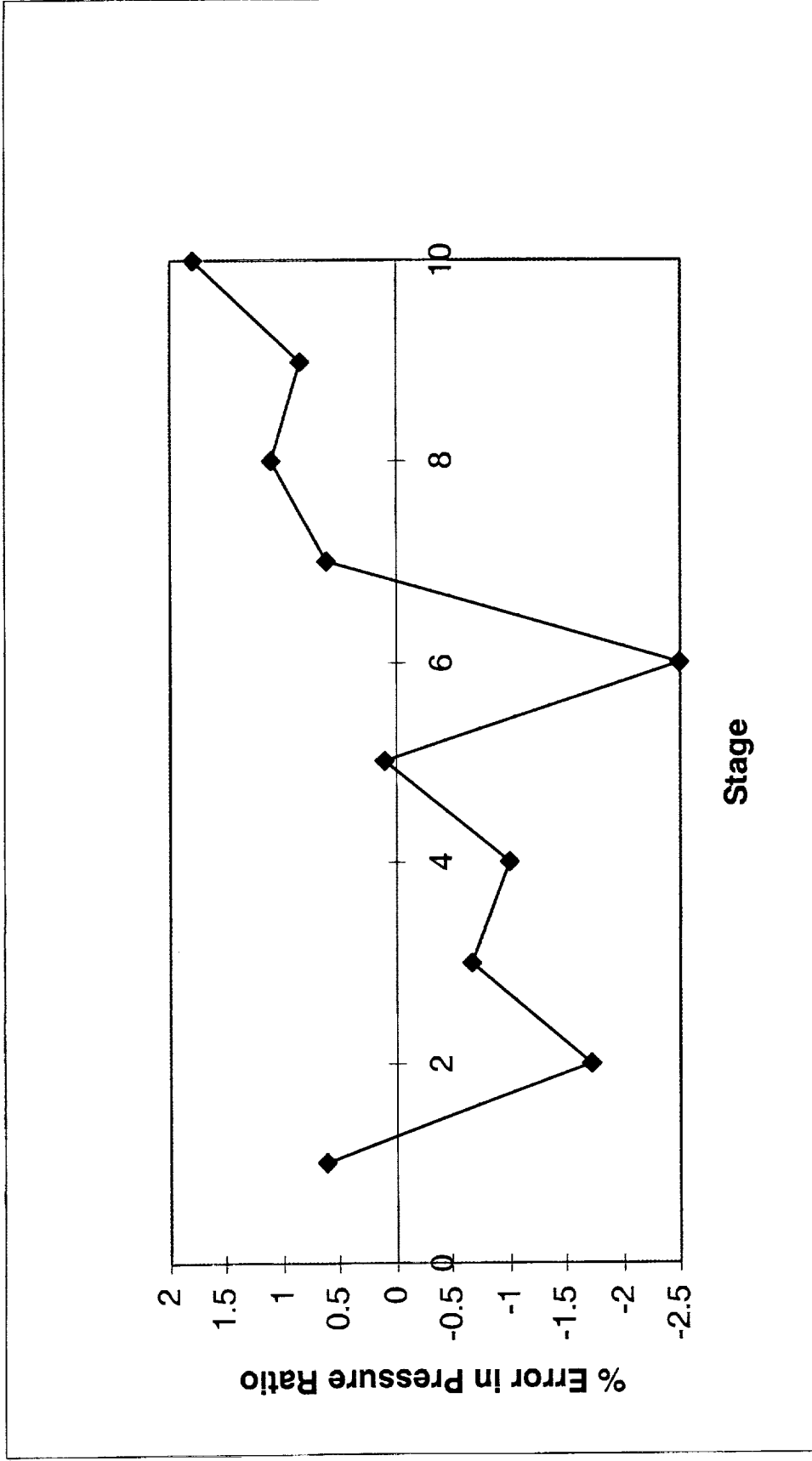
Error is (analysis-test)/test

High Pressure Compressor Rig

Stage Pressure Ratio along a Speed Line
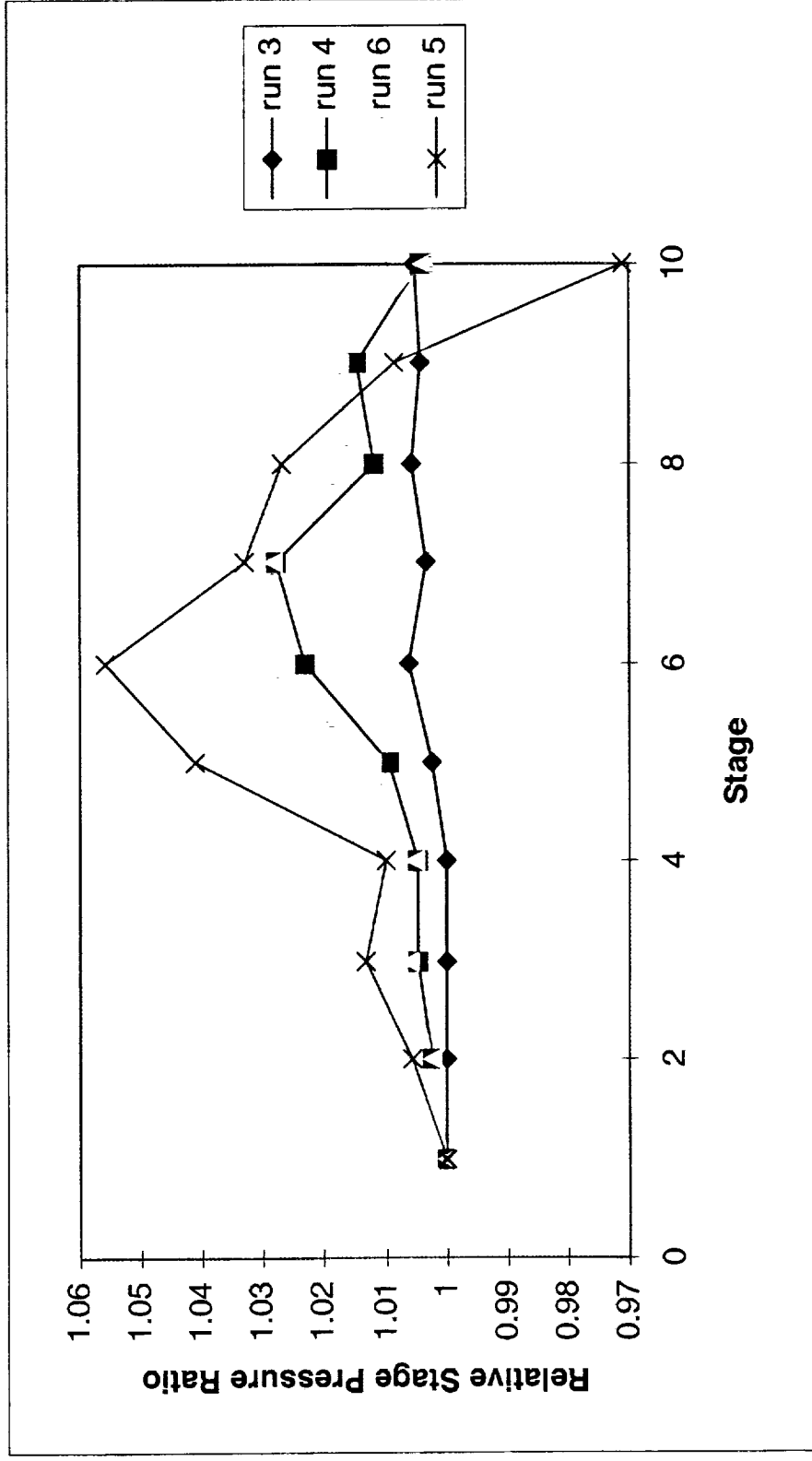
As the machine is throttled, the back end stops pumping just like test.
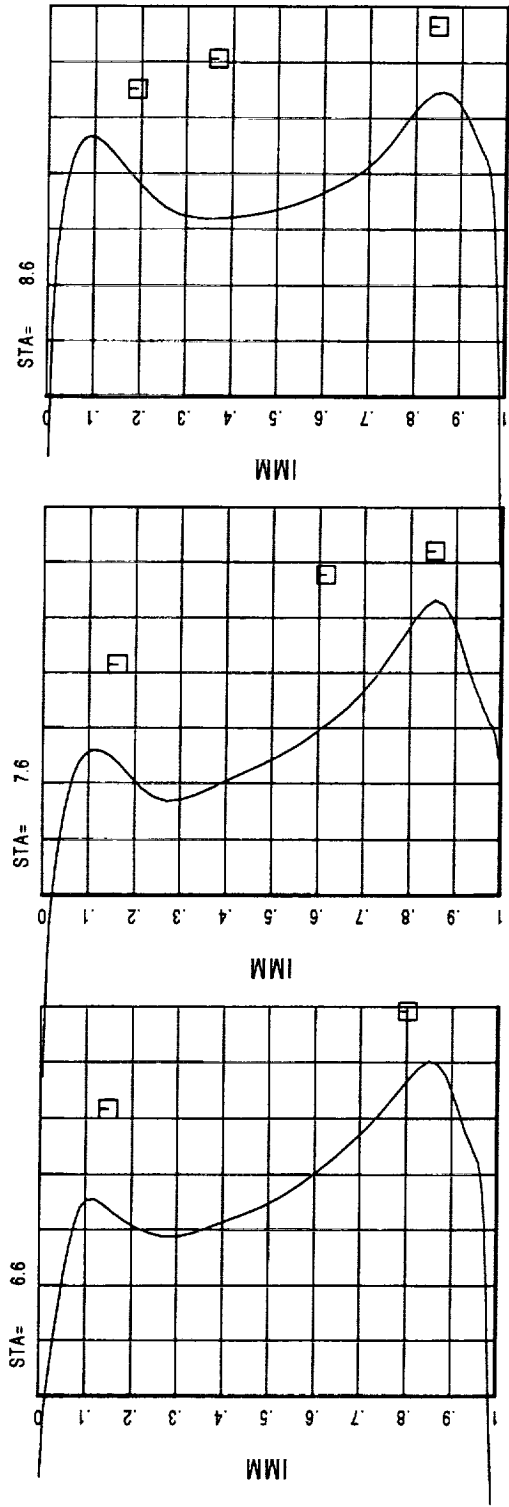
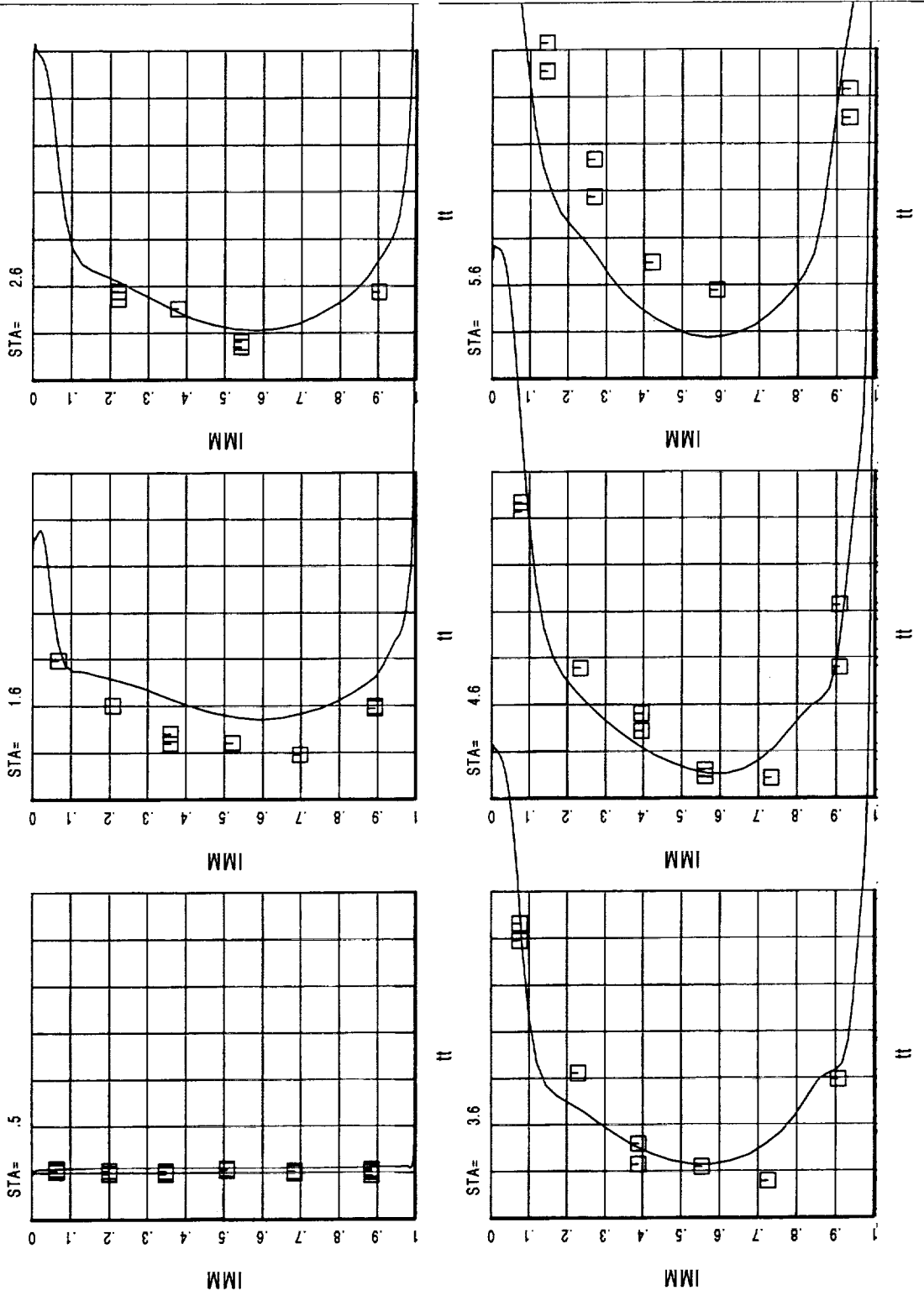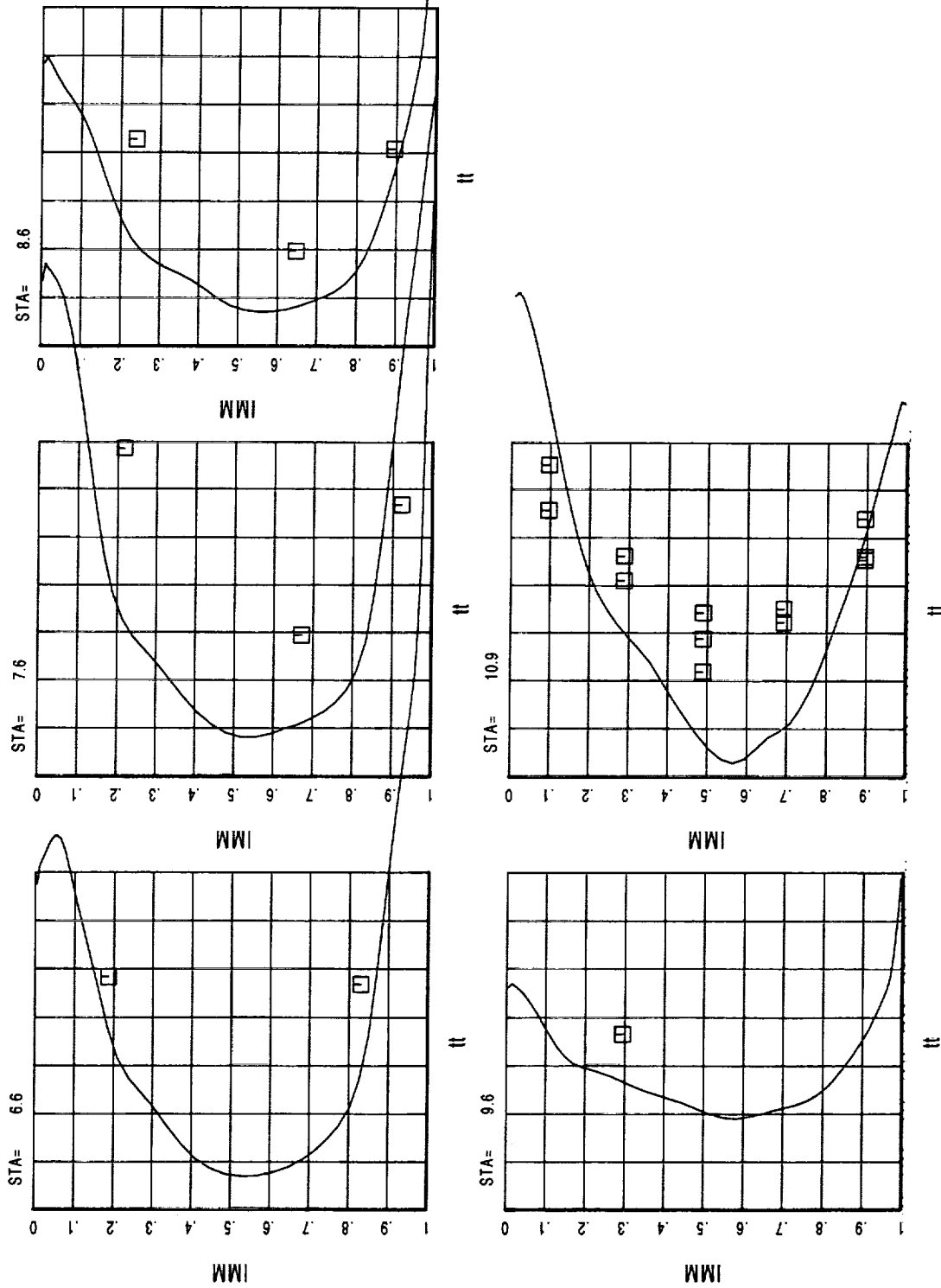# High Pressure Compressor Rig

Effect of Bleed on Pressure Ratio
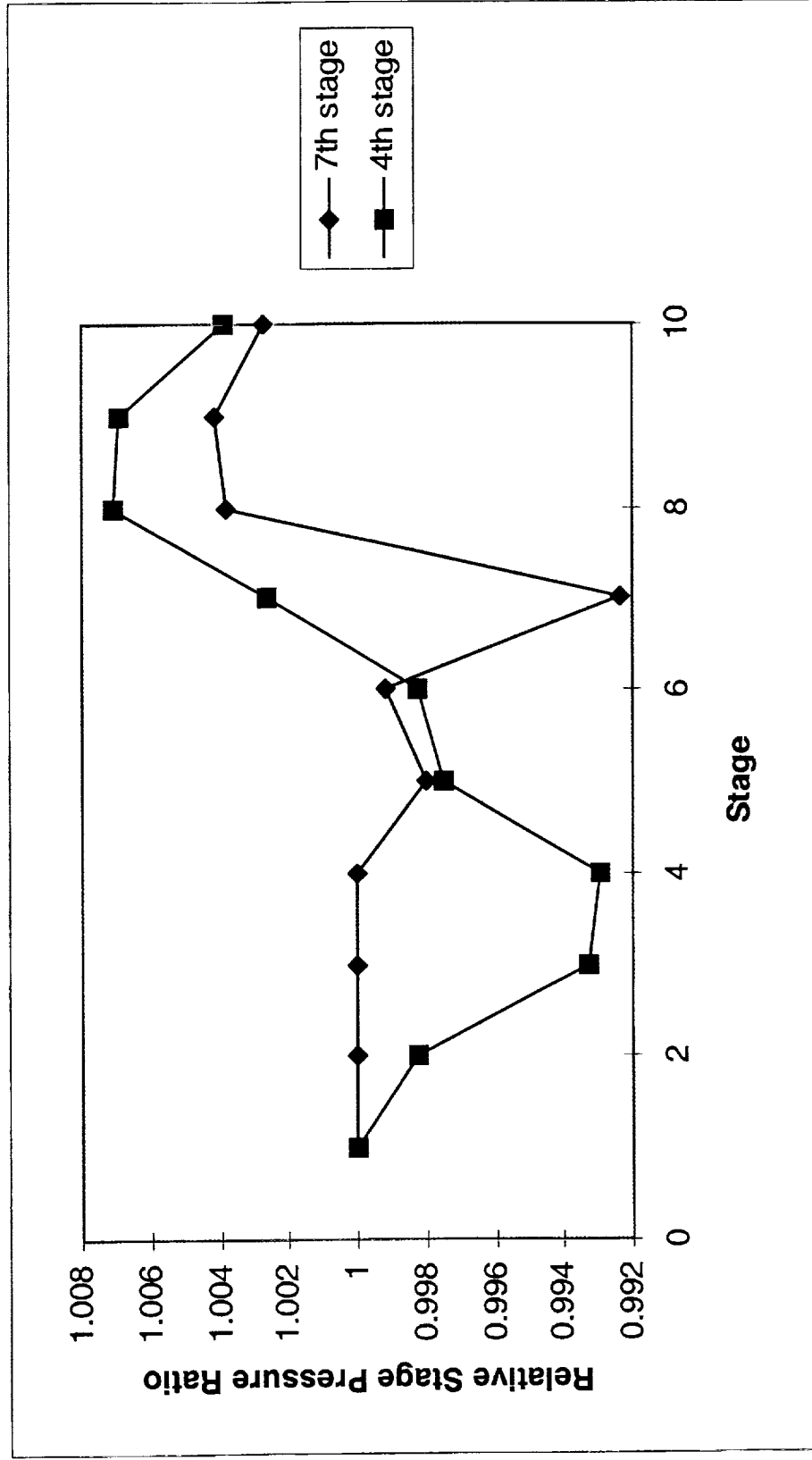
High Pressure Compressor Rig
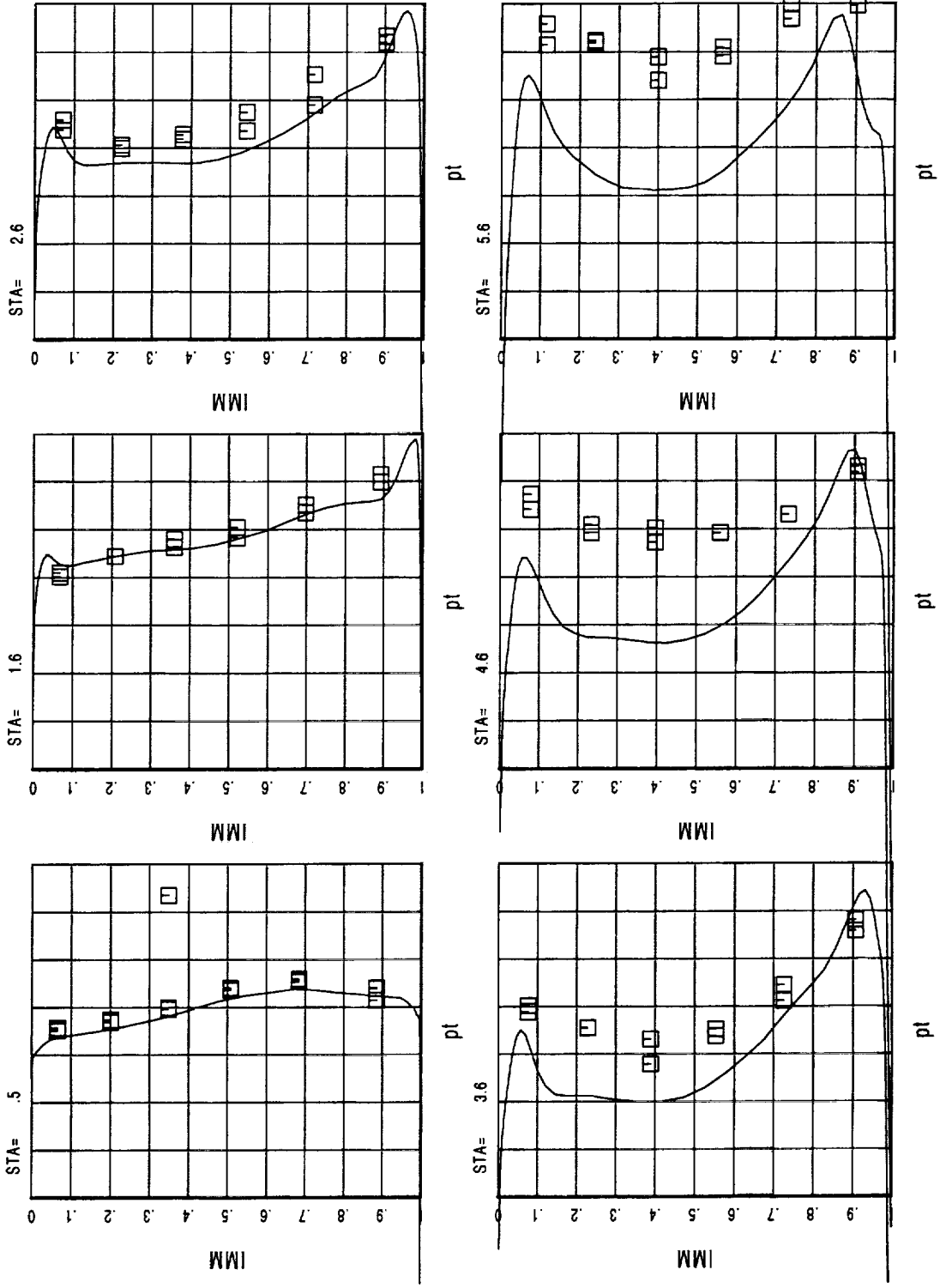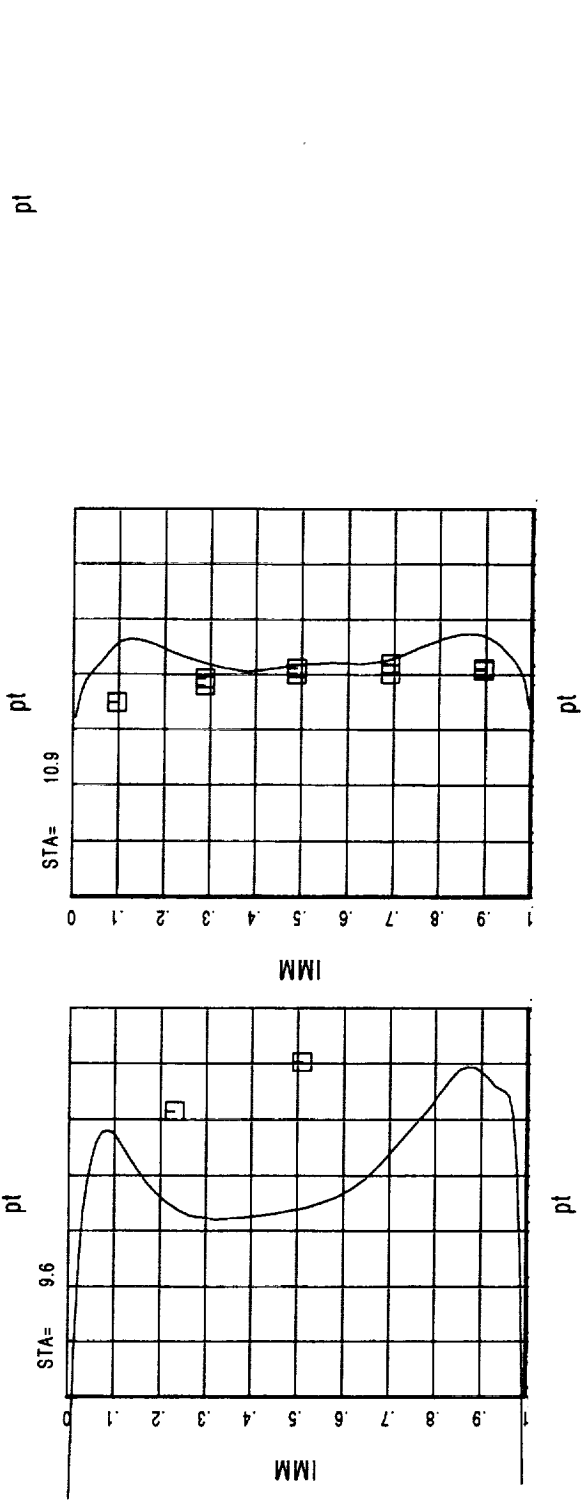
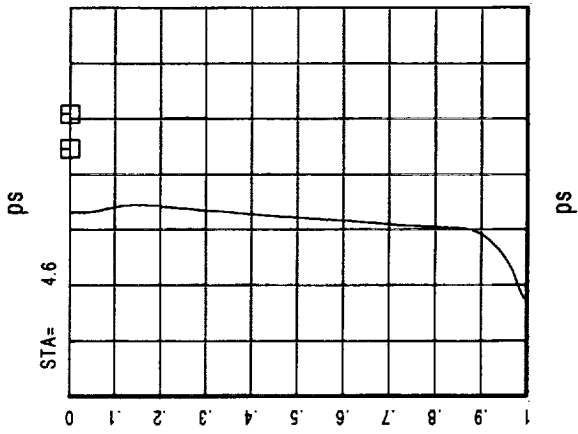*GE Aircraft Engines*

High Pressure Compressor Rig

High Pressure Compressor Rig

High Pressure Compressor Rig

GE Aircraft Engines

High Pressure Compressor Rig

GE Aircraft Engines

High Pressure Compressor Rig
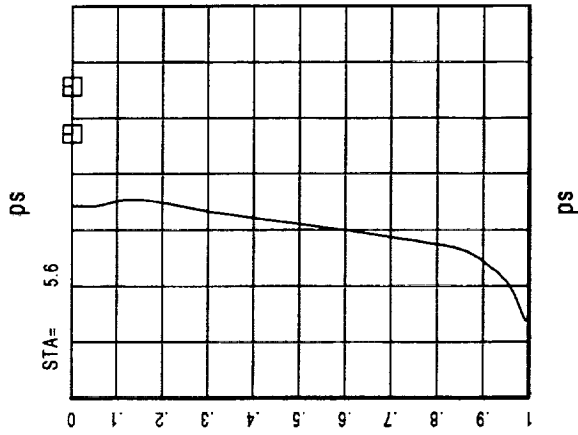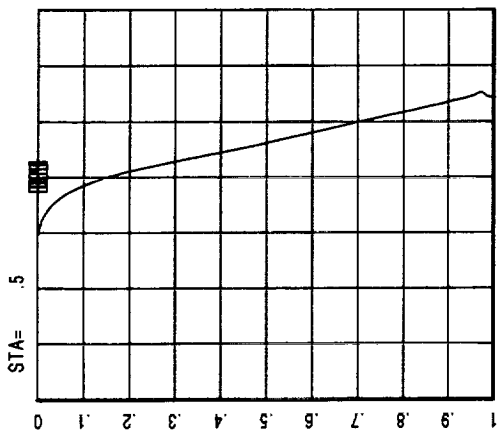
GE Aircraft Engines

High Pressure Compressor Rig

GE Aircraft Engines
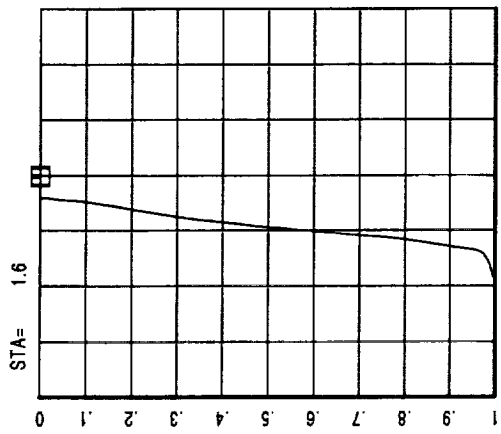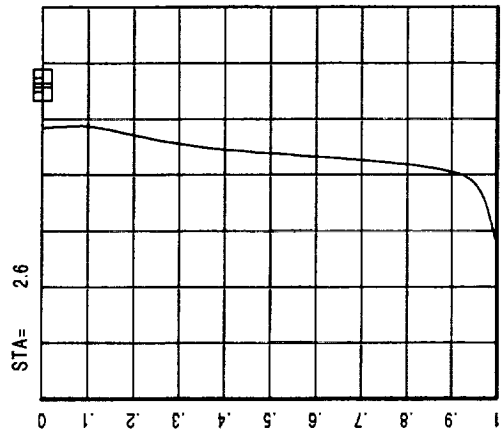
High Pressure Compressor Rig

GE Aircraft Engines
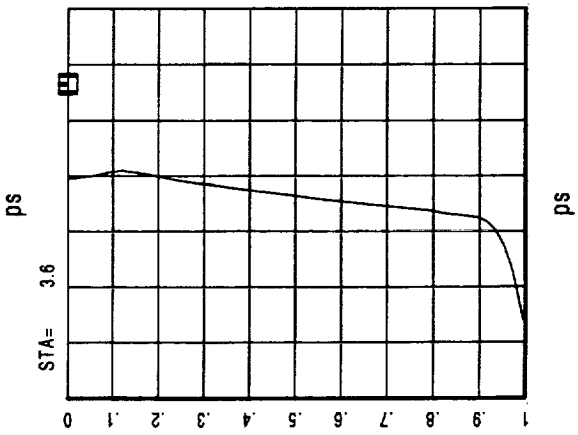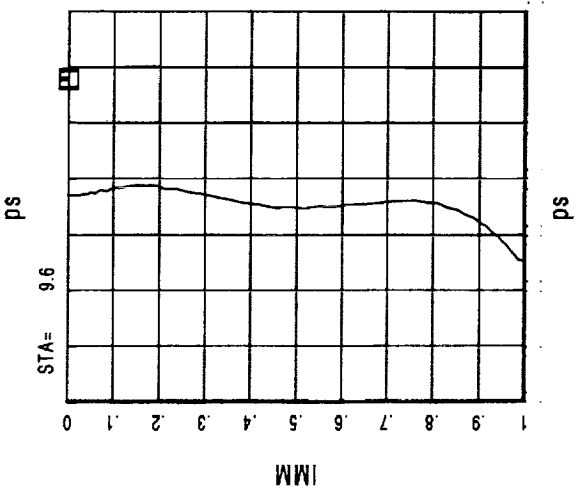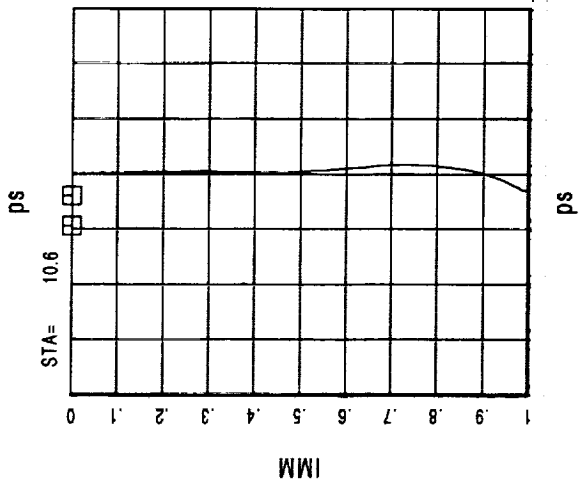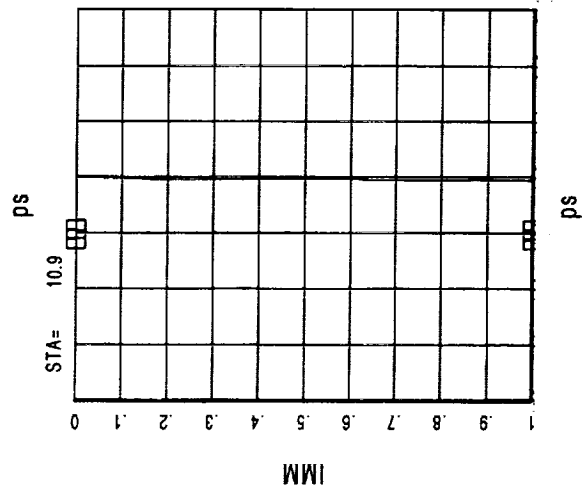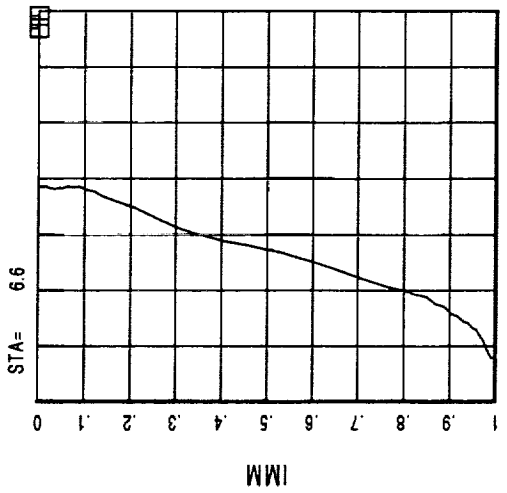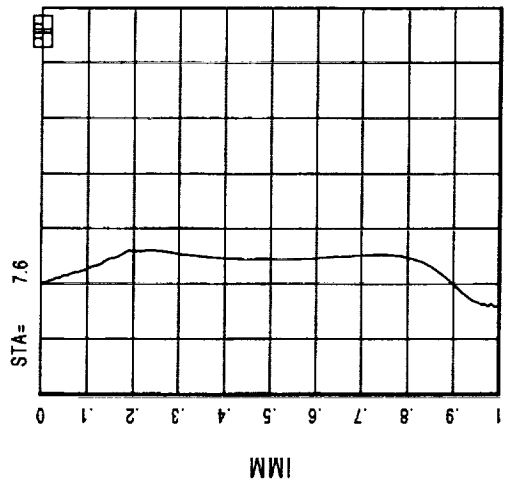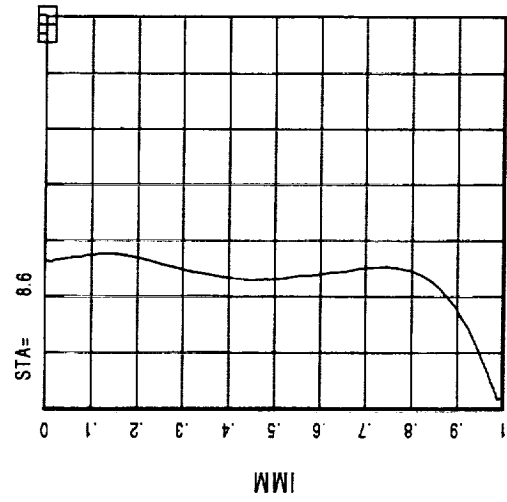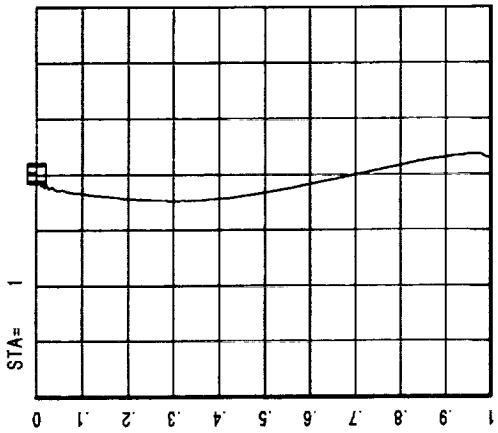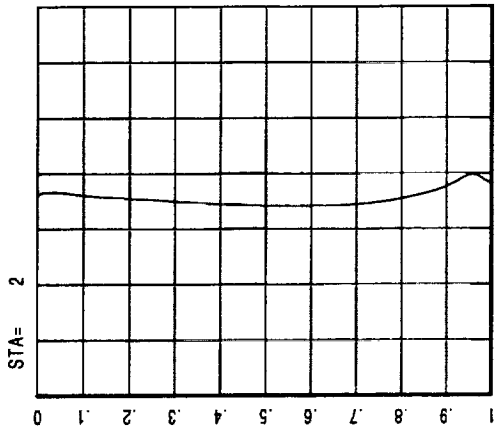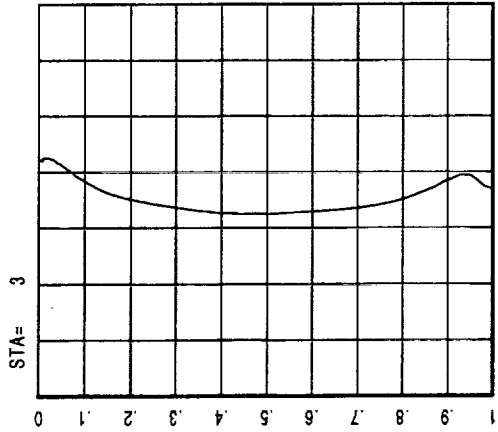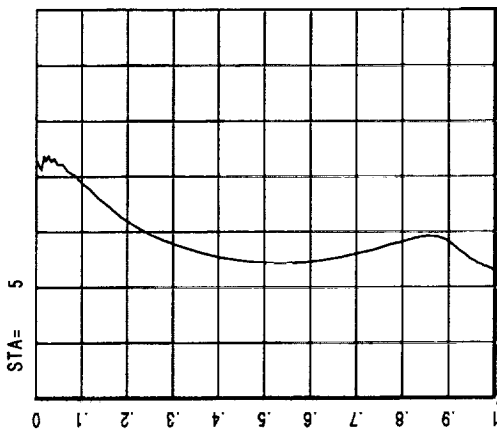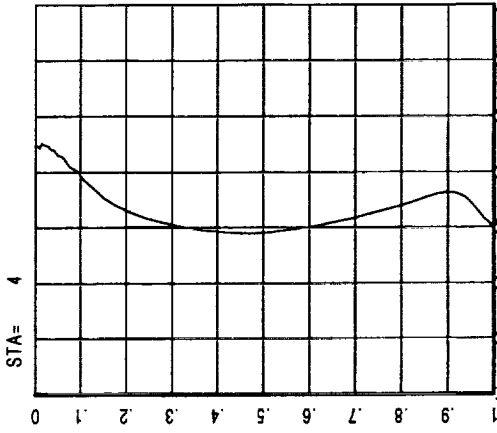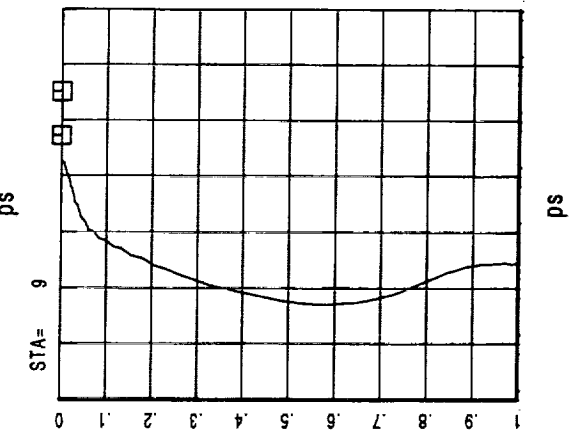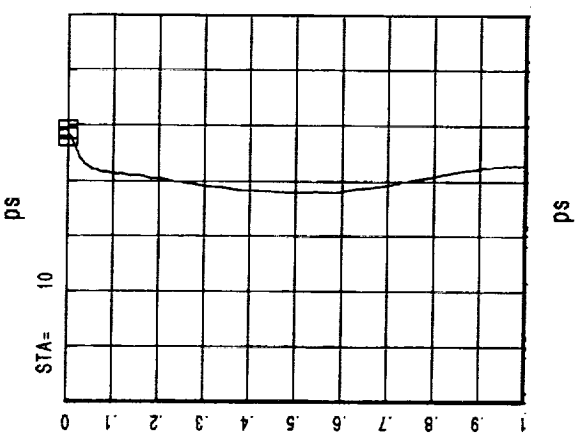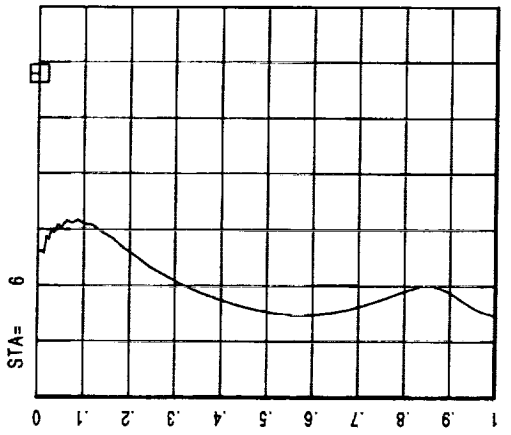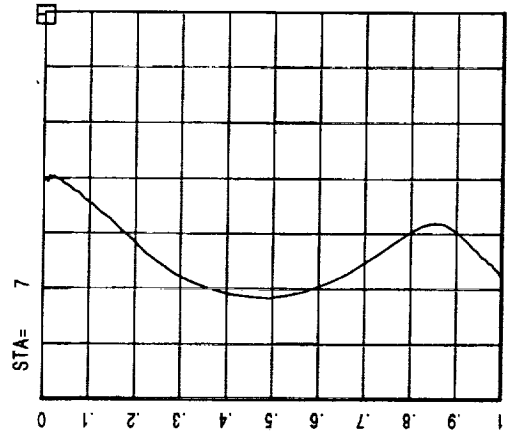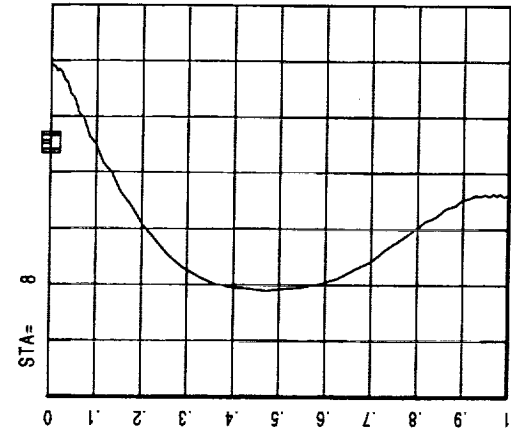
GE90 FETT FAN

Total Pressure at Booster S1 Leading Edge

Total Pressure (psi)

Immersion

GE Aircraft Engines

Slide 18
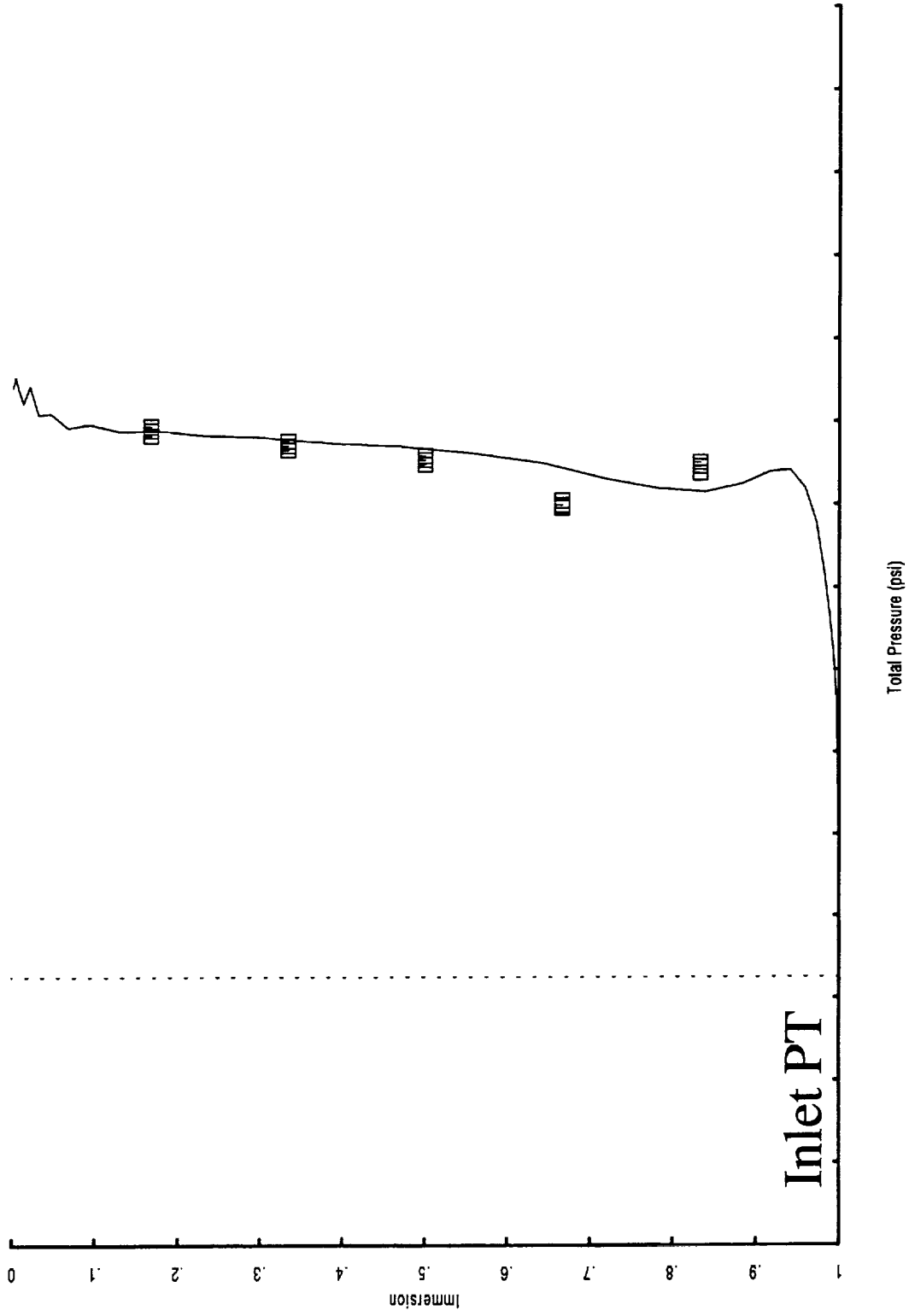
GE90 FETT FAN

Total Temperature at Booster S1 Leading Edge

Inlet TT

Total Temperature (R)

Immersion

GE Aircraft Engines

Slide 19

50

GE90 FETT FAN

Inlet PT

Immersion

Total Pressure (psi)

GE90 FETT FAN

Total Temperature (R)

Immersion

Inlet TT

GE Aircraft Engines

Slide 21

GE90 FETT FAN

Inlet PT

Total Pressure (psi)

Immersion

0 .1 .2 .3 .4 .5 .6 .7 .8 .9 1

GE Aircraft Engines

Slide 22

GE90 FETT FAN

Inlet TT

Immersion

Total Temperature (R)
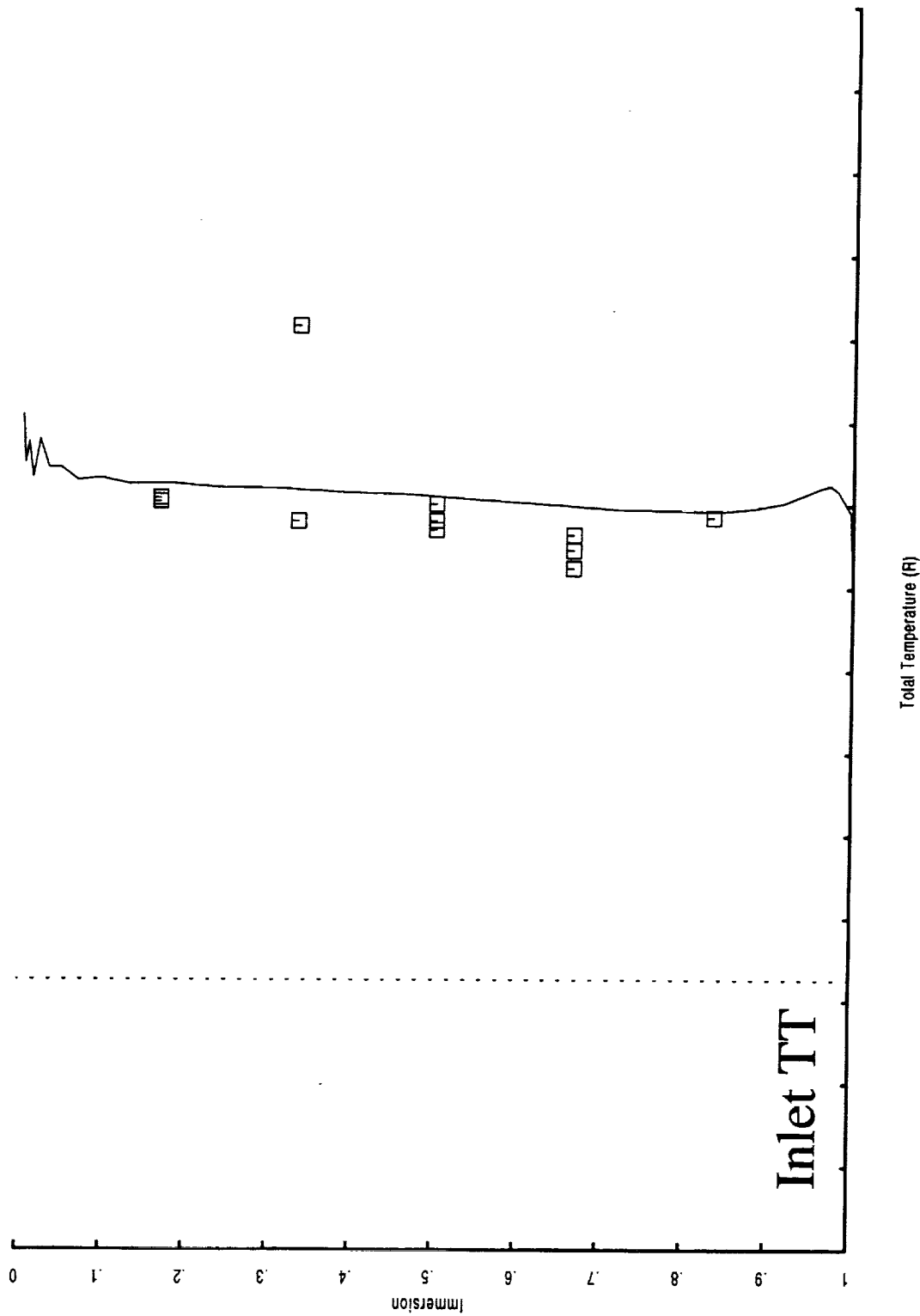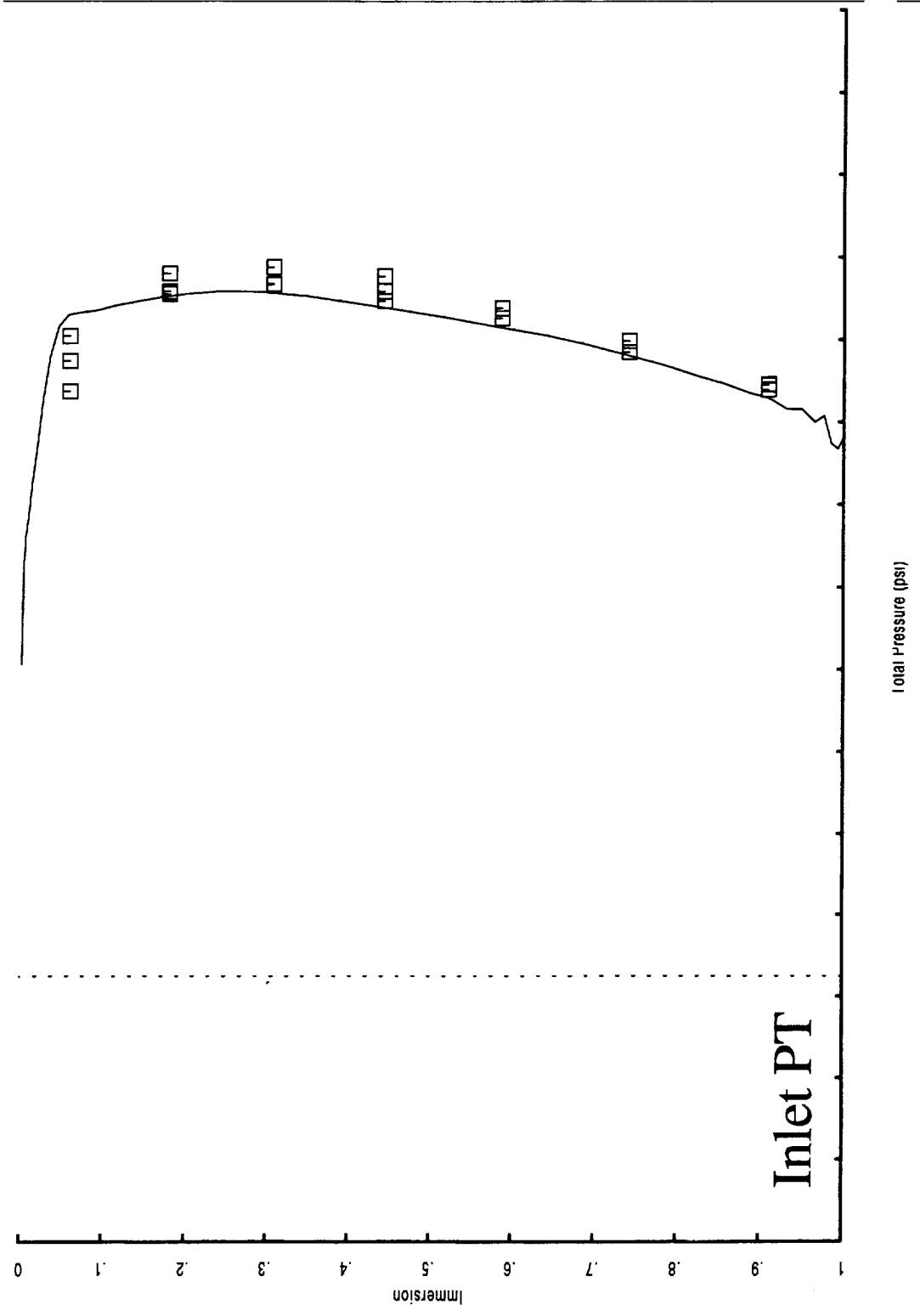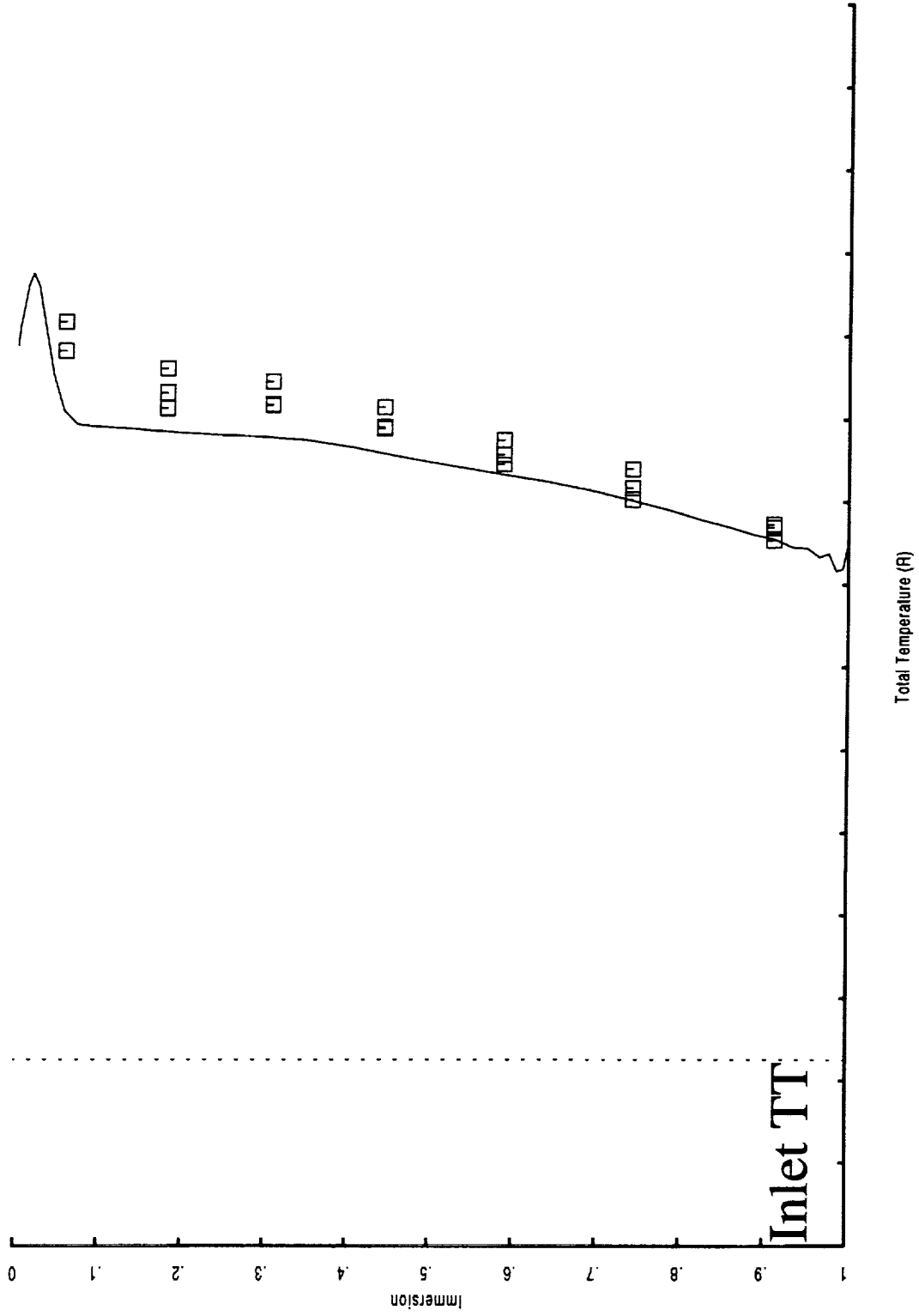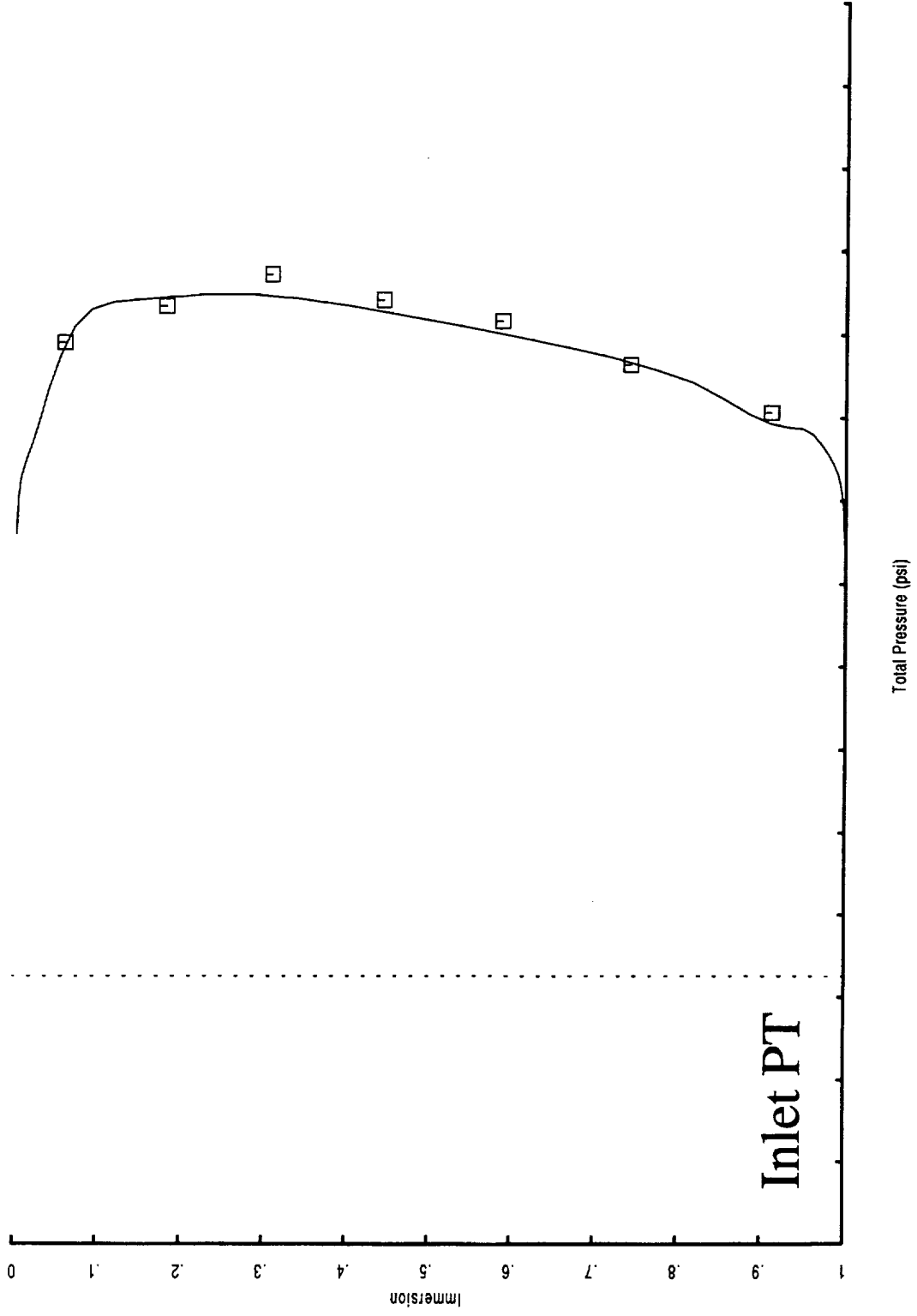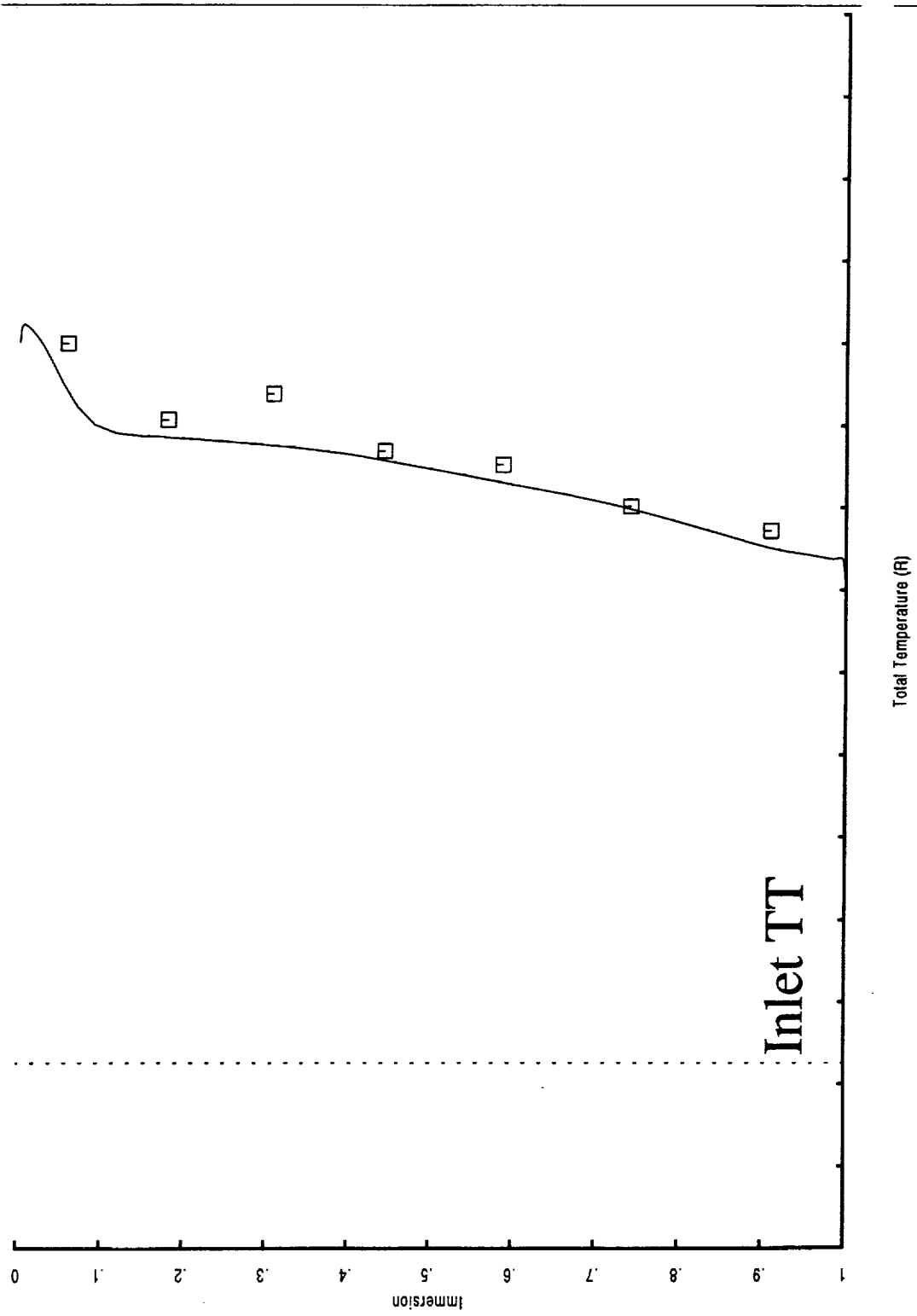
GE90 Fan & Booster

- Set up for Running to Full Engine Cycle Conditions
- 10 blade row solution, Fan, OGV, 3 stage Booster, Strut
- Gridded by Tim Beach using APG
- Run by Mark Celestina using Version 5
- Pylon not Modelled
- Core run to flow
- Bypass run to Static Pressure
- Run 150 flips
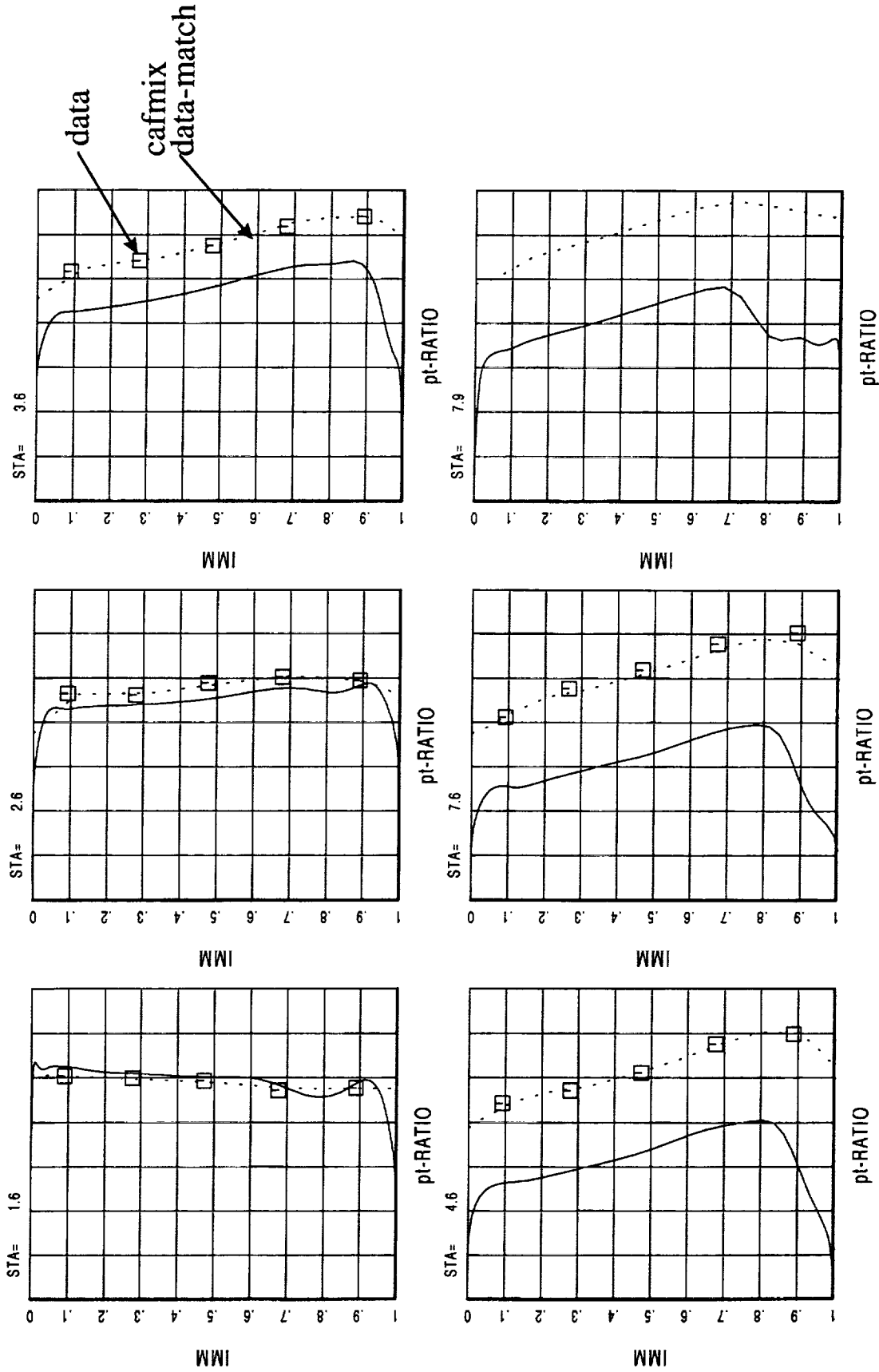
GE90 Fan & Booster

APNASA solution run to Engine Conditions, Not Rig Conditions

GE Aircraft Engines

Slide 25

GE90 Fan & Booster

data

cafmix
data-match

STA= 3.6   tt-RATIO

STA= 2.6   tt-RATIO

STA= 1.6   tt-RATIO

STA= 7.9   tt-RATIO

STA= 7.6   tt-RATIO

STA= 4.6   tt-RATIO

IMM

APNASA solution run to Engine Conditions, Not Rig Conditions

GE Aircraft Engines

Slide 26
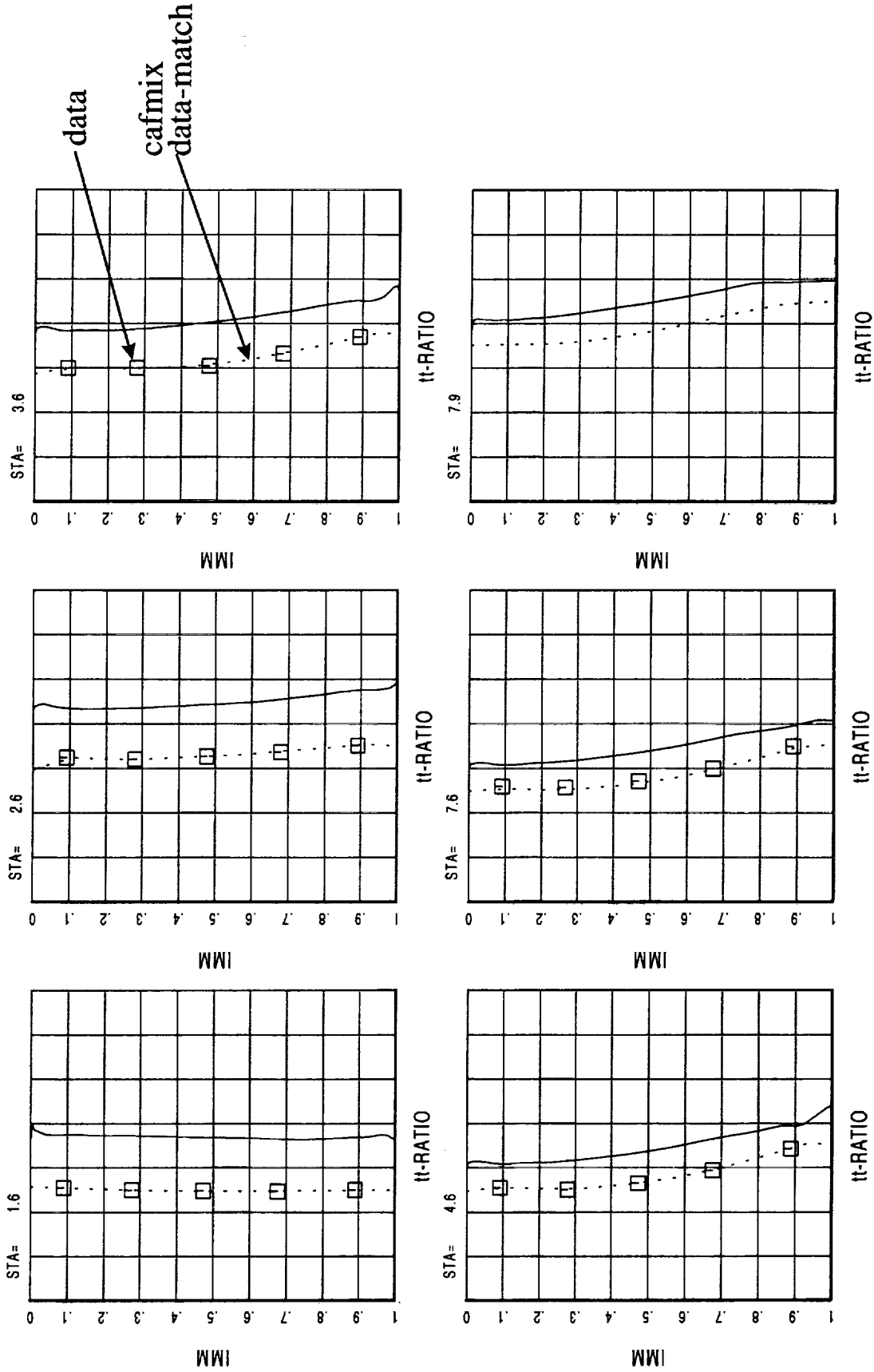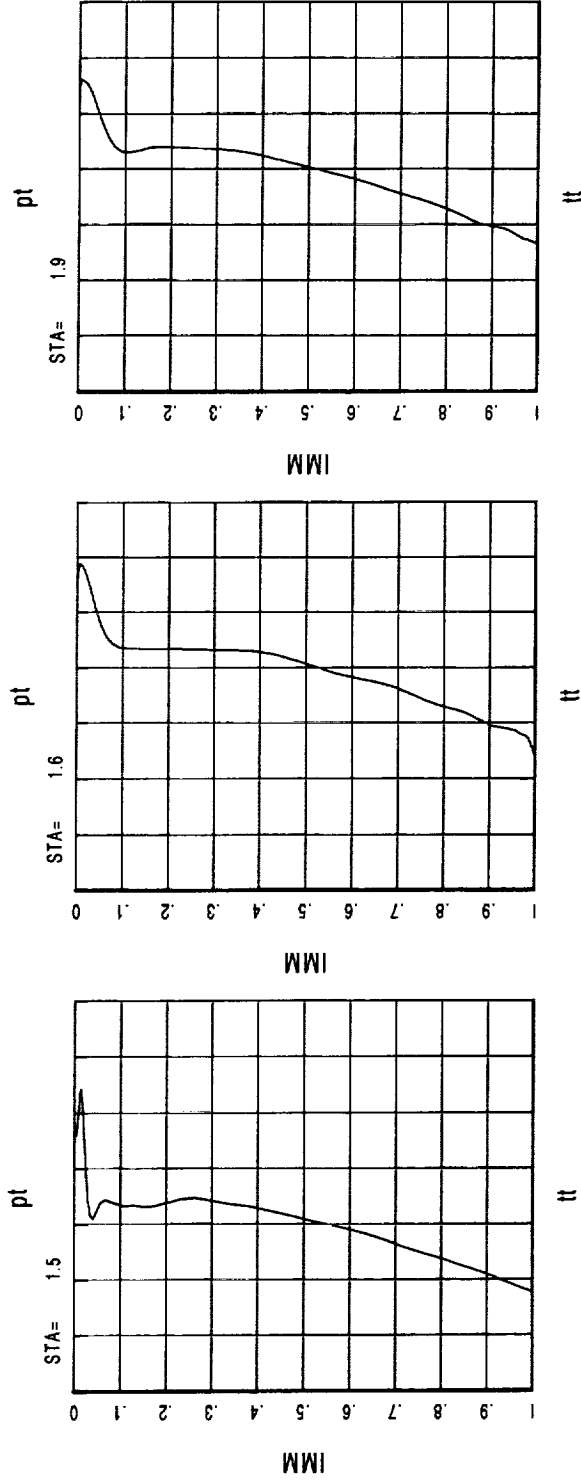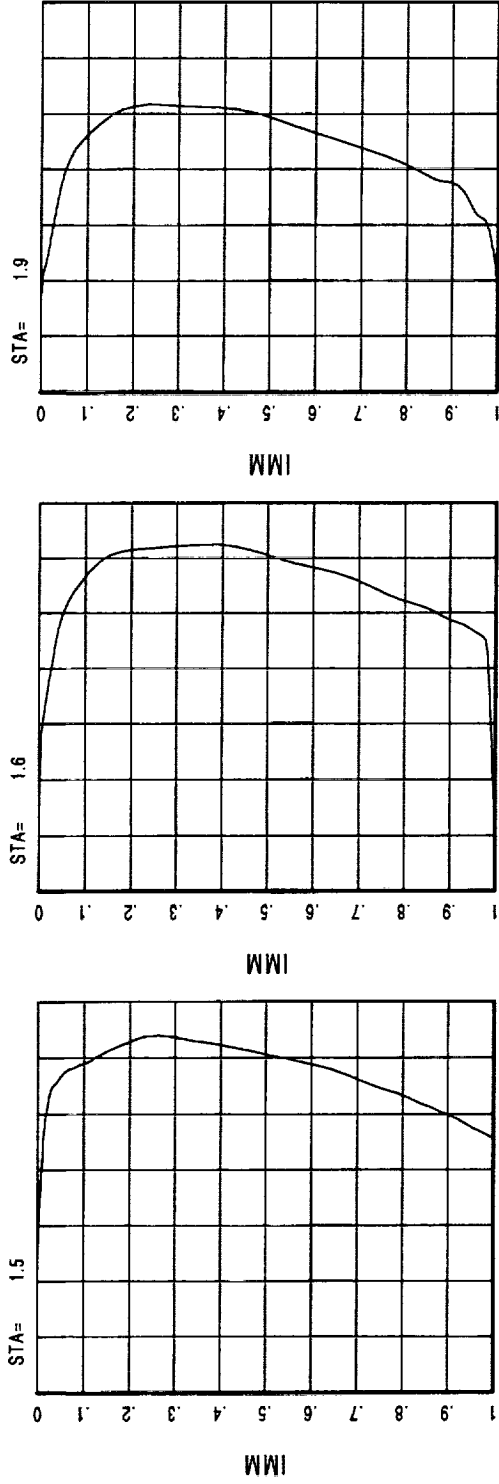
GE90 Fan & Booster

fan trailing edge   OGV leading edge   OGV trailing edge

GE90 Fan & Booster

Exit of Booster

	Difference Between Cycle and APNASA
Pressure Ratio	5.3%
Temperature Ratio	1.3%
Mass Flow (lbm/sec)	0.09%

Exit of Fan

	Difference Between Cycle and APNASA
Pressure Ratio	0.10%
Temperature Ratio	0.38%
Mass Flow (lbm/sec)	1.78%

GE Aircraft Engines

GE90 Compression System

- Set up for Running to Full Engine Cycle Conditions
- 31 blade row solution
- Gridded by Tim Beach using APG
- Being run using APNASA Version 5 by Kevin Kirtley
- Pylon not Modelled
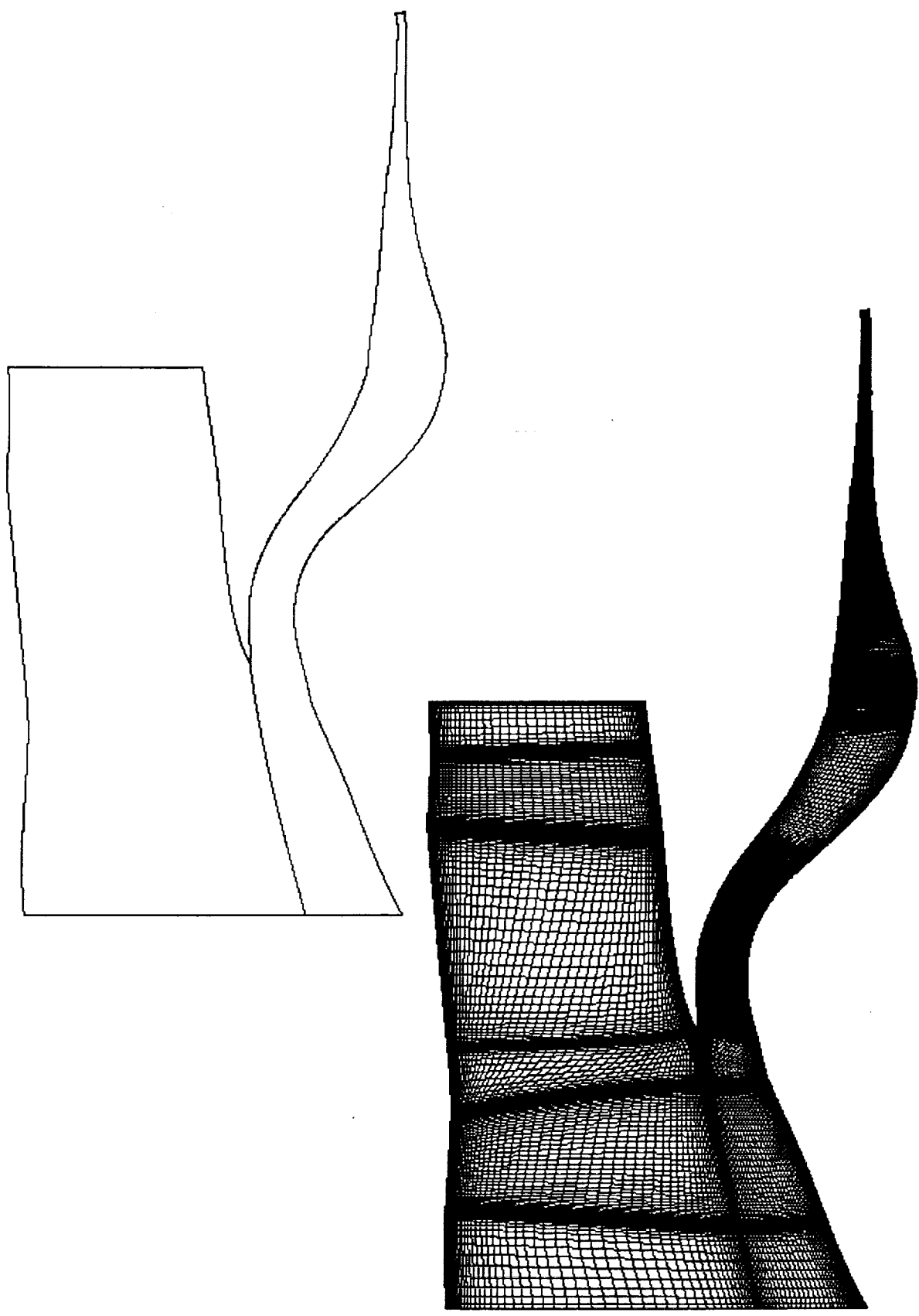
60

GE Aircraft Engines

GE90 Compression System

GE90 Compression System
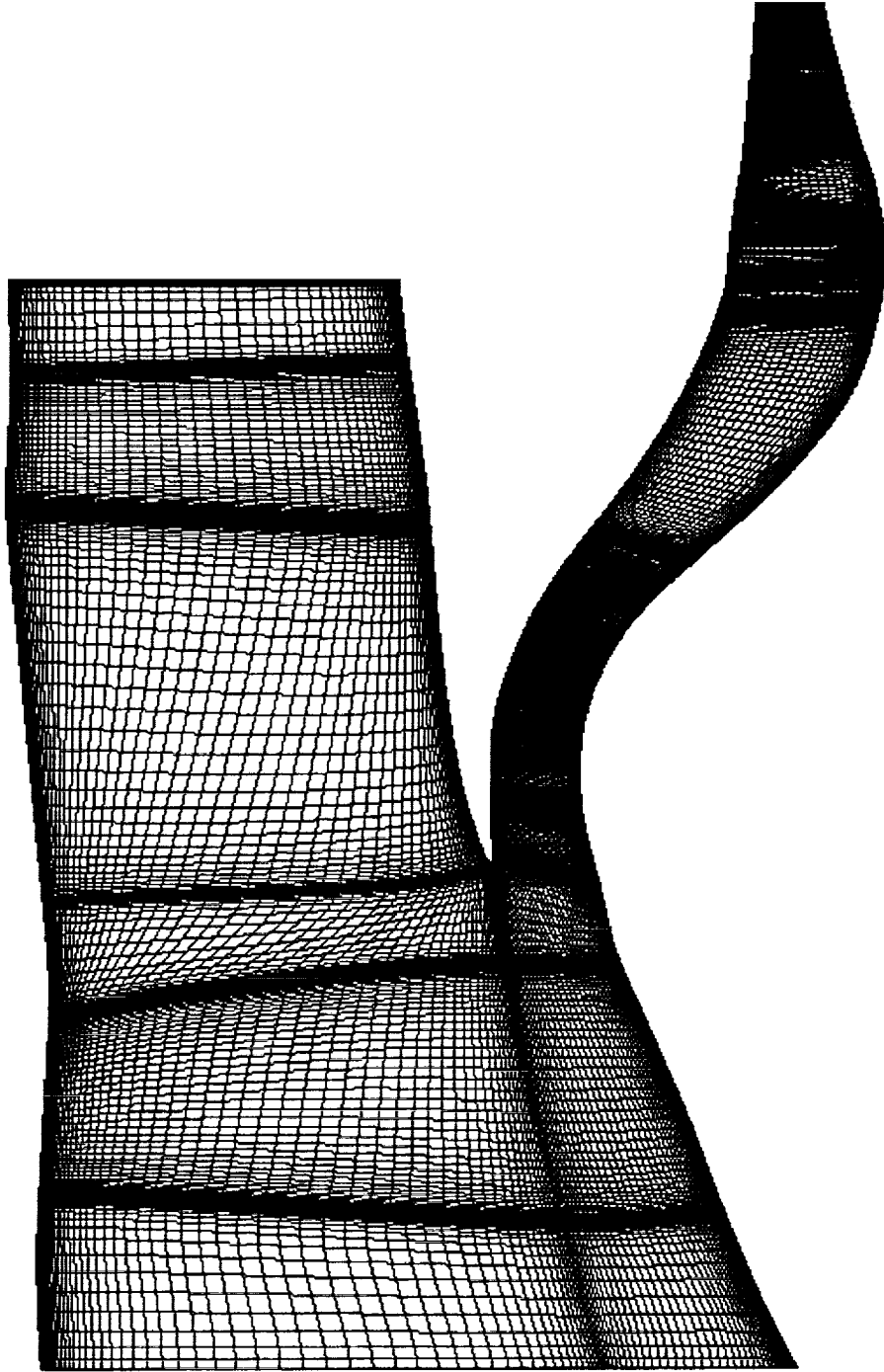
GE90 Compression System
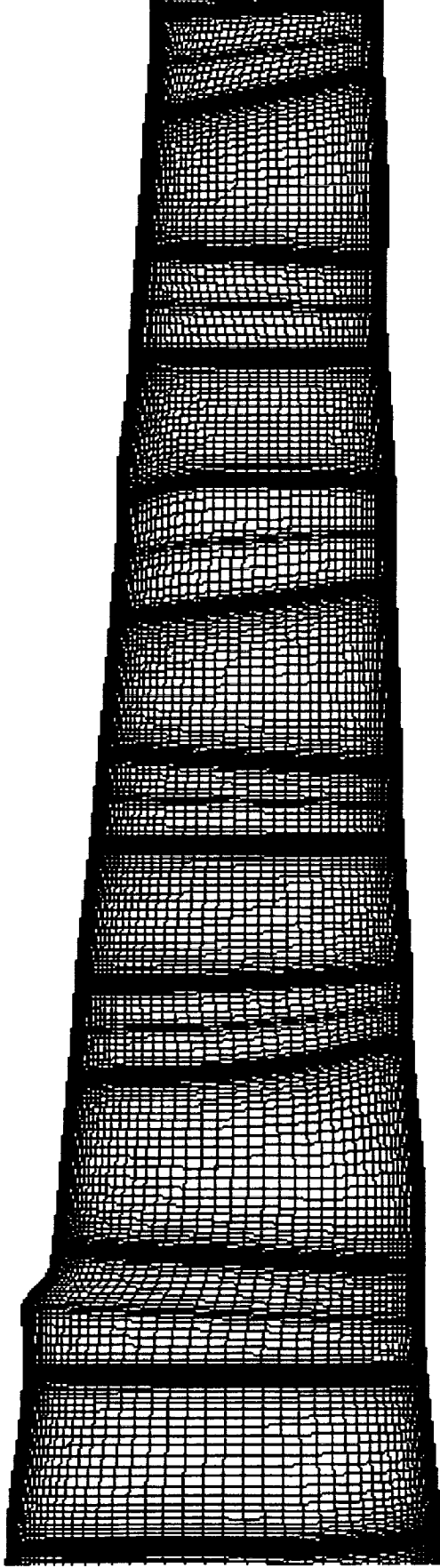
Appendix D

"Multistage Simulations of the GE90 Turbine"

to be presented at the 1999 ASME IGTI conference

MULTISTAGE SIMULATIONS OF THE GE90 TURBINE

Mark G. Turner
GE Aircraft Engines
Cincinnati, OH

Paul H. Vitt
ASE Technologies
Cincinnati, OH

David A. Topp, Sohrab Saeidi, Scott D. Hunter, Lyle D. Dailey
GE Aircraft Engines
Cincinnati, OH

Timothy A. Beach
Dynacs Engineering Co.
Cleveland, OH

ABSTRACT

The average passage approach has been used to analyze three multistage configurations of the GE90 turbine. These are a high pressure turbine rig, a low pressure turbine rig and a full turbine configuration comprising 18 blade rows of the GE90 engine at takeoff conditions. Cooling flows in the high pressure turbine have been simulated using source terms. This is the first time a dual-spool cooled turbine has been analyzed in 3D using a multistage approach. There is good agreement between the simulations and experimental results. Multistage and component interaction effects are also presented. The parallel efficiency of the code is excellent at 87.3% using 121 processors on an SGI Origin for the 18 blade row configuration. The accuracy and efficiency of the calculation now allow it to be effectively used in a design environment so that multistage effects can be accounted for in turbine design.

INTRODUCTION

The high pressure turbine (HPT) of a modern turbofan engine must operate in an extreme environment of high temperature, high stress, and high speed. As such, it must be film cooled and designed for long life and high efficiency. The heat transfer design requires a detailed knowledge of the gas side temperatures. The low pressure turbine (LPT) is designed for very high efficiency and must be able to operate effectively behind the HPT. The requirements for both the HPT and LPT necessitate a detailed aerodynamic solution capability which accounts for the film cooling, multistage effects and variable gas properties.

The Average Passage Approach developed by Adamczyk (1986) has been generalized for improved grids by Kirtley. Turner and Saeidi (1999) and applied to the complete turbine for the GE90 turbofan engine. In preparation for doing the full turbine, the HPT and LPT rig configurations were first validated. These rigs were designed and tested as part of the GE90 development program. A three quarter scale rig of the 2 stage GE90 HPT was designed and built by GE and tested at the NASA Lewis Research Center. A half scale rig of the 6 stage GE90 LPT was designed and built by GE and Fiat and tested at GE. These rig tests produced detailed measurements of hub and casing static pressures and inlet and exit profiles of total pressure, total temperature and flow angles. The engine turbine simulation was set up based upon a cycle analysis of the GE90 engine at takeoff. The HPT rig simulation comprised 4 blade rows; the LPT rig was 14 blade rows including the mid frame strut and OGV, and the full turbine simulation comprised all 18 blade rows.

The present work was undertaken for three reasons:

1. To support a full engine simulation of the GE90 in order to demonstrate the capability of high fidelity 3D analysis for a complete turbofan application. This would allow an analysis of the primary flowpath when coupled with the full compression system and a model

of the combustor,. This represents the first time a dual-spool cooled turbine has been analyzed using a 3D multistage solver.

2. To determine the differences between a turbine running at warm air rig conditions and that running in an engine. For the HPT, this involves a severe inlet temperature profile at elevated temperatures. For the LPT, this involves the interaction with the upstream HPT which produces profiles of temperature, pressure and flow angles. The amount of cavity purge flows in an engine application were also much greater than in the LPT rig, which greatly modifies the hub aerodynamics in the LPT.

3. To validate the method for application in turbine design by simulating real turbine hardware.

This paper describes the features of the code, APNASA, including film cooling and the variable gas model used. It also presents the method of simulating leakage flows due to purge cavity flows, nozzle under shroud leakages and rotor over shroud leakages. Following this, the HPT rig, the LPT rig and the full engine configurations will be described. Results for these simulations will then be presented with particular emphasis on multistage effects and differences between rig and engine simulations. Following the results is a description of the parallel capability of the solver when applied to the 18 blade row full turbine configuration.

METHODOLOGY

Three methods have been used by researchers for multistage analysis. These include the mixing plane approach as described by Dawes (1990), the average passage approach of Adamczyk (1986), and the fully unsteady approach similar to Chen. Celestina and Adamczyk (1994). A full unsteady analysis for a problem of this scale is still beyond the computing capability currently available. The mixing plane approach produces an entropy jump at the mixing plane as demonstrated by Fritsch and Giles (1993). Especially for HPT turbines with large circumferential variations, this can lead to large errors. Therefore, the average passage approach has been used to simulate the multistage environment of the turbine. This has been shown by Turner (1996) to work well for an LPT application. The ability of this approach to capture most of the multistage effects is presented by Adamczyk (1999).

Numerical Scheme

The foundation of the Navier-Stokes solver is an explicit 4 stage Runge-Kutta scheme with local time stepping and implicit residual smoothing to accelerate convergence. Second and fourth difference smoothing as applied by Jameson (1984) is employed for stability and shock capturing. A k-ε turbulence model is solved using an implicit upwind approach similar to that presented by Turner and Jennions (1992) and Shabbir et. al. (1997). Wall functions are employed to model the turbulent shear stress adjacent to the wall without the need to resolve the entire boundary layer.

The solver has been parallelized using MPI (Message Passing Interface) to share information across domain boundaries. Domain decomposition is accomplished "on the fly" by subdividing the grid in the axial direction into an arbitrary number of domains specified in the argument list. The number of parallel bugs has been reduced or totally eliminated by strict adherence to keep the parallel code equal to serial (within numerical precision). The overall solver has two levels of parallel capability as shown in Figure 1. The first level is to solve each blade row in a multistage component. The next level is to solve each blade row on several processors.

All blade rows are run for 50-100 Runge-Kutta iterations, at which time the body forces and deterministic stresses are calculated and written to a file. This is one outer iteration, or flip. At this time, the files are distributed to the other blade rows to update the multistage effects.

Average Passage Approach with Generalized Closure

A more general form of the average passage closure first developed by Adamczyk (see Adamczyk, Celestina and Mulac (1986)) has been developed by Kirtley, Turner and Saeidi (1999). It allows for non-pure H grids, as shown in Figure 2 for the GE90 HPT rotor 1. These grids have been generated using APG, a grid generator specially designed for the Average Passage Code with the generalized closure implementation. Compared with the pure H-grids required by the previous closure implementation, these grids allow much better leading and trailing edge orthogonality and resolution which improves accuracy and the convergence rate. The closure requires overlapping grids so that the deterministic stresses from one blade row are applied to other blade rows. This allows blade row interactions such as spanwise mixing of temperature, wake blockage and potential field blockage due to blunt leading edges to be modeled.

The desired near wall grid spacing can be characterized by the dimensionless quantity y^+ which should be approximately 30 when wall functions are used. Grid generation was carried out with this goal in mind, while also balancing the need for good leading and trailing edge resolution. The actual y^+ values on the pressure surface of Nozzle 1 were approximately 20. Tip gaps over the unshrouded HPT rotors have been modeled with 4 cells. Periodicity is applied across a void representing an extrusion of the blade to the casing. Overall grid resolution has been set based on a detailed grid study of the LPT nozzle 1 as an isolated blade row. Grids were chosen which produced accurate flowrate and loss calculations. This gridding approach was then applied for all blade rows. The resulting grids had 50 spanwise grid points. The number of blade-to-blade grid points varied with blade row solidity; 41 blade-to-blade grid points is a representative number. A minimum of 72 points from leading to trailing edge were used. The number of grid points in the axial direction varied depending on the chord and axial gaps of each individual airfoil.

As mentioned, the average passage approach uses overlapping grids. When validating the HP turbine, it was noticed that the extent of that overlap should only be half way through the downstream blade row. If the overlap extends further, the upstream blade row wake produces an entropy decrease which is not plausible and does not compare favorably with the measurements. This is due to the closure not mimicking the true unsteady wake chopping effect. The dominant effect of the downstream blade row is captured by including the front half of the airfoil. This effect is the metal blockage of the downstream airfoil and the bending of the wake streamlines due to the turning of the downstream blade row. The blockage effect of the upstream wake through the first half of the blade row is also still captured. Research is currently underway to correctly model the physics without truncating the grids, but the truncated grid approach can still provide a quality solution if the solution is interrogated correctly. The LPT rig simulation did not suffer from this problem so overlaps of one blade row were used. For the HPT rig and full turbine, a half blade row overlap was used for each blade row.

Model for Real Gas

A model for real gas effects which treats γ (the ratio of specific heats) as a linear function of temperature was presented by Turner

(1996). In that implementation. γ was treated as an axisymmetric quantity. With the new closure implementation, this has been generalized so γ is now a three-dimensional quantity. This is very important for a turbine where the inlet total temperature can vary by 1000 degrees Rankine, and large variations in temperature can occur circumferentially due to wakes and secondary flows . Figure 3 shows how well the linear model compares with the actual real gas for γ, C_p (the specific heat at constant pressure) and H (the enthalpy) for a range of temperatures typical in an HPT at takeoff conditions. These quantities are also shown assuming a perfect gas at constant γ, resulting in a large enthalpy shift. With cooling flows modeled as sources of mass, momentum and energy, this allows the cooling flow to enter at the correct enthalpy level in order to achieve the correct energy balance.

One other assumption which has been used is that the ideal gas constant, R, is constant. For a cooled turbine in an engine environment, there are products of combustion in the flow entering the first stage turbine nozzle, However, the cooling flow does not have these products of combustion. This gas property difference leads to a different R. The energy source term of the cooling flow described below accounts for this effect, although this leads to erroneous coolant film temperatures and other errors. A more correct approach is to track the products of combustion with a species equation and use a variable R. This has not yet been implemented so an average R for the turbine has been used.

Source Terms to Represent Cooling Flow

A source term approach described by Hunter (1998) is used to simulate the film cooling on the cooled airfoils, the endwalls and for some of the gaps with purge cavity flows. Sources of mass, momentum, energy and the turbulence quantities are specified in each cell adjacent to a surface with film injection. A row of cooling holes is actually modeled as a slot because the grid is not fine enough to capture the effect of each discrete film hole. Several inputs are required to specify the source terms. These include the coolant mass flow, the geometric angles of the hole centerline, the hole size, the coolant supply temperature, an approximate discharge static pressure, the turbulence intensity and the turbulent length scale of the coolant. With this information, the mass flux, energy flux, turbulent kinetic energy flux, turbulent dissipation flux and the total momentum flux can be determined. The source term in a cell is then set to the calculated flux. The unit vector of the momentum flux is specified tangent to the hole centerline. so the momentum flux in all three directions can be specified. This approach picks up the macroscopic effects of film cooling so the overall mass, momentum and energy are correct with the momentum applied at the correct angle relative to the blade or endwall surface. Figure 4 shows the contours of absolute total temperature on the pressure side of HPT nozzle 1 for the engine configuration. Clearly visible are the rows of cooling holes.

Leakage Model

In addition to the source term approach, there is a method to specify endwall leakage due to shroud leakage and purge flows. This method is applied as a code input. It differs from the source term approach in that the axial and radial momentum terms are updated as the solution converges. The leakage model is more straightforward to apply . Figure 5 shows how this model is applied to the under-shroud hub leakage across LPT nozzle 2. The velocity vectors crossing the endwall show where the leakage model has been applied. Also notice

how the hub flowpath has been specified to model the real nozzle hub geometry. The effect of leakage is quite pronounced on the endwall temperature profiles. The amount, temperature and level of swirl for the leakage is input and held fixed as the solution converges. This input can be calculated from an assumed pressure drop across an orifice with a specified flow coefficient. This process has been automated using a proprietary labyrinth seal analysis code that requires the clearance, pressure drop and seal teeth arrangement as inputs. These leakage flows were then held fixed for the average passage . analysis.

TURBINE SIMULATION CONFIGURATIONS

Figure 6 shows the geometry modeled in this study. For each of the configurations, total pressure, total temperature, the radial flow angle and zero swirl were specified at the inlet. At the exit, the static pressure was specified. For both rig configurations, the design intent geometry was used.

The goal of the rig measurements, the data reduction, and the choice of instrumentation used for these rigs has been to obtain turbine performance. The use of these data for validation of CFD simulations is only a byproduct of this primary goal. The biggest impact is that the energy output of a turbine is measured through a torque measurement of the shaft. Torque times wheel speed gives the power. The temperature measurements are taken to obtain radial variations in temperature and not the absolute level. The variation is obtained accurately without detailed calibration of the thermocouples. This detailed calibration is therefore not done. Static pressure measurements are taken under nozzle platform overlaps in the hub of a turbine. Due to detailed cavity aerodynamics, this is not the flowpath static pressure. In addition, upstream turbulence has not been measured. Upstream turbulence intensity values of 5% have been applied for the HPT and LPT rigs, and 10% for the full engine.

High Pressure Turbine Rig

The HPT rig geometry is shown in Figure 6. It is a ¾ scale cooled rig of the actual GE90 HPT which was designed and built at GE Aircraft Engines and has been tested at a NASA Lewis Research Center test cell. The actual configuration also included the strut and first LPT nozzle. Only the first four blade rows have been analyzed here. A simulation was set up to match the rig test conditions.

Low Pressure Turbine Rig

The LPT rig geometry, shown in Figure 6, is a ½ scale rig which was designed and built by GE and Fiat, and tested at GE. It is a six stage high efficiency LPT. As shown, the turbine center frame and turbine rear frame struts were tested and included in the analysis. This simulation was set up to match the rig test conditions at the LPT design point.

Full Engine Turbine Configuration

The full turbine configuration is shown in Figure 6 at full scale as it exists in the engine. A few changes relative to the rig designs had to be implemented for the production engine. The most notable is that the first stage nozzle throats had to be opened up to allow more flow in the growth production design. Overall boundary conditions and levels of cooling flow were set up using a cycle model of the GE90 at sea level takeoff, and at 0.25 Mach number. This cycle model has

empiricism derived from rig and engine data and represents a good macroscopic view of the engine. The temperature profile at the inlet to the turbine is based on analysis and testing of the GE90 dual annular combustor at takeoff. Detailed distribution of cooling flow is based on analysis models of the serpentine passage cooling circuits. To match the cycle flow, the HPT nozzle throat area was increased 1.7% relative to design intent. This was accomplished by re-staggering the nozzle 0.35 degrees more open. This is a very small angle difference and was rationalized that area measurement error and assembly tolerance which is estimated at approximately 2% is greater than this change. Correct work splits among the stages and the future mating with the rest of the turbofan engine analysis requires that the mass flow be consistent with the cycle. This was accomplished by adjusting the throat area in a reasonable way.

RESULTS

Each simulation has been run until the axial variation in flowrate accounting for cooling and leakage flows became less than 0.2%. Other parameters were also monitored to verify that the losses and work were not varying. Use of mass flow as an overall guide is appropriate for this subsonic turbine application. Because the multistage matching changes the mass flow, the mass flow for this application only settles out after other quantities have settled out. For each simulation, small changes in the simulation parameters have been made as the solution evolved. These included the nozzle re-stagger described above and a modification of coolant supply temperatures for the cooled turbine based on a re-evaluation of the assumptions. None of these cases was started from scratch and run to convergence without a simulation parameter change. The full turbine simulation took about 20,000 Runge-Kutta iterations with 50 iterations per flip or outer iteration. If the full turbine simulation was started from scratch with no changes in simulation parameters, it is expected that convergence could be achieved in about 10,000 iterations. The rig simulations take less time because of the reduced axial extent over which pressure and vortical waves need to travel.

Table I is a comparison of the rig analyses with experiment for one-dimensional overall quantities. The results compare well except that the flow is high in the HPT and low in the LPT relative to the experiment. It is not known why the HPT flow is high. but as mentioned above, a very small change in flow angle makes a big difference in flow. There can also be differences in actual throats relative to what was analyzed due to measurement and manufacturing tolerances. Coolant injection angles, especially at the trailing edge slots, also strongly affect the flowrate, but may not be modeled accurately. The LPT throats are not as difficult to measure as in the HPT since the exit angle is not as large. Therefore the geometry is probably not the cause of the discrepancy in the LPT. More likely, it may be due to the assumption in the turbulence model that the flow is fully turbulent, whereas in the rig there may be a large amount of laminar flow which would reduce the wakes and increase the flow. The temperature ratios do not match well, especially for the LPT. These values are also not consistent with the efficiency prediction which exhibits better agreement with the rig tests. As explained above, this is because the temperature measurements are made to obtain the profile shape, not the level, since the overall temperature levels are not rigorously calibrated in the experiments. A torque measurement is made to get the overall work from which efficiency is determined.

Table I. Comparison of Overall Performance of HPT and LPT Rig Analyses Relative to Experiment. Efficiency is analysis minus measured. Other quantities are (analysis - measured)/measured.

Case	Flow	Pressure Ratio	Temperature Ratio	Efficiency
HPT Rig (4 blade rows)	+2.5%	+0.4%	-1.6%	-1.0%
LPT Rig (14 blade rows)	-2.5%	+0.3%	-3.5%	-0.5%

Profiles of total pressure (PT), total temperature (TT) and angle are shown in Figures 7-9. Rig and engine analyses are compared with experimental data. At station 41, the PT and TT are normalized by the average PT and TT at station 4 (the inlet). At all other stations, PT and TT are normalized by the average plane 42 PT and TT values of the experiment or the cycle.

In Figure 7, the PT profiles at plane 42 show excellent agreement between the HPT rig analysis and data. The engine simulation profile is more hub-strong than the rig, while the LPT rig analysis profile is flat here since this plane represents the inlet of the LPT rig. At station 48, the strut loss and boundary layer in the LPT rig are well matched. At station 5, the shape and level match very well.

The TT profiles in Figure 8 at station 41 show the main difference between a rig and engine: namely the inlet combustor TT profile carries through nozzle 1 (although mixed) and has large gradients, especially near the hub relative to a flat inlet profile entering a rig. At station 42, relative to the experiment, the TT profile shows good agreement except near the hub where the experiment is slightly cooler than the prediction. The engine was instrumented with temperature rakes downstream of the HPT, and the full turbine simulation compares very well to these at station 48. At station 5, the full turbine comparison has the same overall gradient, but the midspan temperatures are calculated to be higher than the experiment. The LPT rig comparison of TT at station 5 shows good agreement. The overall difference is reflected in the 3.5% temperature ratio difference shown in Table I, which could be due to measurement calibration error.

The angle profiles are shown in Figure 9. At station 41, the full engine HPT nozzle 1 has been opened up to allow more flow and higher thrust since the rig was built. This is why the flow angle between full turbine and HPT rig are different. The swirl differences are not great between rig and full turbine at station 42. At station 48, the swirl at the LPT nozzle 1 leading edge in the full turbine simulation is different than design intent in the outer 20% span by as much as 10 degrees. At station 5, the LPT rig and measurement match well, and full turbine and LPT rig show little difference.

Figures 10 and 11 show the HPT and LPT rig static pressure comparison between analysis and experiment. The overall pressure drops are very large, so this same information has also been tabulated in Table II and Table III for the HPT rig and LPT rig respectively. The pressure taps in the rig are recessed in small gaps in the casing and mounted under the nozzle platform overlaps in the hub. This is why the location is described relative to the upstream or downstream

69

nozzle platform in the tables. In general, the comparisons are very good. The hub pressures compare less well than the casing pressures which is likely due to the location of the pressure taps within the cavities. These cavities are not modeled in the analysis. The inlet total pressure profile and the exit static pressure profile are specified which sets the overall total to static pressure ratio of the turbine. The inter-stage static pressure is therefore a result of the work splits among the stages and the reaction of each stage, which is a product of the turbine simulation. The good pressure comparison demonstrates that both work splits among the stages and reaction are correctly simulated.

Table II. Comparison of HPT Rig Hub and Casing Static Pressure. Quantities represent (analysis - measured)/(HPT rig overall total pressure drop).

HPT Rig Location	Casing	Hub
Stage 1 HPN Downstream Platform	0.63%	1.86%
Stage 2 HPN Upstream Platform	No Data	-1.30%
Stage 2 HPN Downstream Platform	0.30%	0.87%
Strut Forward Platform	-1.34%	-0.91%
Strut LE Rake Plane	0.60%	0.12%

Table III. Comparison of LPT Rig Hub and Casing Static Pressure. Quantities represent (analysis - measured)/(LPT rig overall total pressure drop).

LPT Rig Location	Case	Hub
Nozzle 1 Downstream Platform	-0.04%	0.41%
Nozzle 2 Upstream Platform	-1.42%	0.76%
Nozzle 3 Downstream Platform	No Data	-2.43%
Nozzle 4 Downstream Platform	0.47%	-0.18%
Nozzle 5 Upstream Platform	-0.50%	0.37%
Nozzle 5 Downstream Platform	-0.60%	No Data
Nozzle 6 Upstream Platform	-1.39%	No Data
Nozzle 6 Downstream Platform	-0.31%	-1.43%
Outlet GV Upstream Platform	-0.24%	-0.22%

These three configurations represent the three-dimensional flowfields of 36 blade rows. These are complex flowfields with variable properties, cooling flows and large secondary flows. There are many interesting features. One of these is visualized in Figure 12, which shows streamlines that were launched in the purge flow just upstream of LPT rotor 1. In the engine configuration, the amount of purge flow entering here is quite large relative to the rig. The streamlines get caught up in the hub vortex and lift off the hub surface. Downstream of the rotor is a contour plot of total temperature showing that the cold fluid emanated from the purge cavity.

Multistage Effects

Many axisymmetric solvers used in quasi-3D turbomachinery design systems use a blockage factor or flow coefficient as a sole parameter to account for many effects not described by the axisymmetric equations. One of these effects is due to circumferential variations within the flowfield. This approach of using blockage has a basis in matching measurements given total pressure, total temperature, angles, static pressure and overall flow rate. The only way to match the flow rate is by introducing a blockage factor which is less than one. For a given definition of average quantities, such as mass averaged enthalpy, area averaged static pressure, enthalpy averaged total pressure, mass averaged angular momentum and a momentum averaged meridional angle, one can determine this blockage factor from post processing any 3D solution. Because of the definition, this blockage is due to any circumferential variations including wakes, tip clearance flows, secondary flows, leakage flows and potential effects.

The blockage calculated in this way for the full turbine configuration is shown in Figure 13. The circumferential variations are especially large in the HPT where the temperature varies by over one thousand degrees Rankine due to cooling flow wakes and the secondary flows which act on the large inlet radial temperature gradients. In addition, the total pressure and static pressure vary tremendously. Values of this blockage factor less than 0.8 exist over large regions of the HPT. This means over 20% of the flow area is "blocked" in these regions due to these circumferential variations. These effects must be adequately modeled or the static pressure comparisons shown in Figures 10 and 11 and Tables II and III would not be so good. In addition to work splits and reaction, the thrust balance of the engine can be better simulated. Adamczyk (1999) has described flow blockage as being related to the recovery energy thickness and then related this to the unsteady deterministic flow state. This unsteady deterministic flow state is modeled well using the average passage approach and allows these effects to be captured. This is not the case for a mixing plane approach where the circumferential variations are eliminated across the mixing plane.

Other flow features become apparent in Figure 13 and this type of plot can demonstrate some overall characteristics of the simulation with one axisymmetric plot. Some of these features are the tip clearance flows downstream of the HPT rotors. The hub leakage effects can also be seen in the HPT and LPT.

Another multistage effect is that the static pressure downstream of a nozzle is very different with and without the rotor behind it. This is due to the blade blockage and turning of the downstream rotor and the high exit angle of the nozzle. Figure 14a shows the static pressure field predicted from an isolated blade row solver. The average exit radial static pressure profile has been imposed which comes from a streamline curvature axisymmetric solver. The boundary condition of this code holds this imposed average static pressure while allowing variations in the circumferential direction. Due to the high exit angle of the nozzle, the circumferential variations persist far downstream. Figure 14b shows the corresponding plot from an average passage solution. Notice how the isobars are altered by the close proximity of the rotor. The circumferential variations are attenuated by the rotor modeled as body forces. These apply the correct turning, energy drop and blade blockage to simulate the rotor downstream of the nozzle.

70

PARALLEL COMPUTING CAPABILITY

As mentioned above in the description of the solver, the code has two levels of parallel capability as shown in Figure 1. Achieving good parallel performance with this code requires that it be load balanced. Figure 15 shows how this has been done with the full turbine 18 blade row simulation. The size, geometry and aerodynamics of each blade row is different, and therefore the grid size varied. The load balancing was accomplished by assigning a blade row a fraction of processors equal to the fraction of grid relative to the total number of grid points. As shown in Figure 15, this leads to an imperfect load balancing because the number of processors is integral. The load balance improved slightly by increasing the number of processors from 60 to 121.

Figure 16 shows the parallel efficiency for APNASA run on an SGI ORIGIN 2000. The parallel performance of an isolated blade row calculation up to 8 processors is shown and demonstrates excellent parallel efficiency. With 2 processors, the speed-up is actually super linear, possibly due to reduced cache memory misses. The real test of the parallel performance is with the real full turbine simulation. The speedup is plotted against the number of processors assigned to blade row 2. A case with an equal number of processors per blade row is also shown and demonstrates the importance of optimal load balancing. Also shown are the 60 and 121 processor calculations which used 4 and 8 processors on blade row 2, respectively. The resulting parallel efficiency is 87.3% using 121 processors which truly demonstrates the case is well load balanced and the code has excellent parallel capability.

Currently the code takes 7.3×10^{-5} sec/grid-point/iteration on the 250 MHz SGI ORIGIN 2000 running in parallel with 121 processors. Since a solution starting from scratch would take approximately 10,000 iterations, a solution of the full turbine which has a total of nine million grid points would take 1820 processor hours. However, due to the parallel capability, this solution would be done in 15 hours of wall clock time utilizing 121 processors. This could be accomplished overnight, the key criteria for a code to be useful in the design environment.

The scenario for design use is that a design case can be run overnight. Automatic post-processing scripts could then be run at the end of the component simulation. The designer can then evaluate the design in the morning, make modifications, re-grid the new geometry and submit a new job to be run overnight. This process would continue until an optimal design is produced.

SUMMARY

Three GE90 turbine configurations have been analyzed using the average passage approach. Two of these are rig configurations where detailed data exists. The third is a full turbine configuration for the GE90 at a takeoff configuration. This simulation is the first dual-spool cooled turbine analyzed with a 3D multistage solver. Comparisons have been made to the measurements, and good agreement has been demonstrated. Multistage and component interaction effects have also been presented which demonstrate why a calculation such as this is worthwhile. The parallel efficiency of the code is excellent and can lead to effective use of this code in the design environment.

REFERENCES

Adamczyk, J.J., Mulac, R.A., and Celestina, M.L., 1986, "A Model for Closing the Inviscid Form of the Average-Passage Equation System," Journal of Turbomachinery, Vol. 108, pp. 180-186.

Adamczyk, J.J., 1999, "Aerodynamic Analysis of Multistage Turbomachinery Flows in Support of Aerodynamic Design," To be published at the 1999 ASME IGTI Conference.

Chen, J.P., Celestina, M.L. and Adamczyk, J.J., 1994, "A New Procedure for Simulating Unsteady Flows Through Turbomachinery Blade Passages," ASME Paper 94-GT-151.

Dawes, W.N., 1990, "Towards Improved Throughflow Capability: The Use of 3D Viscous Flow Solvers in a Multistage Environment," ASME Paper 90-GT-18.

Fritsch, G. and Giles, M.B., 1993, "An Asymptotic Analysis of Mixing Loss," ASME Paper 93-GT-345.

Hunter, S.D., 1998, "Source Term Modeling of Endwall Cavity Flow Effects on Gaspath Aerodynamics in an Axial Flow Turbine", Ph.D. Thesis, University of Cincinnati, Department of Aerospace Engineering and Engineering Mechanics, November.

Jameson, A. and Baker, T.J., 1984, "Multigrid Solutions of the Euler Equations for Aircraft Configurations," AIAA Paper 84-0093.

Kirtley, K.R., Turner, M.G. and Saeidi, S., 1999, "An Average Passage Closure Model for General Meshes," To be published at the 1999 ASME IGTI Conference.

Shabbir, A., Celestina, M.L., Adamczyk, J.J. and Strazisar, A.J., 1997, "The Effect of Hub Leakage Flow on Two High Speed Axial Flow Compressor Rotors," ASME Paper 97-GT-346, June.

Turner, M.G., 1996, "Multistage Turbine Simulations with Vortex-Blade Interaction," Journal of Turbomachinery, Vol. 118, pp. 643-653.

Turner, M.G., and Jennions, I.K., 1993, "An Investigation of Turbulence Modelling in Transonic Fans Including a Novel Implementation of an Implicit k-e Turbulence Model," ASME J. of Turbomachinery, Vol. 115. No. 2, April 1993, pp. 249-260.
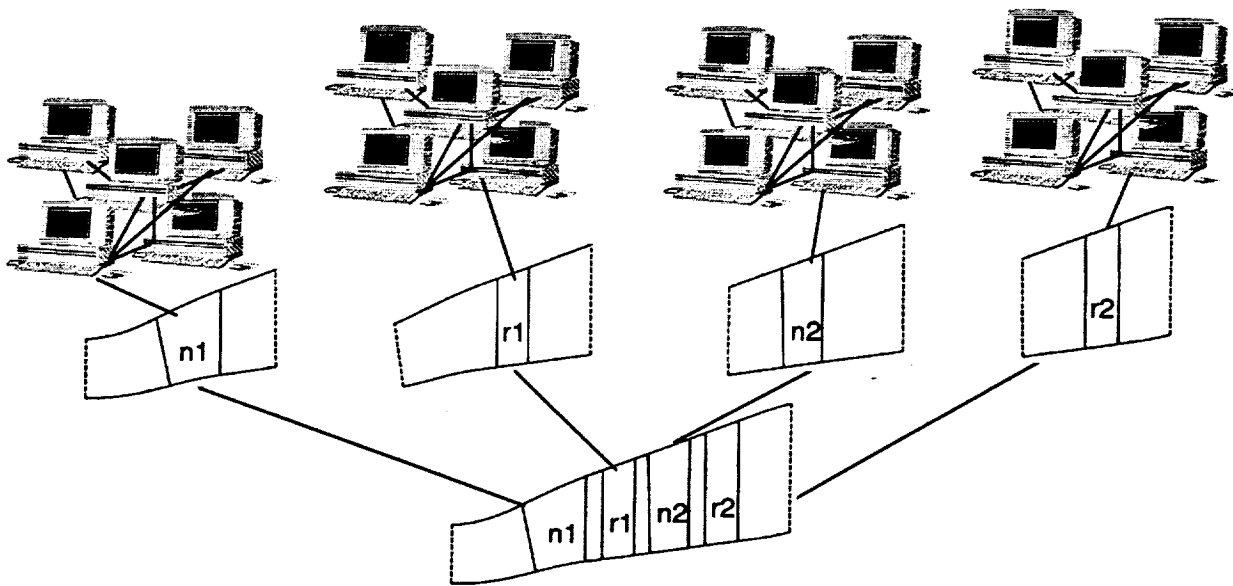
Figure 1. Two levels of parallel capability in Average Passage Code.

Leading edge detail
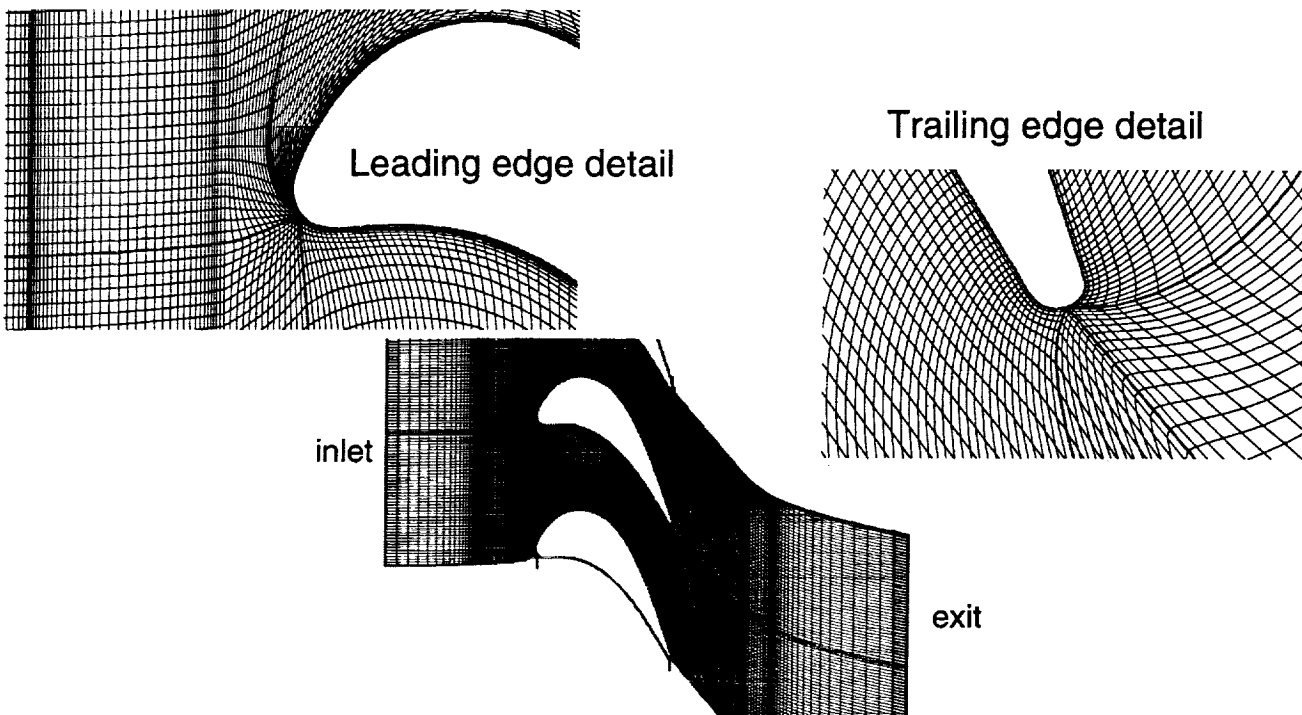
Trailing edge detail

inlet

exit

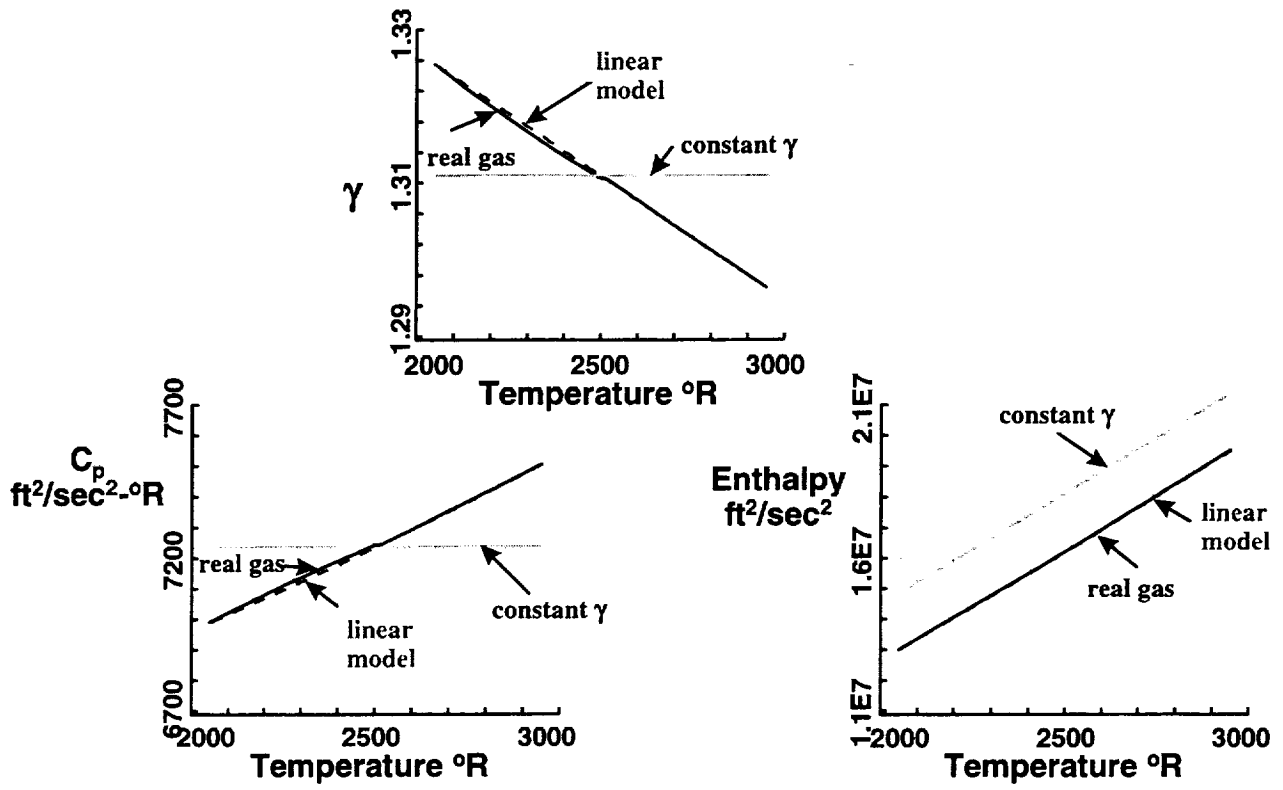**Figure 2. Blade-to-blade grid for the GE90 HPT rotor1.**

Figure 3. Linear real gas model used in Average Passage Code at HPT temperatures.
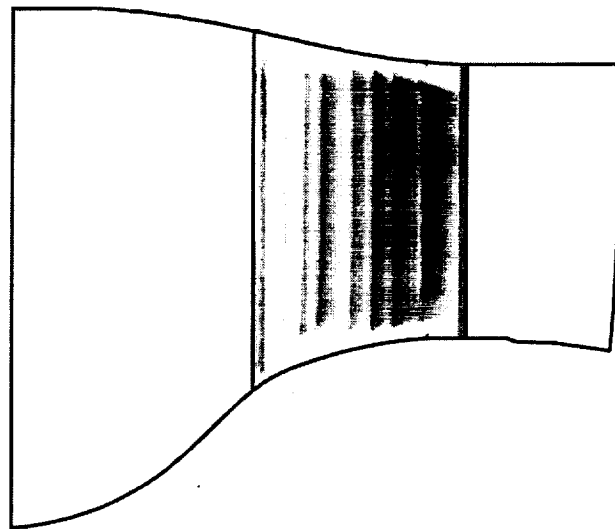

Figure 4. Total temperature contours of pressure side surface of nozzle 1 showing effect of the rows of film cooling holes. Dark - cold, light - hot.
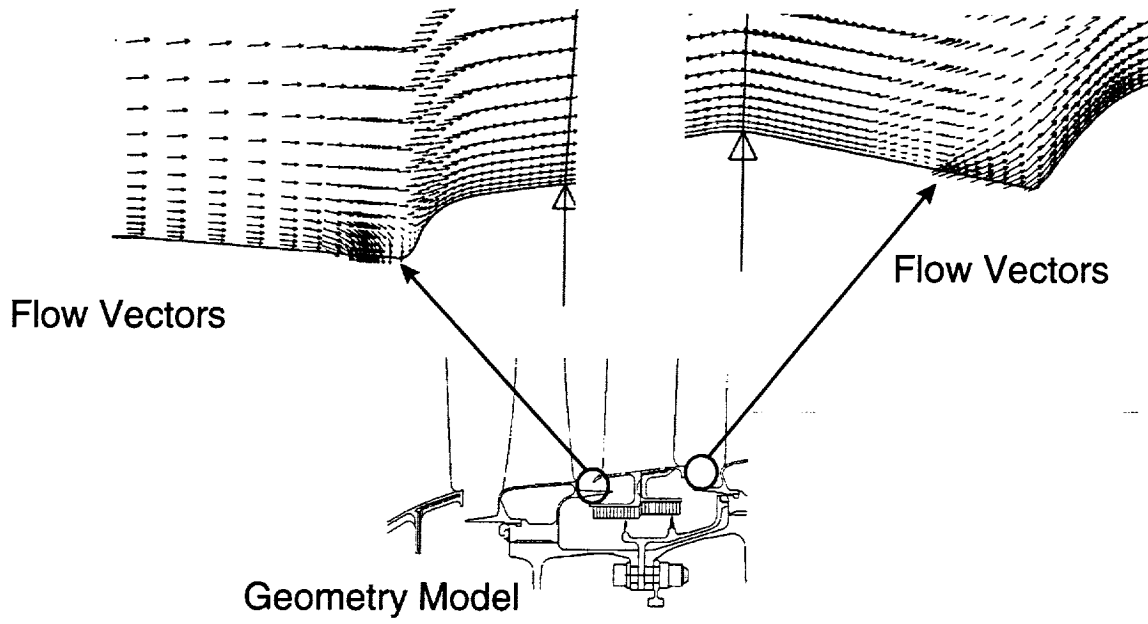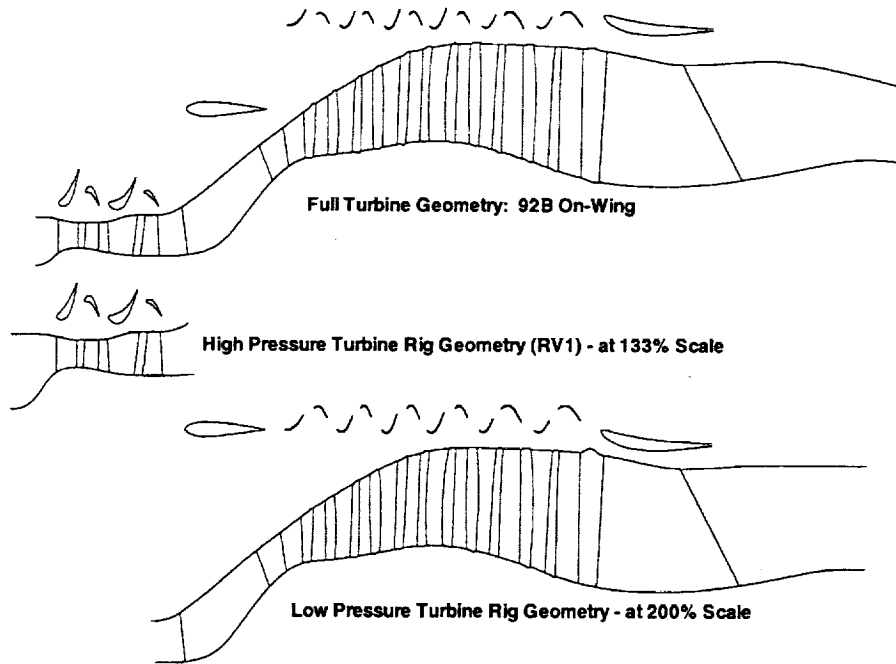
Flow Vectors

Flow Vectors

Geometry Model

Figure 5. Application of leakage model.

Full Turbine Geometry: 92B On-Wing

High Pressure Turbine Rig Geometry (RV1) - at 133% Scale

Low Pressure Turbine Rig Geometry - at 200% Scale

Figure 6. Geometry for full turbine, HPT rig and LPT rig.
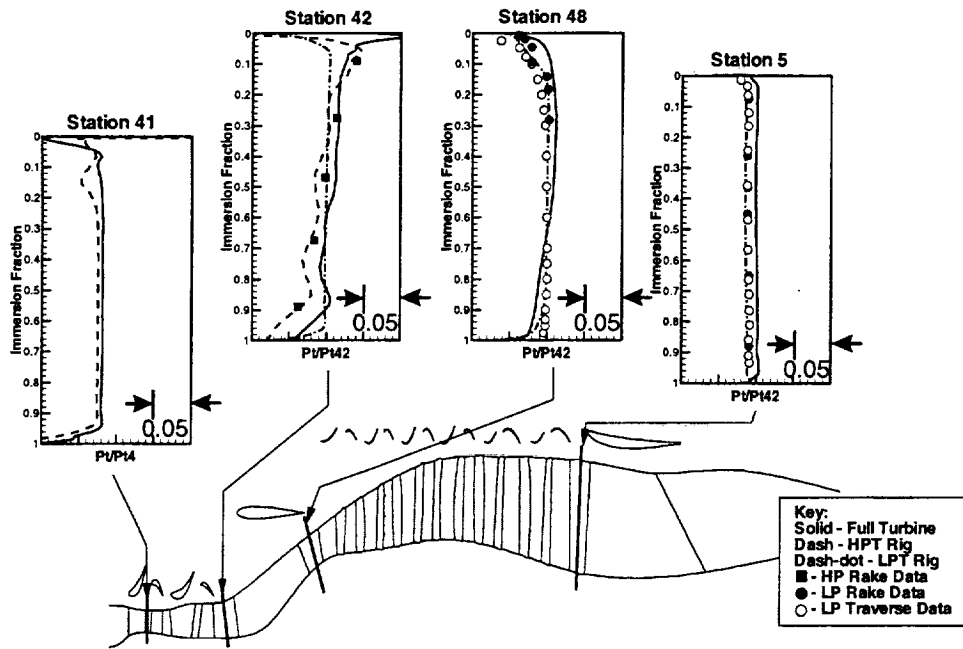
Figure 7. Total pressure profiles in turbine. Each major division is 5%.
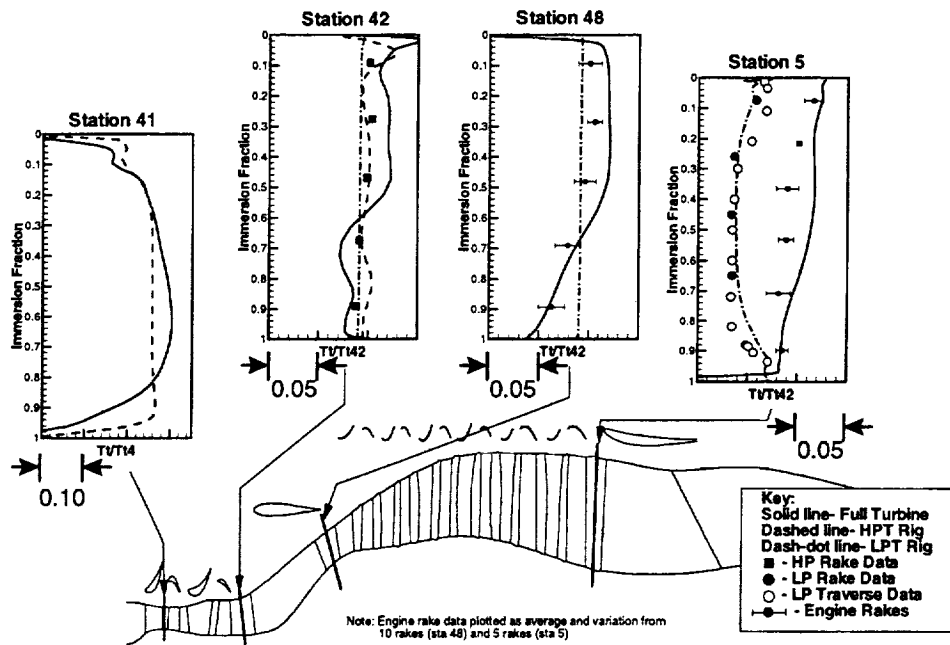
Figure 8. Total temperature profiles in turbine. The major division at station 41 is 10%. The major division for stations 42, 48 and 5 is 5%.

75
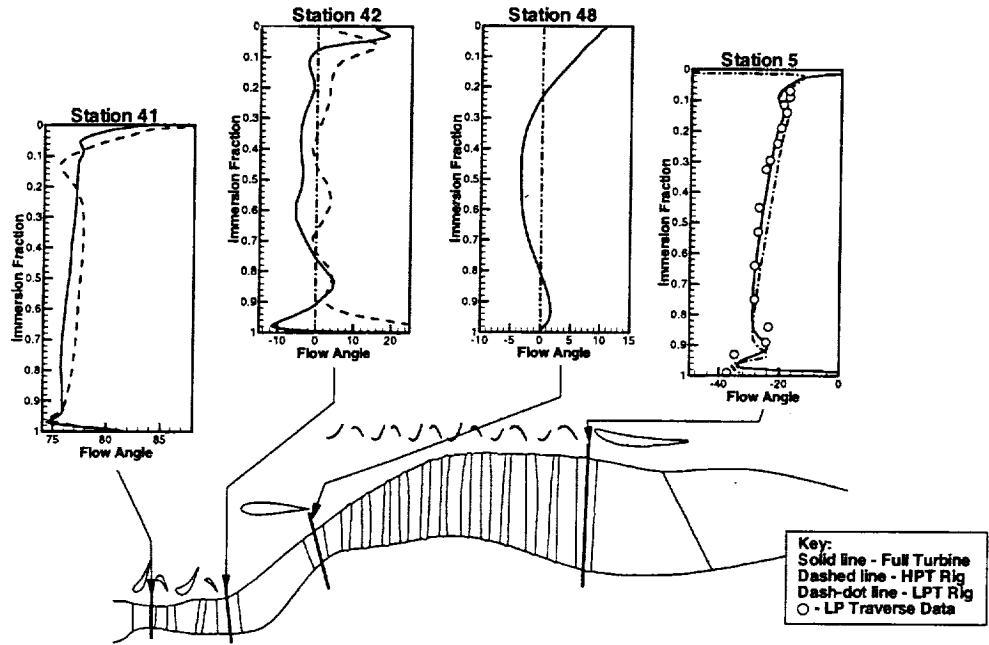
Figure 9. Absolute flow angle profiles in turbine.
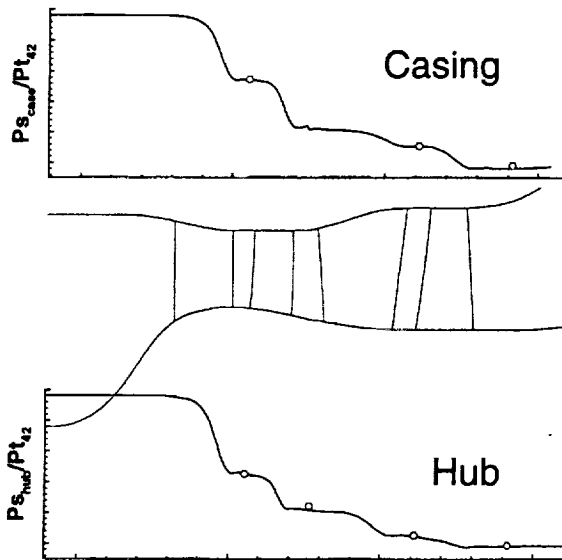
Figure 10. HPT Rig static pressure. Line - analysis, circle - data.
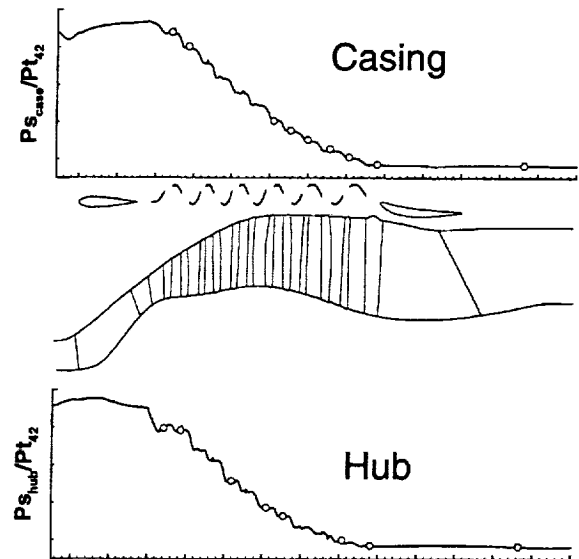
Figure 11. LPT Rig static pressure. Line - analysis, circle - data.
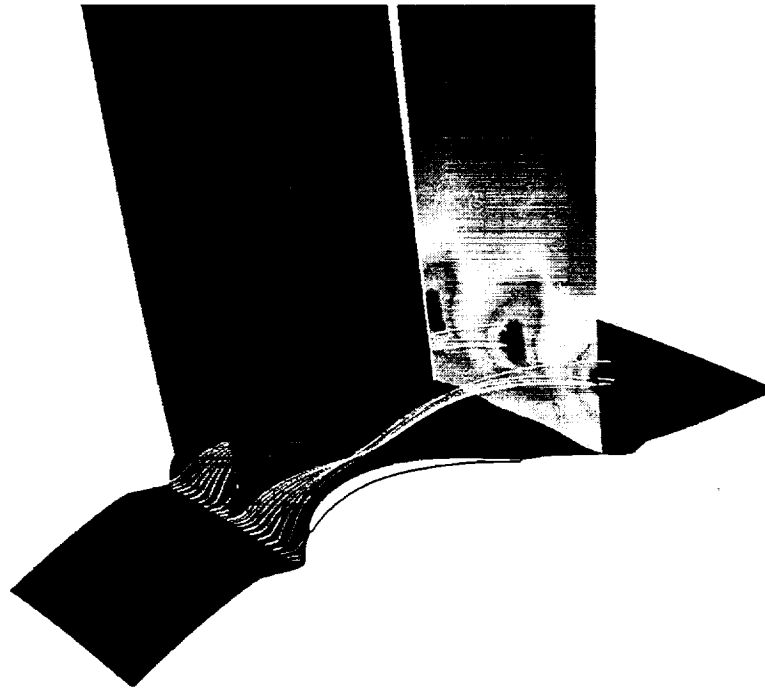
Figure 12. Streamlines showing purge flow caught in hub vortex. Plane downstream of trailing edge shows total temperature contours (dark-cold, light-hot). Full turbine simulation, LPT rotor 1.

Blockage: 0.75   0.80   0.85   0.90   0.95   1.00
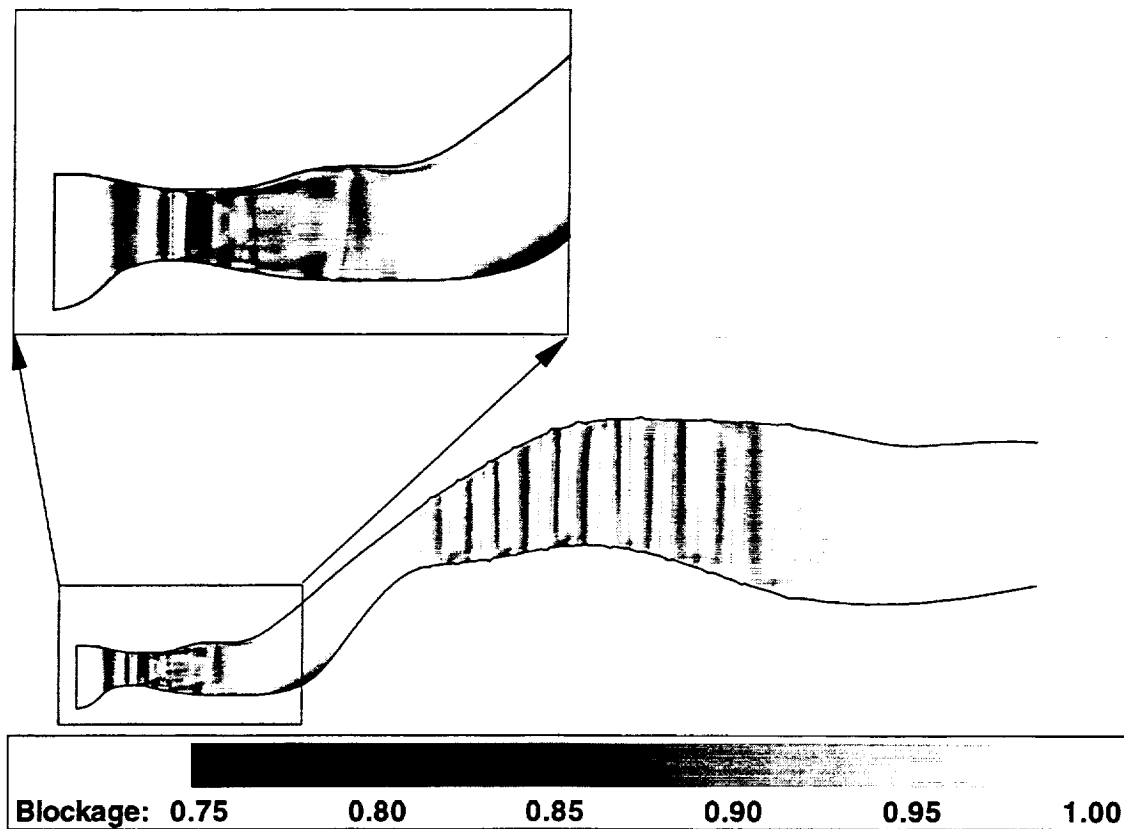
Figure 13. Contours of axisymmetric blockage for the full turbine configuration.

b.) APNASA Results

a.) Isolated Blade Row Results
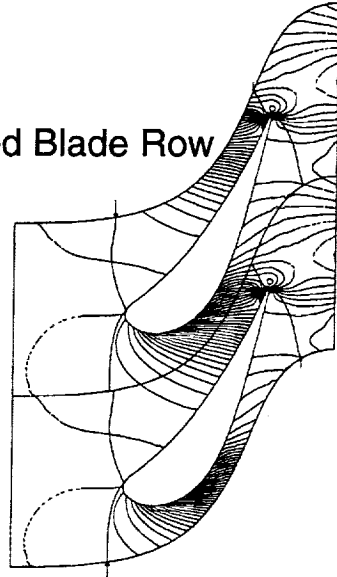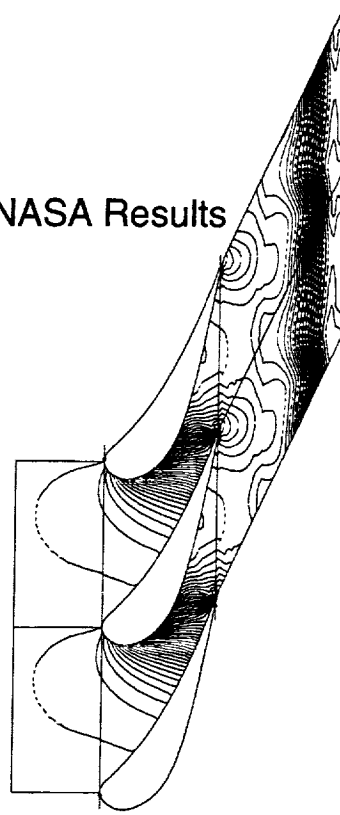
Figure 14. Static pressure contours for GE90 HPT nozzle 1 showing multistage effects.
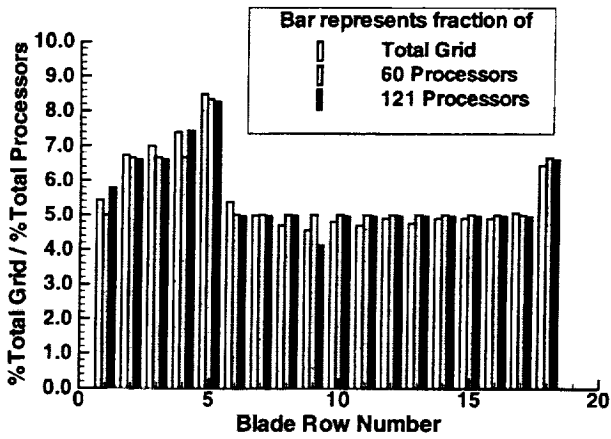

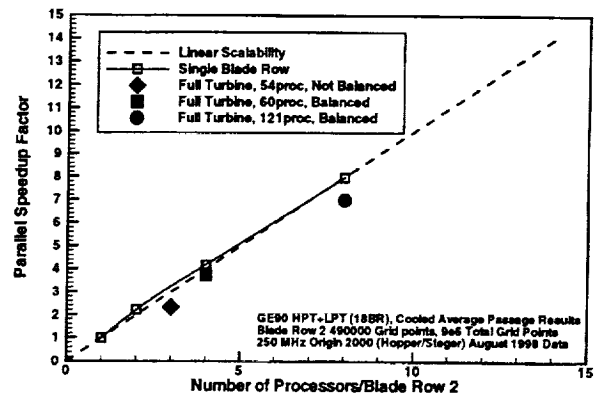**Figure 15. Load balancing based on grid size.**

Figure 16. Parallel efficiency.

Appendix E

Excerpts from the 1999 IGTI scholar lecture paper by John J. Adamczyk

"Aerodynamic Analysis of Multistage Turbomachinery Flows in Support of Aerodynamic Design"

sor stalls at a flow coefficient near the peak pressure point of the characteristic.

Figure (11) shows the measured static pressure rise characteristic for each stage along with results from the simulations. The agreement between the simulation results and the data is very good. For the flow coefficient of 0.395, Fig. (12) shows plots of the total and static pressure coefficient, the axial and absolute tangential velocity, and the absolute and relative flow angle as a function of span for the simulation and the experiment. The plots are for an axial location behind the second stator. Once again, the agreement between the simulation results and the data is good. The slight difference between the static pressure coefficient derived from the simulation and that measured inboard of 40% span is unknown. For the same flow coefficient, Fig. (13) compares the simulated and measured results for an axial location behind the third stage rotor. The agreement between the simulation results and that derived from the measurements is comparable to that shown in Fig. (12). Additional comparisons are presented in Adamczyk, *et al.* (1998).

These results clearly show that the APNASA code with its current models that account for the effects of the unsteady deterministic flow field is, to a large extent, capturing the flow features which are setting the performance of the LSAC compressor.

High Speed Ten Stage Compressor

The next set of results are for the high pressure (H.P.) compressor of the GE 90 engine series. This compressor has ten stages plus an IGV. At the design point the first three stages of this compressor are transonic. The origin of this compressor dates back to the GE E^3 compressor, Wisler, (1977). In simulating this compressor, all known leakage and bleed flows were accounted for. The first set of results, Fig. (14), shows the total temperature and total pressure at the exit of each rotor as predicted by APNASA relative to that predicted by a refined quasi-three-dimensional flow code, CAFMIX II, developed by Smith (1999). The results are presented in terms of a relative difference between the APNASA predictions and those of CAFMIX II. The leakage and bleed flows are the same in both simulations. The simulated operating point of the compressor is near its design point. Figure (14) shows that the results from both models are in good agreement with each other throughout the compressor. The maximum difference in total temperature is less than .8%, and the difference in total pressure is less than 4%. Figure (15) shows spanwise profiles of the normalized total pressure distribution and the normalized total temperature distribution at three axial locations within the compressor. The locations are the exit of the third and seventh stage and at the compressor discharge. Once again the agreement between the two mod-

els is quite good. The average-passage model appears to give results which are very comparable to those of a refined quasi-three-dimensional flow model without the empiricism built into the quasi-three-dimensional model.

An interesting outcome of this study is a comparison between the flow blockage estimates of CAFMIX II and those deduced from the APNASA simulation. Turner (1999). The flow blockage deduced from the APNASA simulation is based on the definition of flow blockage used in the CAFMIX II code. The comparison is shown in Fig. (16). Even though the through-flow results from both codes are nearly the same, the flow blockage estimates are markedly different. For example, for the fifth stage the flow blockage estimate of CAFMIX II is a factor of two times larger than that deduced from the APNASA simulation. In addition, the flow blockage deduced from the APNASA simulation is almost constant throughout the compressor, while the estimate from CAFMIX II increases from the front to the discharge of the compressor. The CAFMIX II flow blockage estimate at the exit of the tenth stage rotor is more than twice that at the exit of the first stage rotor.

Since the predicted total temperature and total pressure rise through the compressor by both simulations was nearly the same, one may wonder if the difference in estimated flow blockage is being compensated for by differences in estimates of the flow angle exiting the blade rows. Figure (17) shows the spanwise distribution of the flow angle exiting the third stage rotor, the third stage stator, the sixth stage rotor, and the sixth stage stator as predicted by both codes. The agreement between the two predictions is good, but there are differences. The sensitivity of total pressure rise or total temperature rise to changes in flow blockage or exit flow angle for this compressor is unknown to the author. Whether the difference in the predicted exit flows seen in Fig. (17) compensates for the difference in estimated flow blockage seen in Fig. (16) is unknown.

The results presented in Figs. (16) and (17) raise questions as to how best to incorporate the results from a three-dimensional simulation into a through-flow model. If the estimates of flow blockage derived from the APNASA simulation were introduced into CAFMIX II, it is speculated that the outcome would be an increase in the pressure rise across the aft stages, and a decrease in the pressure rise across the front stages for a fixed overall compressor pressure ratio. This would drive the agreement between the two models apart.

Unfortunately the compressor was never tested at the IGV setting, vane settings, and bleed rates corresponding to the APNASA and CAFMIX II simulations. Therefore, no true prediction of the compressor performance is available by which to judge either code. A series of simulations were executed using APNASA with the IGV and vanes set

to their test settings in an attempt to match experimental measurements at a point on the operating line near design wheel speed. Additional simulations were executed at this wheel speed in which the compressor was throttled from the operation line to near stall. The first set of results. Fig. (18) shows the relative difference in total pressure between the simulation result and the data at each stage in the compressor. The data was obtained from instrumentation mounted to the leading edge of the stators. The axial location of the simulation results is also the leading edge of stators and the compressor discharge. The agreement between the simulation results and the data is quite good. Figure (19) shows the spanwise distribution of normalized total pressure and total temperature at the leading edge of the third stage stator, the leading edge of the seventh stage stator and at the discharge of the compressor. Both simulation results and data are shown. The profiles resulting from the simulation are in good agreement with that inferred from the data, especially the total temperature profiles. The compressor efficiency as estimated by the simulation agreed very well with the measured efficiency.

The level of agreement shown in Figs. (18) and (19) required an adjustment of the bleed rates from the initial values specified. The initial values were best estimates prior to compressor tests. The final estimates were derived from measurements and a series of data match computations. Figure (20) shows the relative difference in total pressure at each stage based on the simulation used to generate the results in Fig. (18) and (19) (i.e., best estimate of bleed rates, IGV and vane settings) and two other bleed rate schedules. The first of these bleed rate schedules. annotated by shaded bars, corresponds to that used to generate the results in Figs. (14) through (17). For this bleed schedule the front end of the compressor becomes unloaded relative to the back end. The next result, annotated by open bars, was generated by lowering the third stage bleed rate to that measured. By drawing less third stage bleed air the predicted pressure ratio of the front stages increased to near their measured values, while that of the back stages was reduced. Finally, reducing the amount of bleed air being drawn from the seventh stage bleed to that measured lowered the predicted pressure ratio of stages eight through ten to near that measured. Stages one through four remained unchanged as stage seven bleed was reduced, while stages five through seven experienced an increase in pressure ratio. The results shown in Fig. (20) are quite significant for they clearly show how bleed can affect the matching of stages within a compressor. The initial simulation using the *a priori* estimates of bleed rates was judged to be less than satisfactory for design purposes. Clearly. in addition to having sound models to account for the unsteady flow field within axial flow multistage compressors, it is equally important to have credible estimates of the leakage flow rates and the bleed flow rates.

A series of simulations were also performed to ascertain APNASA's ability to compute the impact of throttling on compressor performance. The wheel speed for these simulations corresponds to that used in the previous simulations. Figure (21) shows the percent difference in total pressure ratio of individual stages relative to their predicted total pressure ratio at the operating line (i.e., simulation results used to generate the results in Fig. (18)). The pressure ratio being defined from stator leading edge to rotor trailing edge. For the tenth stage the pressure ratio is from the leading edge of the ninth stage stator to compressor discharge.

A series of simulations were executed for increasing back pressure until the code failed to converge. The highest total pressure ratio for which a converged solution was obtained is less than the total pressure ratio at which the compressor stalled. The first case labeled Case 1 is for a back pressure slightly greater than the value corresponding to Fig. (18), while Case 4 is for a back pressure setting very close to the numerical stall point. The other two cases are for back pressure settings which lay between these two extremes.

For Case 1, the slight increase in back pressure caused the last six stages to move slightly up their pressure characteristic. The operating point of the first four stages remains unchanged. Case 2 increased the back pressure further and caused all of the stages with the exception of stage 1 to respond. The mass flow, being set by the first stage, is unaffected by this increase in back pressure. The change in the pressure ratio of stages five through nine is significantly greater than that for stage ten. Stage ten show a modest change in pressure ratio which implies that it is operating on the flat part of its characteristic. Raising the back pressure still higher, Case 3, further increases the pressure ratio of stages three through nine. Stages one and two remain unchanged as does the mass flow, while the pressure ratio across stage 10 decreases. Stage ten is operating on the positive side of its pressure characteristic. Throttling the compressor to near its numerical stall point, Case 4, causes an increase in pressure ratio of stages two through eight. The pressure ratio for stage one remains unchanged as does the mass flow. The pressure ratio for stages nine and ten has decreased. Both nine and ten are now operating on the positive side of their characteristic. The decrease in stage ten's pressure ratio from its previous value is quite noticeable. It appears that the pressure characteristic for stage ten rolls over very abruptly after peak pressure. Obtaining a converged solution at still higher back pressures proved difficult because of the extreme sensitivity to back pressure setting. It is thought that stage eight is operating near peak pressure and that any slight increase in back

pressure causes its operating point to shift to the positive side of its pressure characteristic. When this occurs, the compressor numerically stalls. At this wheel speed, there is experimental evidence which suggests that stall originates in the eighth stage, Liou (1999).

High Speed Three Stage Compressor

The next set of results are for a small high-speed three stage plus IGV axial flow compressor. The compressor was designed, tested and simulated by Allied Signal, Mansour (1999). The compressor is of a modern design, employing transonic rotors in all three stages. Although the simulations are not a prediction (the tests predate the simulations) they were executed by a researcher who is not a developer of APNASA but rather a user who is attempting to assess its predictive capabilities. The total pressure characteristics and the total temperature characteristics of the individual stages as derived from the simulations and measurements are shown in Fig. (22). The experimental results were obtained from stator leading edge instrumentation. For the first stage, the total pressure ratio as well as the total temperature ratio is from the inlet to the exit of the first stage rotor. For stage two, the pressure ratio as well as the total temperature ratio is from the inlet of the first stage stator to the exit of the second stage rotor. For the third stage, the total pressure ratio as well as the total temperature ratio is from the inlet of the second stage stator to the exit of the third stage rotor. The stage total pressure ratios as well as the stage total temperature ratios are plotted as a function of corrected flow exiting each of the rotors. The characteristics are for the design wheel speed. The error between the simulated results and experimental data is also shown on the figure.

Two throttle settings were simulated in an attempt to bracket the design pressure ratio of the compressor. In both the simulation and test, the first stage operating point remains fixed as the compressor is throttled. This result implies that the second stage rotor is choked. The corrected mass flows exiting the first stage rotor, as derived from the simulations are approximately 1.5% greater than that deduced from the experimental measurements. For the second stage, the difference in corrected mass flow is 1.4%. For the third stage, the difference between the corrected mass flow deduced from the data and that from the simulation results is .4%. Overall the agreement is quite satisfactory.

Figure (23) shows the total pressure ratio and the total temperature ratio at the exit of the first stage rotor as a function of span. Percent differences are also shown on the figure. Only the results from one simulation and one experimental point are shown since the operating point of the first stage rotor remained unchanged as the compressor was throttled. With the exception of the region near 90% of span, the agreement between the total pressure pro-

files derived from the simulation and the experiment data is very good. At 90% of span, the total pressure profiles differ by less than 3%. The total temperature profiles are also in good agreement. The difference between the two total temperature profiles at midspan is less than 1.0%. It is encouraging to see that the simulation shows nearly the same rise in total temperature as the experiment outboard of 70% of span.

Figure (24) shows the pressure ratio and the total temperature ratio at the exit of the third stage rotor as a function of span. The pressure ratio associated with the two simulations brackets the experimental pressure ratio. The shape of the total pressure profiles are in reasonable agreement with each other. At midspan, the two simulations differ by less than 5%, while the experimental value differs from either simulation result by less than 3%.

The shape of the total temperature profiles shown in Fig. (24) are also in reasonable agreement with each other. However, the spanwise average total temperature from the two simulations is less than that deduced from the experiment. The relative difference between the experiment and simulation point 1 is approximately 1.3%.

The agreement between data and simulation was judged to be sufficient for the purposes of using APNASA to guide the aerodynamic design of this multistage axial flow compressor, Mansour (1999).

High Speed High Pressure and Low Pressure Turbine

The final simulation examples are of a high pressure turbine (HPT) and low pressure turbine (LPT). The HPT is a 3/4 scale model of the HPT from the GE engine family, while the LPT is a 1/2 scale model of the LPT from the GE engine family. The HPT is a two stage machine while the LPT is a six stage machine. The simulations of both machines included the effect of cooling and purge flows as well as variable gas properties. The simulations were set up to match the conditions for which data was available. The details of the simulations are given in Turner, et al. (1999). Figure (25) shows the spanwise profiles of total pressure and total temperature exiting the second stage rotor of the HPT. The measurements are represented by solid squares, while the simulation results appear as a solid line. The relative difference between the measurements and the simulation results is also shown on the figure. The agreement between the simulation and the data is very good. A comparison of the overall one-dimensional performance parameters showed that the simulation was 2.5% high in mass flow, 0.4% high in total pressure ratio and 1.6% low in total temperature ratio. Figure (26) shows a similar set of plots for the LPT. The spanwise profiles are at the exit of the sixth stage rotor. The relative difference between the measurements and the simulation is shown on the figure. The

agreement between the two is also very good. For the LPT study, a comparison of the overall one-dimensional performance parameters showed that the simulation was 2.5% low in mass flow, 0.3% high in total pressure ratio, and 3.5% low in total temperature ratio.

The machines whose simulation results were presented in this section cover a broad range of multistage axial flow turbomachinery configurations. The objective of this section was to illustrate to the turbomachinery design community what could be, and what could not be, predicted by a code based on the average-passage flow model with the current procedures to account for the effects of the unsteady flow environment within multistage turbomachines. All the simulations were executed without recourse to information supplied by external models or data which prescribed the aerodynamic matching of stages, this information being an output of the simulations and not an input. Being able to reliably establish the aerodynamic matching of stages in a multistage configuration is critical to ensuring that advanced designs attain their aerodynamic goals in the first build.

In the next section the current state of the art for simulating multistage axial flow turbomachines in support of aerodynamic design using models which are uncoupled from through-flow models is summarized. Suggestions for future work are also presented.

Summary and Suggested Future Work

Before summarizing it is important to stress the need to have correct geometry and correct inflow and outflow boundary conditions before attempting any simulation. This detail cannot be emphasized enough as evidenced by the findings of Shabbir, *et al.* (1997), Escuret and Veysseyre, (1997), Wellborn, *et al.* (1999). It is important to know the geometry at the flow conditions being simulated. This includes the blade geometry as well as the hub and shroud geometry. Rotor tip clearance, stator hub clearance, variable geometry setting, and variable geometry button configuration must all be known. Blade fillet geometry and surface finish must also be known. All cavities which are opened to the primary flow path must be known. All leakage flows must be known including those associated with shrouded blading, bleed flows, purge flows and the cooling flows of cooled turbines. If any of these details (geometry, inflow and outflow boundary conditions) are unknown, it is important to establish the sensitivity of the simulation results to their assumed values.

Table I is a bullet chart which summarizes the fluid mechanics addressed in this paper. At the top of the list is spanwise transport of wake fluid particles which leads to a redistribution of total temperature, and momentum. Although not specifically addressed, the spanwise redistribu-

tion of entropy is also implied.

Next on the list is circumferential transport of wake fluid particles which also leads to a redistribution of total temperature and momentum. The flow physics associated with this redistribution was shown to be equivalent to that associated with spanwise redistribution of total temperature. Although circumferential redistribution of total temperature does not appear to impact aerodynamic performance, it does lead to total temperature segregation resulting in the formation of hot spots. These hot spots have a significant impact on turbine blade life.

TABLE I
Summary of Unsteady Deterministic Flow Processes Discussed Which Impact The Time-Average Performance of Multistage Turbomachinery
● Spanwise transport of wake fluid particles.
● Circumferential transport of wake fluid particles.
● The straining of wakes.

Circumferential redistribution of momentum also involves the interaction between a blade and incoming wakes and blade boundary layers. The impact of incoming wakes interacting with turbulent blade boundary layers on aerodynamic performance is not clear. There appears to be an indication that the interaction of compressor rotor tip clearance flows with a downstream stator leads to increased loss. However, when the interaction involves a transitional blade boundary layer, evidence exists that aerodynamic performance is impacted. This subject will be addressed later in this section.

Next on the chart is the straining of wakes as they convect through a blade row. This straining process leads to wake recovery. Wake recovery results in the transfer of energy by a reversible flow process between the unsteady flow generated by wakes and the time average flow field. Wake recovery was shown to impact the mixing loss of wakes as they pass through a downstream blade row. With respect to an axial flow compressor, the mixing loss attributed to 2D wakes is significantly reduced by the wake recovery process. For an axial flow turbine, the mixing loss attributed to 2D wakes is increased by the wake recovery process. Thus, there is a performance benefit to be gained in axial flow compressors by having blade rows closely spaced, while the opposite is true for axial flow turbines.

It was shown that the wake recovery process also impacted the pressure rise across the blade row through which the wakes are passing. The pressure rise was linked to flow blockage defined in terms of an energy recovery thickness.
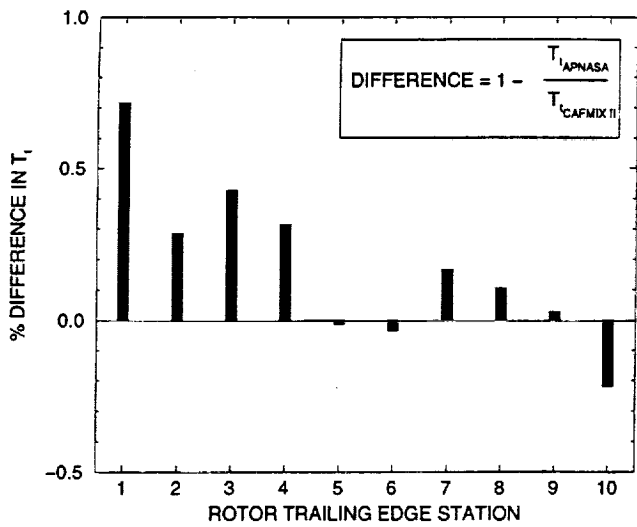
Fig. 14a. Comparison of total temperature as predicted by APNASA and CAFMIX II for the 10-stage GE90 compressor.
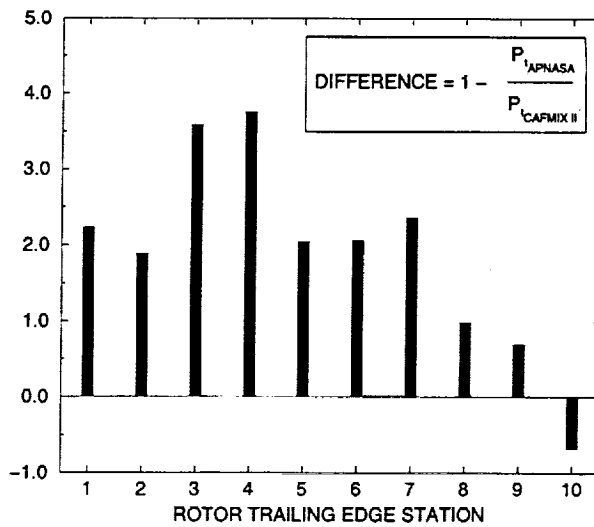
Fig. 14b. Comparison of total pressure as predicted by AP-NASA and CAFMIX II for the 10-stage GE90 compressor.
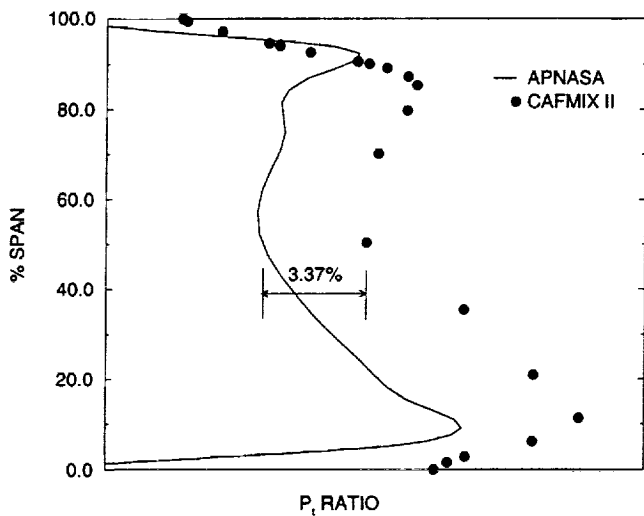

Fig. 15a. Spanwise distribution of total pressure at the exit of the stage 3 stator in the GE90 compressor.
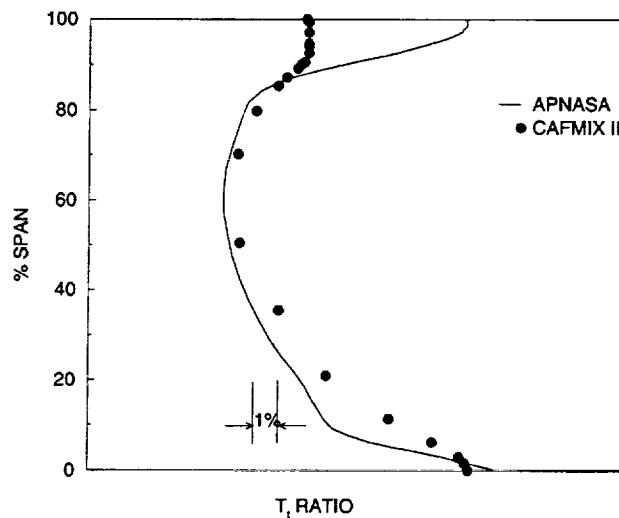
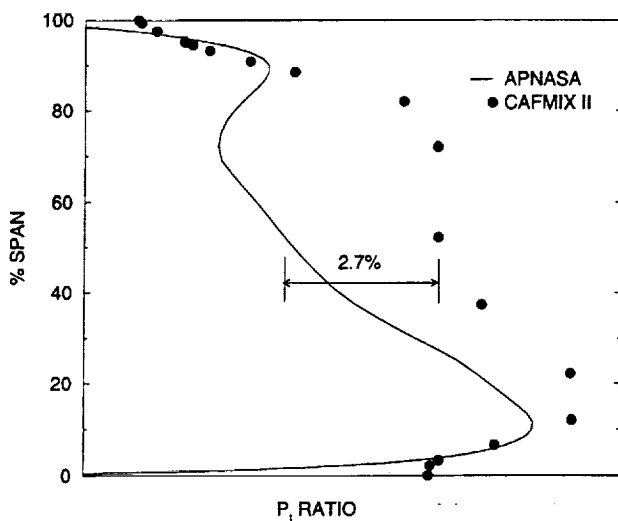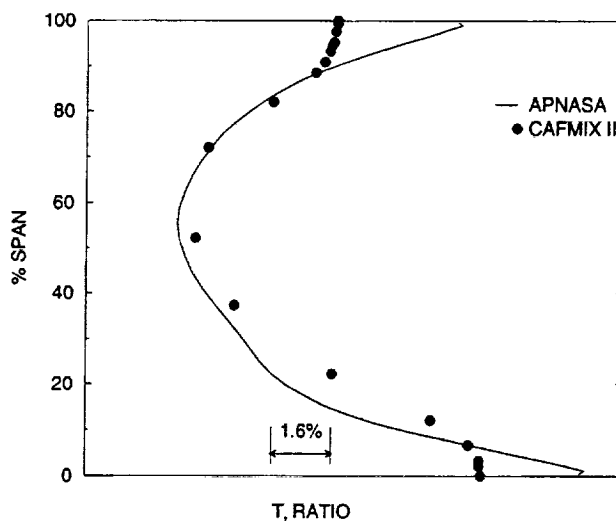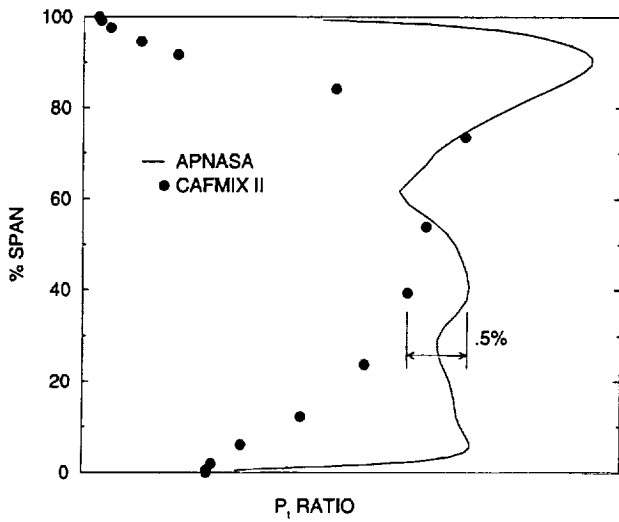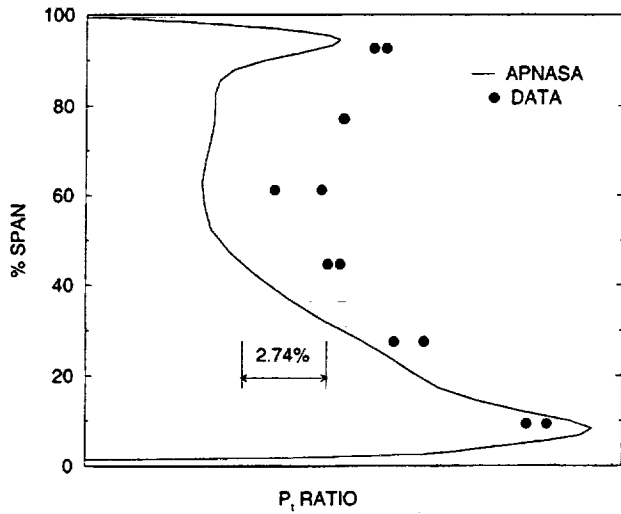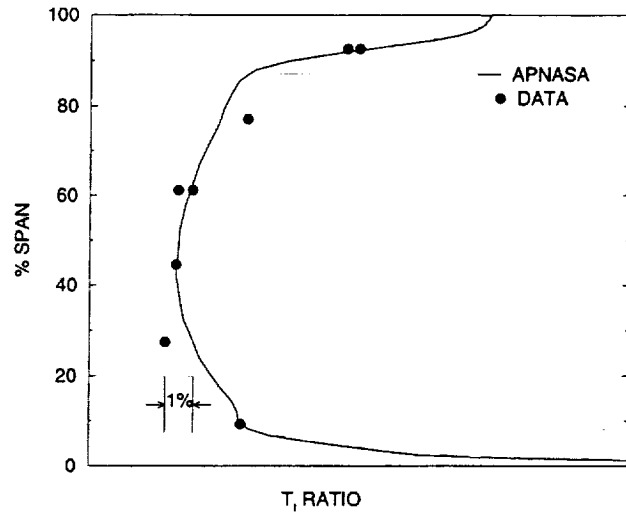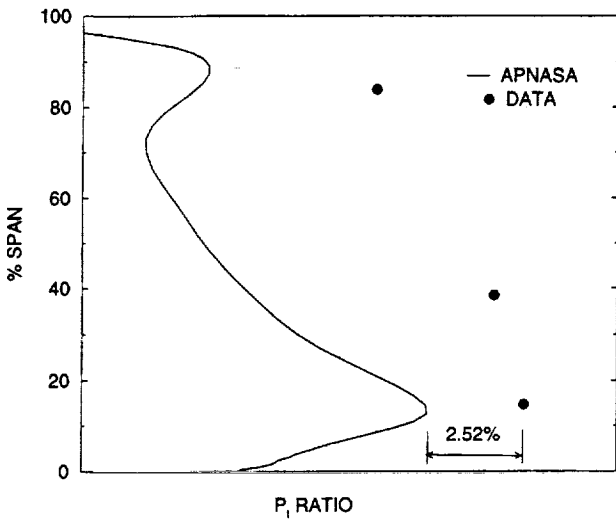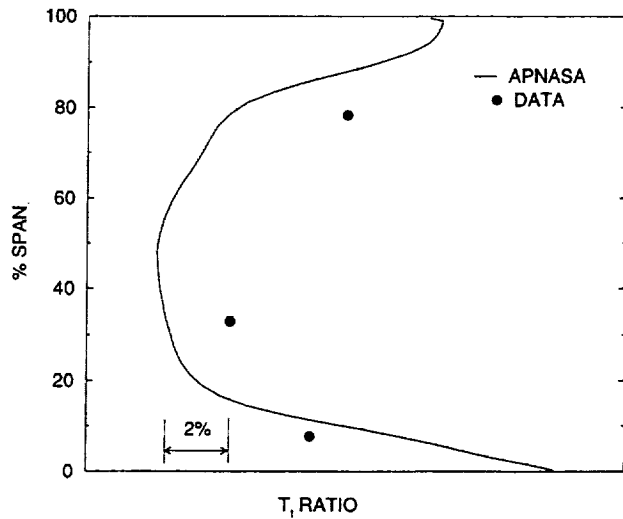Fig. 15b. Spanwise distribution of total temperature at the exit of the stage 3 stator in the GE90 compressor.

Fig. 15c. Spanwise distribution of total pressure at the exit of the stage 7 stator in the GE90 compressor.

Fig. 15d. Spanwise distribution of total temperature at the exit of the stage 7 stator in the GE90 compressor.

84

Fig. 15e. Spanwise distribution of total pressure at the compressor exit in the GE90 compressor.
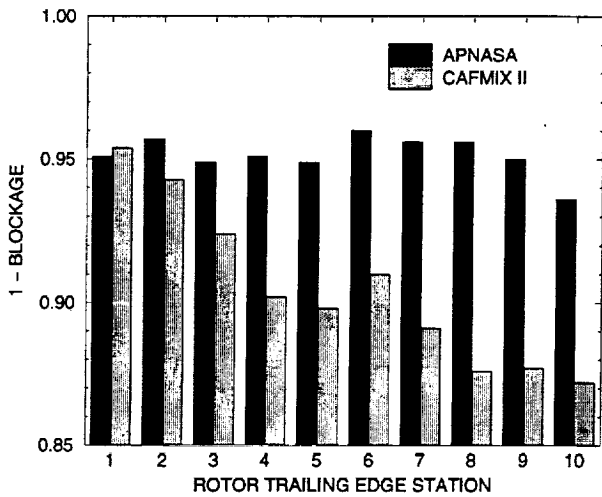
Fig. 16. Flow blockage distribution through the GE90 compressor.
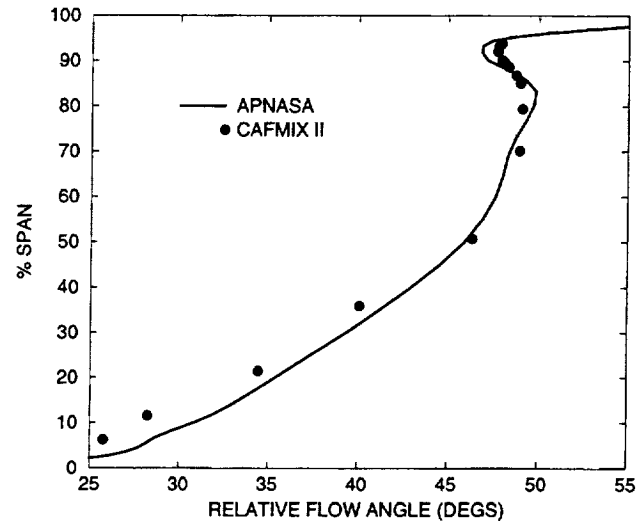
Fig. 17a. Relative flow angle at the exit of the stage 3 rotor in the GE90 compressor.
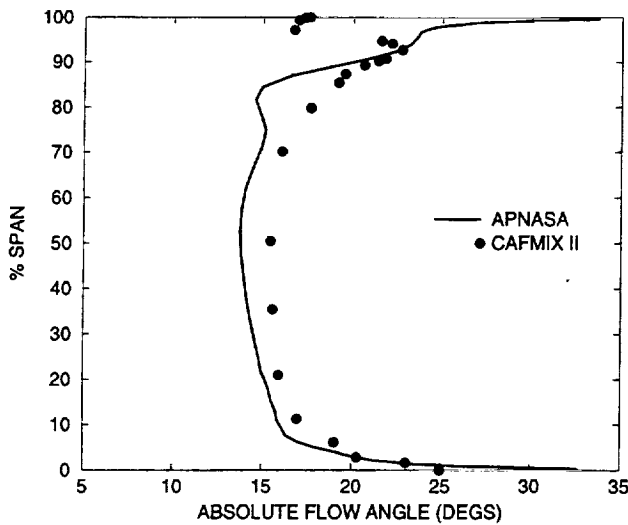
Fig. 17b. Absolute flow angle at the exit of the stage 3 stator in the GE90 compressor.
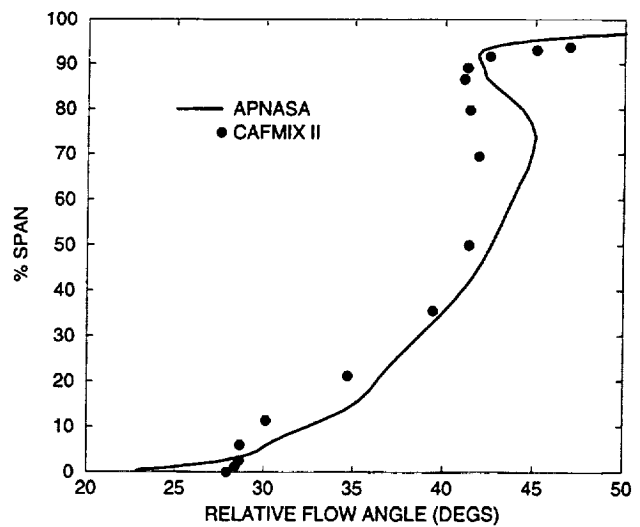
Fig. 17c. Relative flow angle at the exit of the stage 7 rotor in the GE90 compressor.
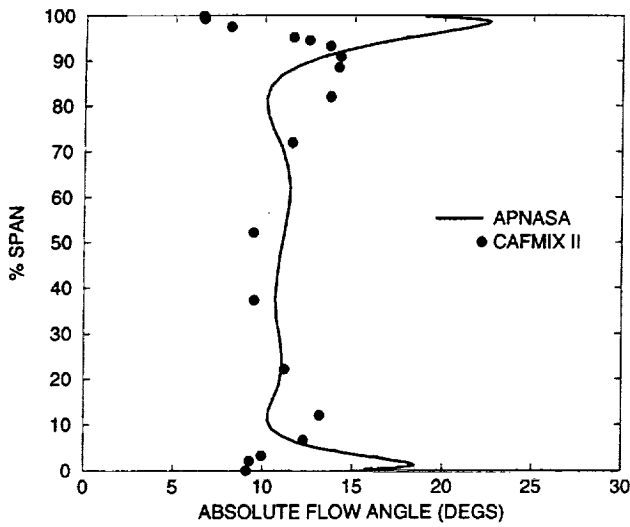
Fig. 17d. Absolute flow angle at the exit of the stage 7 stator in the GE90 compressor.
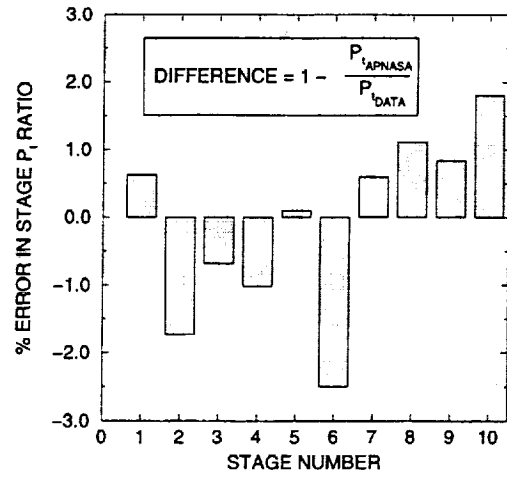
Fig. 18. Percent difference in total pressure through the GE90 compressor near the design speed operating point.

Fig. 19a. Spanwise distribution of total pressure at the exit of the stage 3 rotor in the GE90 near design speed.

Fig. 19b. Spanwise distribution of total temperature at the exit of the stage 3 rotor in the GE90 near design speed.

Fig. 19c. Spanwise distribution of total pressure at the exit of the stage 7 rotor in the GE90 near design speed.

Fig. 19d. Spanwise distribution of total pressure at the exit of the stage 7 rotor in the GE90 near design speed.

86
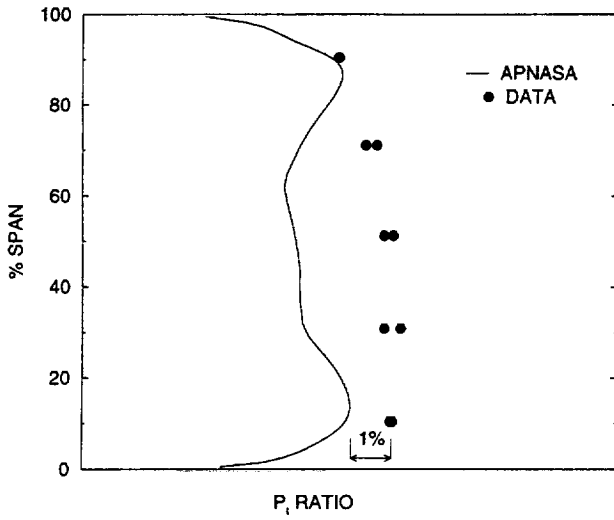
Fig. 19e. Spanwise distribution of total pressure at the exit of the GE90 near design speed.
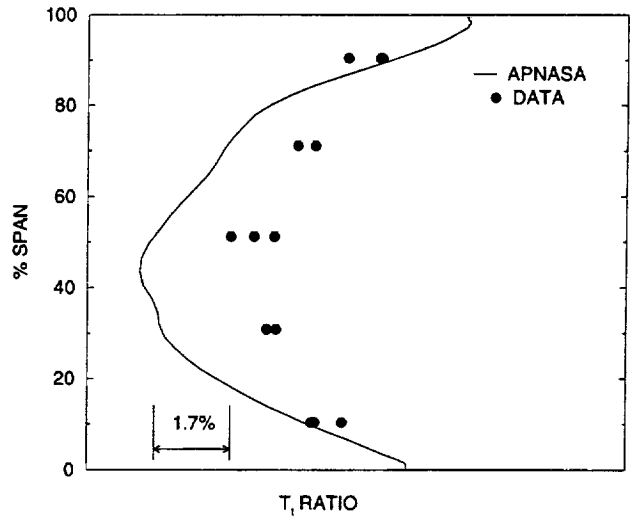
Fig. 19f. Spanwise distribution of total temperature at the exit of the GE90 near design speed.
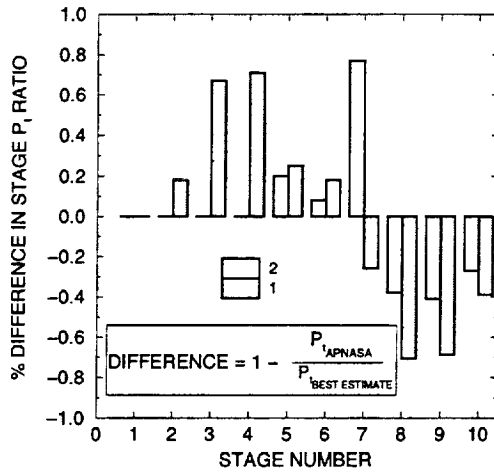
Fig. 20. Percent difference in stage pressure ratio as a function of bleed rates for the GE90 compressor.
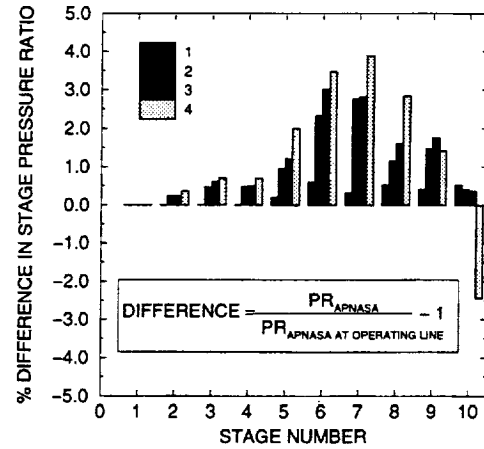
Fig. 21. Percent difference in stage pressure ratio as a function of back pressure for the GE90 compressor.
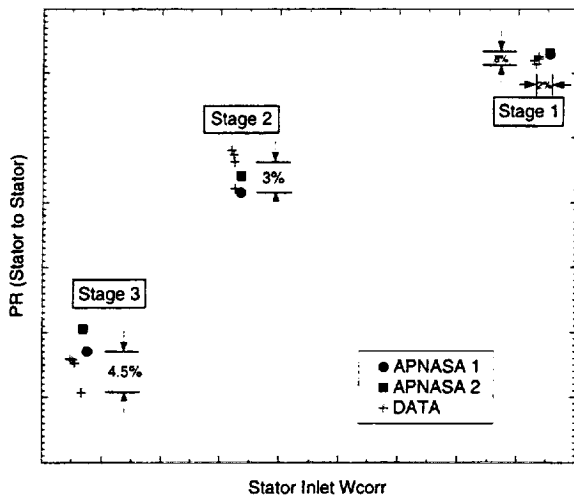
Fig. 22a. Stage total pressure ratio characteristic as a function of corrected mass flow for a 3-stage high speed compressor.
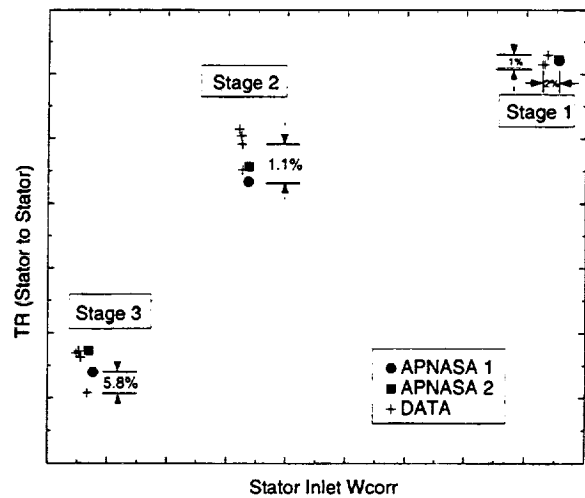
Fig. 22b. Stage total temperature ratio characteristic as a function of corrected mass flow for a 3-stage high speed compressor.
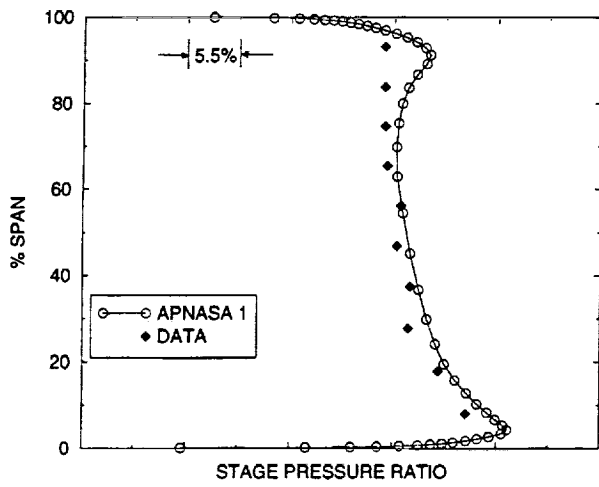
Fig. 23a. Spanwise distribution of total pressure at the exit of the stage 1 rotor for a 3-stage high speed compressor.
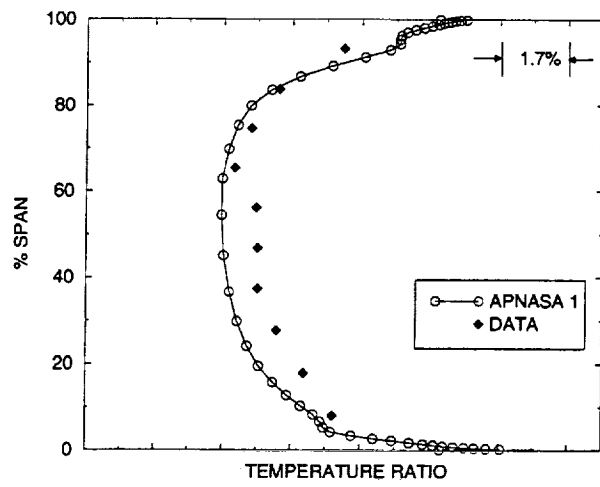
Fig. 23b. Spanwise distribution of total temperature at the exit of the stage 1 rotor for a 3-stage high speed compressor.
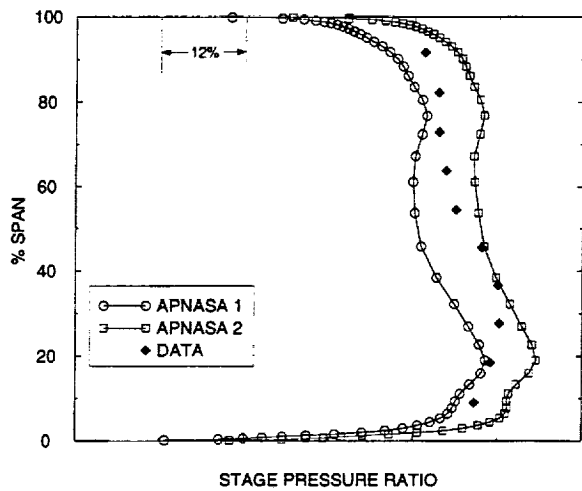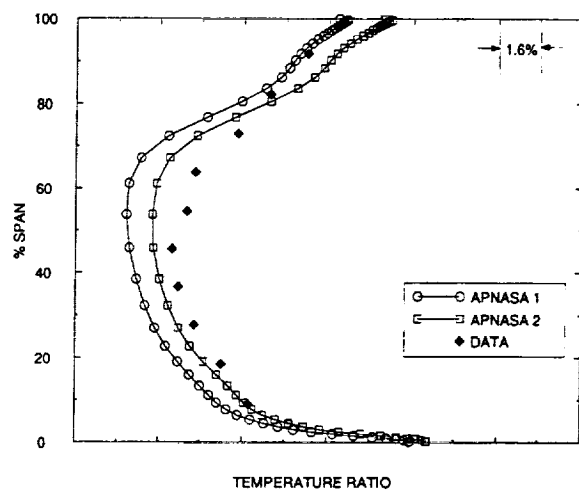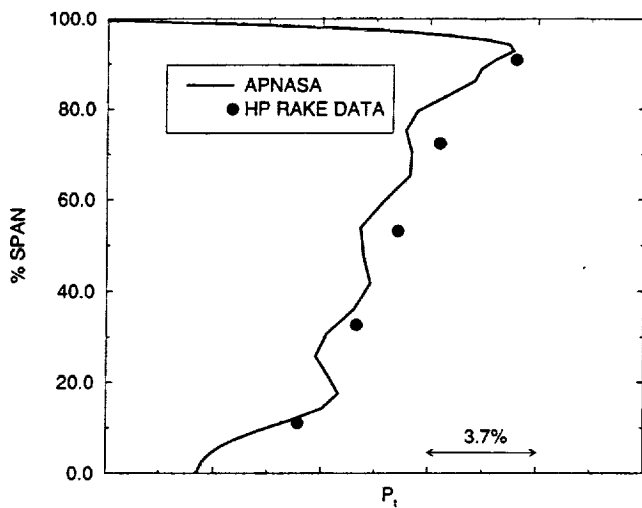

Fig. 24a. Spanwise distribution of total pressure at the exit of the stage 3 rotor for a 3-stage high speed compressor.

Fig. 24b. Spanwise distribution of total temperature at the exit of the stage 3 rotor for a 3-stage high speed compressor.

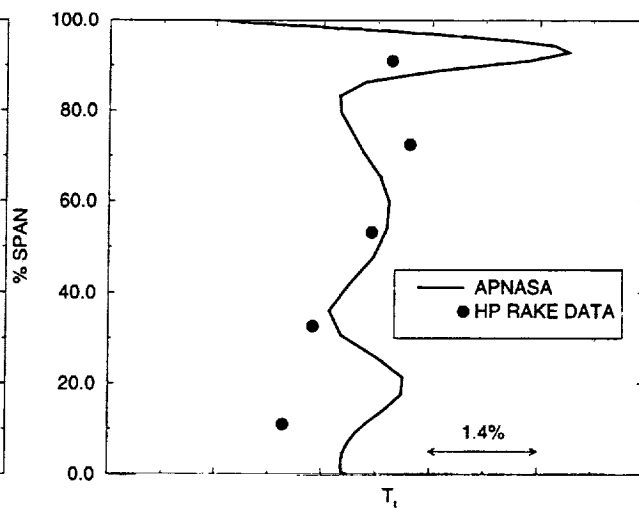Fig. 25a. Total pressure profile at the exit of an HP turbine stage 2 rotor.

Fig. 25b. Total temperature profile at the exit of an HP turbine stage 2 rotor.
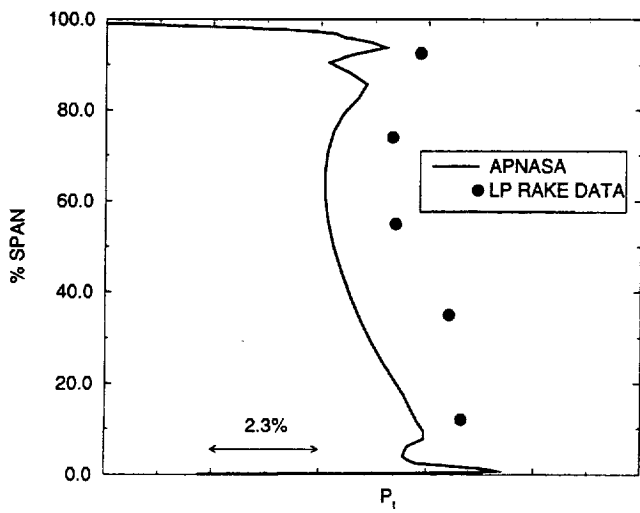
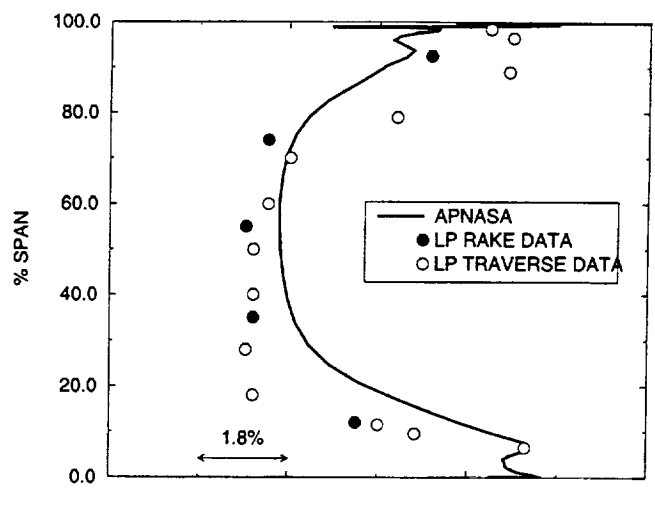Fig. 26a. Total pressure profile at the exit of an LP turbine.

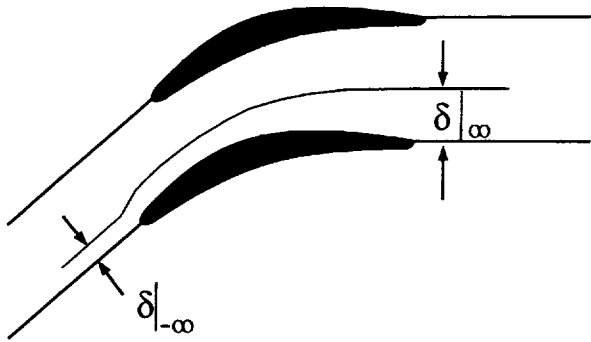Fig. 26b. Total temperature profile at the exit of an LP turbine.

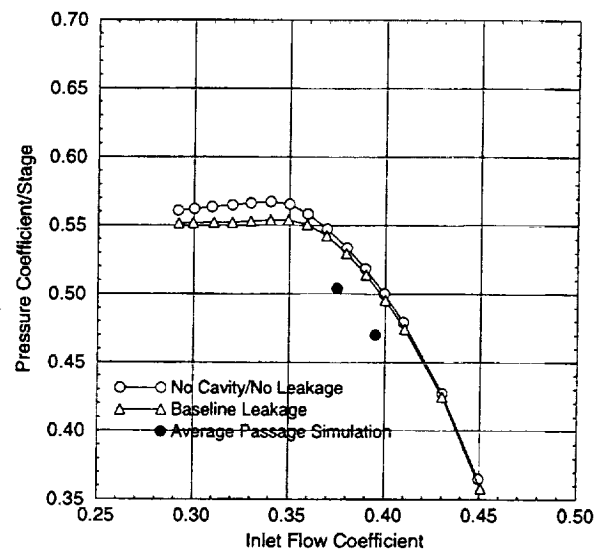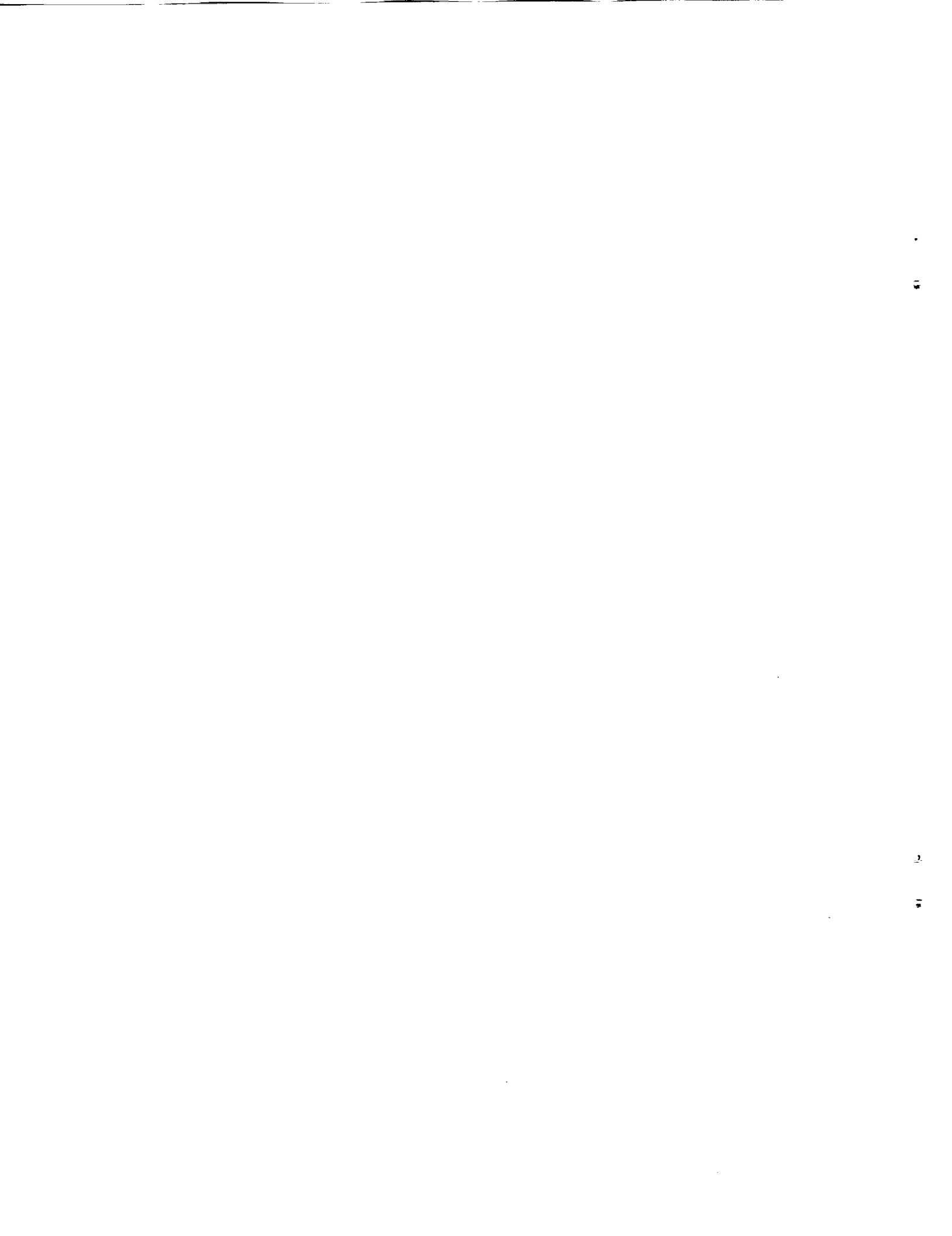Fig. 27. Steady flow through a cascade with blockage.

Fig. 28. Overall pressure coefficient as a function of inlet flow coefficient for the NASA-Lewis four stage axial flow compressor.

Appendix F

Combustor Analysis

Description for the efforts to model the combustor in APNASA with source terms. This approach was later replaced by a simple boundary condition treatment for representing combustor profiles.

GE90 Full Engine Simulation
COMBUSTOR ANALYSIS

An attempt was made to include the combustor in a reduced APC analysis of the GE90. The reduced APC analysis included the outlet guide vane (OGV) of the high pressure compressor, diffuser and combustor section, and first stage nozzle of the high pressure turbine (HPT). The flowpath included the diffuser and the hot section of the combustor, as illustrated by the heavy line in Fig. 1. The APC analysis was for two blade rows, the OGV and HPT nozzle, but the axisymmetric grid included the diffuser and combustor flowpaths, as shown in Fig. 2. Typical blade-to-blade grids for the OGV and HPT nozzle are shown in Figs. 3 and 4, respectively. The effect of the combustor was modeled with average passage body forces.

The body forces for the combustor section were obtained from a separate computation of the combustor flowfield using the program CONCERT3D, one of GE's combustion CFD codes. The three-dimensional solution from CONCERT3D was circumferentially averaged and interpolated onto the APC axisymmetric grid, as shown in Fig. 5. This axisymmetric solution was used to compute APC body forces by running the solution through the APC axisymmetric residual computation. With the body forces computed in this manner, it was thought that this axisymmetric solution would be recovered in the APC solution procedure. Part of the problem also stems from the fact that the governing equations, discretization schemes, and solution procedures for CONCERT3D and APC are very different, which makes it difficult to obtain consistent body forces to couple the solutions.

APC was subsequently used to compute the solution of the two blade row system with the combustor body forces obtained as described above. Several shortcomings in this approach were identified. Since the capability does not currently exist to model the diffuser, the rate and distribution of the flow aft of the OGV was inaccurate. Consequently, the desired effect of the body forces was not achieved. To obtain the proper effect with the body forces, the mass flow rate distribution must be approximately the same as the original distribution from the CONCERT3D analysis. Without modeling all the geometric details of the combustor, this would be very difficult to achieve.

It is believed that the shortcomings in the above approach could be overcome with much additional effort. The approach has the advantage of the combustor contribution coming from a detailed computation with a combustion CFD code. A much simpler, yet less desirable, methodology for coupling the compressor and turbine is currently being developed until the problems with the first approach can be overcome. The simpler method involves coupling the compressor and turbine by iteratively adjusting the OGV exit boundary conditions and HPT nozzle inlet boundary conditions based on the most recent solutions of each.
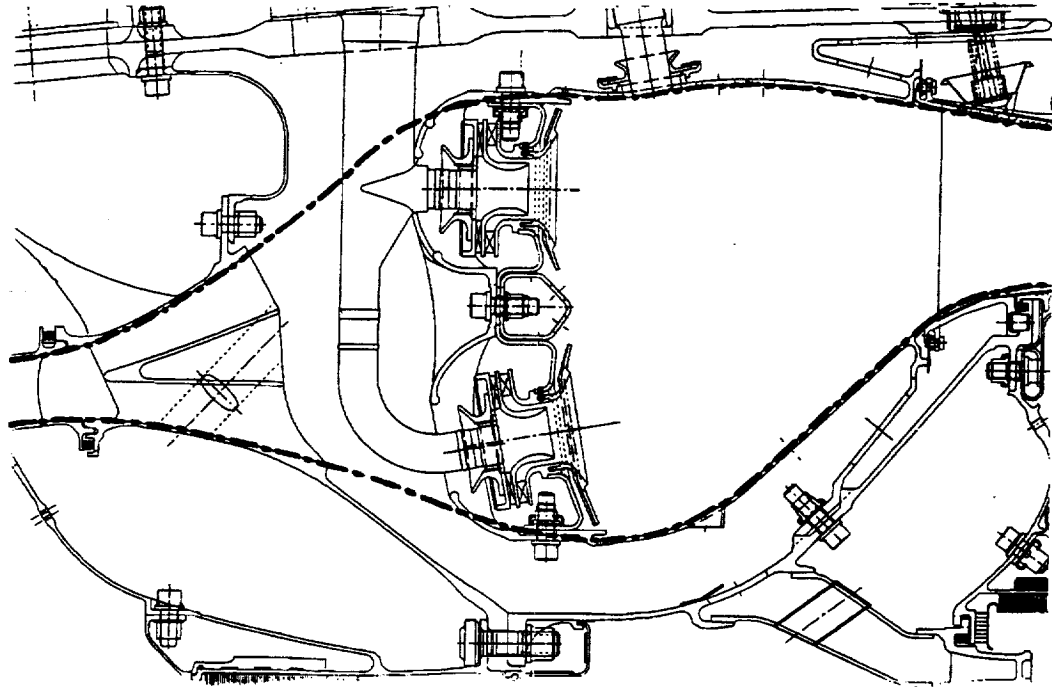
Fig. 1 Geometry for regio of interest, with modeled flowpath shown by heavy black lines.
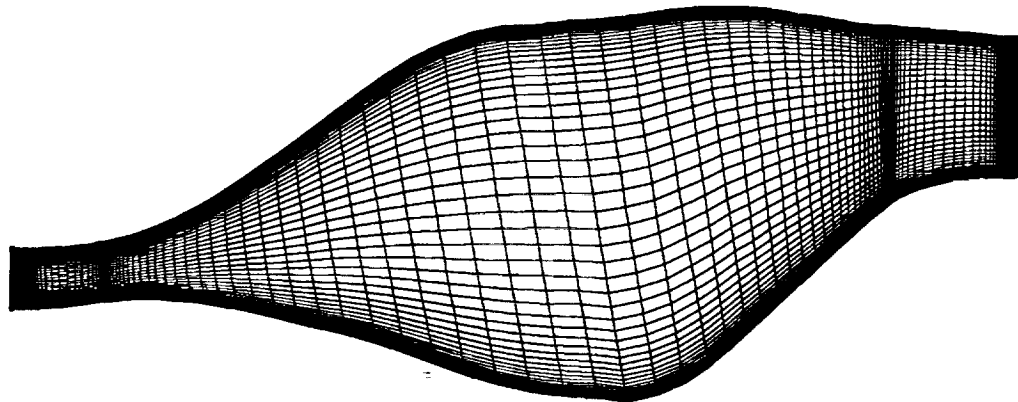

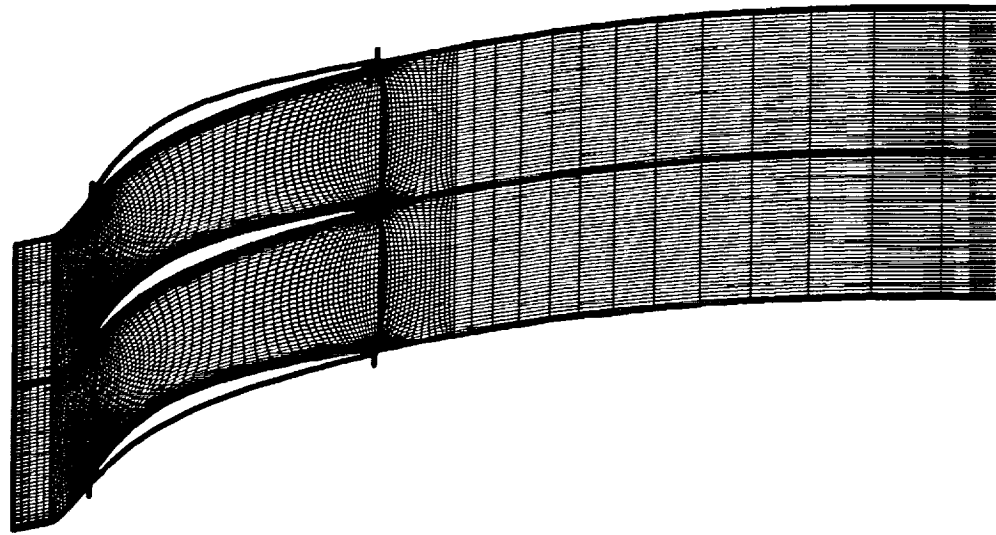Fig. 2 Axisymmetric grid for modeled region.

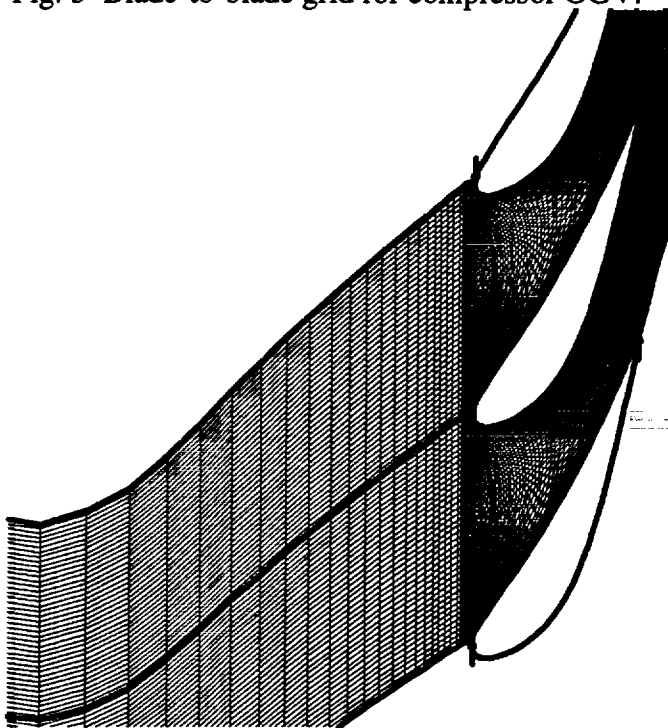Fig. 3 Blade-to-blade grid for compressor OGV.
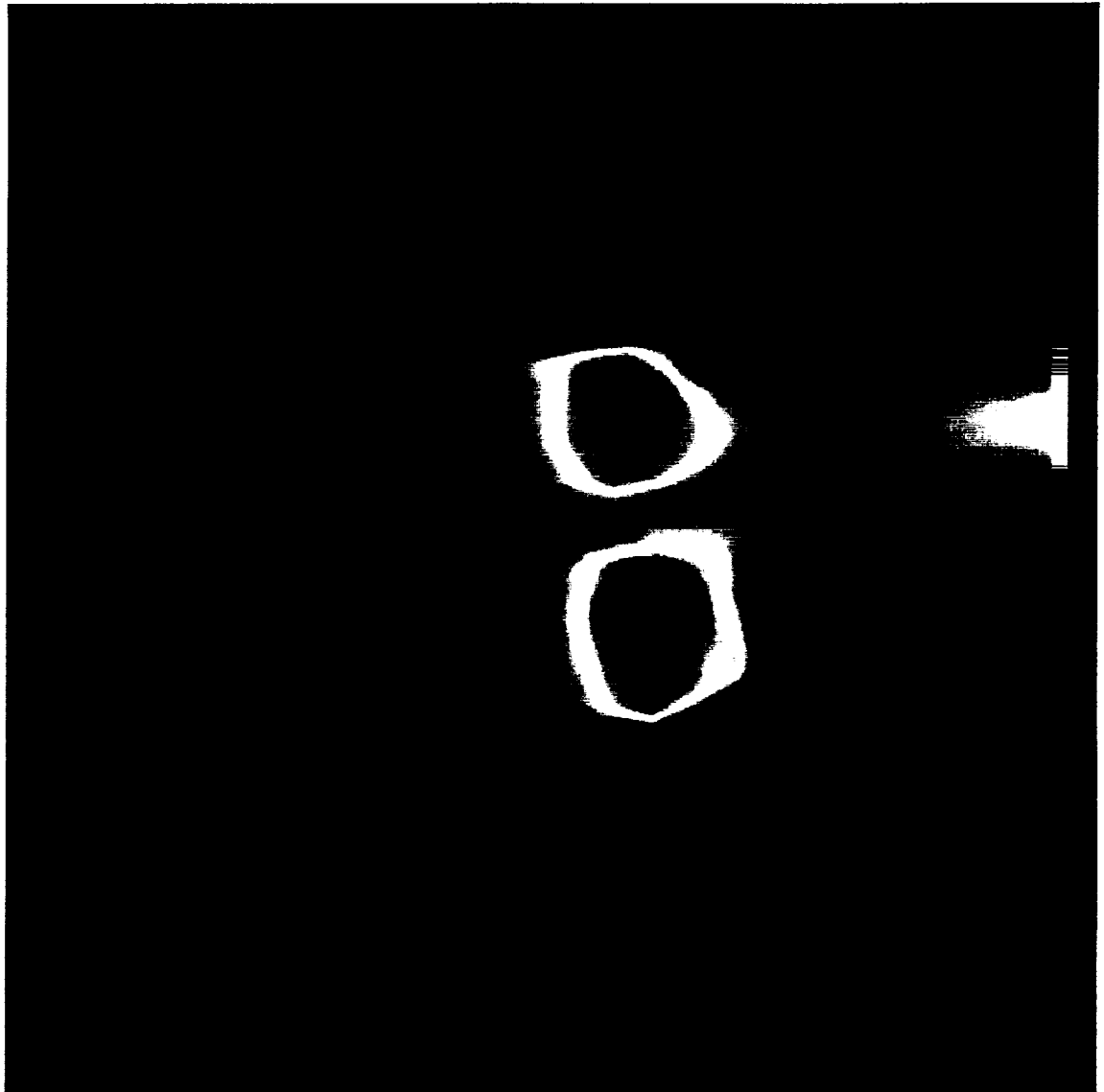

Fig. 4 Blade-to-blade grid for HPT nozzle.

Fig. 5 Circumferentially averaged initial solution from CONCERT3D.

REPORT DOCUMENTATION PAGE

Public reporting burden for this collection of information is estimated to average 1 hour per response, including the time for reviewing instructions, searching existing data sources, gathering and maintaining the data needed, and completing and reviewing the collection of information. Send comments regarding this burden estimate or any other aspect of this collection of information, including suggestions for reducing this burden, to Washington Headquarters Services, Directorate for Information Operations and Reports, 1215 Jefferson Davis Highway, Suite 1204, Arlington, VA 22202-4302, and to the Office of Management and Budget, Paperwork Reduction Project (0704-0188), Washington, DC 20503.

1. AGENCY USE ONLY (Leave blank)	2. REPORT DATE	3. REPORT TYPE AND DATES COVERED
	March 2000	Final Contractor Report

4. TITLE AND SUBTITLE

Full 3D Analysis of the GE90 Turbofan Primary Flowpath

5. FUNDING NUMBERS

WU–509–10–11–00
NAS3–26617
Task Order 65

6. AUTHOR(S)

Mark G. Turner

7. PERFORMING ORGANIZATION NAME(S) AND ADDRESS(ES)

GE Aircraft Engines
One Neumann Way
Cincinnati, Ohio 45215-6301

8. PERFORMING ORGANIZATION REPORT NUMBER

E–12205

9. SPONSORING/MONITORING AGENCY NAME(S) AND ADDRESS(ES)

National Aeronautics and Space Administration
John H. Glenn Research Center at Lewis Field
Cleveland, Ohio 44135–3191

10. SPONSORING/MONITORING AGENCY REPORT NUMBER

NASA CR—2000-209951

11. SUPPLEMENTARY NOTES

12a. DISTRIBUTION/AVAILABILITY STATEMENT

Unclassified - Unlimited
Subject Categories: 07, 02, and 34   Distribution: Nonstandard

This publication is available from the NASA Center for AeroSpace Information, (301) 621–0390.

12b. DISTRIBUTION CODE

13. ABSTRACT (Maximum 200 words)

The multistage simulations of the GE90 turbofan primary flowpath components have been performed. The multistage CFD code, APNASA, has been used to analyze the fan, fan OGV and booster, the 10-stage high-pressure compressor and the entire turbine system of the GE90 turbofan engine. The code has two levels of parallel, and for the 18 blade row full turbine simulation has 87.3 percent parallel efficiency with 121 processors on an SGI ORIGIN. Grid generation is accomplished with the multistage Average Passage Grid Generator, APG. Results for each component are shown which compare favorably with test data.

14. SUBJECT TERMS

Turbofan; CFD; Modeling; Flow; Numerical; Compressor; Turbine

15. NUMBER OF PAGES

101

16. PRICE CODE

A06

17. SECURITY CLASSIFICATION OF REPORT	18. SECURITY CLASSIFICATION OF THIS PAGE	19. SECURITY CLASSIFICATION OF ABSTRACT	20. LIMITATION OF ABSTRACT
Unclassified	Unclassified	Unclassified	

NSN 7540-01-280-5500

Standard Form 298 (Rev. 2-89)
Prescribed by ANSI Std. Z39-18
298-102